A SUBSPACE APPROACH TO HIGH-RESOLUTION MAGNETIC RESONANCE SPECTROSCOPIC IMAGING

BY

FAN LAM

DISSERTATION

Submitted in partial fulfillment of the requirements
for the degree of Doctor of Philosophy in Electrical and Computer Engineering
in the Graduate College of the
University of Illinois at Urbana-Champaign, 2015

Urbana, Illinois

Doctoral Committee:

Professor Zhi-Pei Liang, Chair
Professor Stephen Boppart
Professor Minh Do
Associate Professor Brad P. Sutton

ABSTRACT

With its unique capability to obtain spatially resolved biochemical profiles from the human body noninvasively, magnetic resonance spectroscopic imaging (MRSI) has been recognized as a powerful tool for in vivo metabolic studies. However, research and clinical applications of in vivo MRSI have been progressing more slowly than expected. The main reasons for this situation are the problems of long data acquisition time, poor spatial resolution and low signal-to-noise ratio (SNR) for this imaging modality.

In the last four decades, significant efforts have been made to improve MRSI, resulting in a large number of fast pulse sequences and advanced image reconstruction methods. However, the existing techniques have yet to offer the levels of improvement in imaging time, spatial resolution and SNR necessary to significantly impact in vivo applications of MRSI. This thesis work develops a new subspace imaging approach to address these technical challenges to enable fast, high-resolution MRSI with high SNR.

The proposed approach, coined SPICE (Spectroscopic Imaging by Exploiting Spatiospectral Correlation), is characterized by using a subspace model for integrative data acquisition, processing and image reconstruction. More specifically, SPICE represents the spectroscopic signals in MRSI using the partial separability (PS) model. The PS model implies that the high-dimensional spectroscopic signals reside in a low-dimensional subspace, which enables the design of special sparse sampling strategies for accelerated spatiospectral encoding and special image reconstruction strategies for determining the subspace and reconstructing the underlying spatiospectral function of interest from the sparse data. Using the SPICE framework, new data acquisition and image reconstruction methods are developed to enable high-resolution ^{1}H-MRSI of the brain.

We have evaluated SPICE using theoretical analysis, numerical simulations, phantom

and in vivo experimental studies. Results obtained from these experiments demonstrate the unprecedented capability of SPICE in achieving accelerated MRSI with simultaneously very high resolution and SNR. We expect SPICE to provide a powerful tool for in vivo metabolic studies with many exciting applications. Furthermore, the SPICE framework also presents new opportunities for future developments in subspace-driven signal generation, signal encoding, data processing and image reconstruction methods to advance the research and clinical applications of high-resolution in vivo MRSI.

To my parents and my wife

ACKNOWLEDGMENTS

Graduate school has been a long but fruitful journey for me. During this journey, I have felt extremely fortunate for the opportunity and privilege to work and interact with the most brilliant minds at the University of Illinois. Although I cannot list all the names of those who have helped, motivated and inspired me during the past seven years here, I would like to express my sincere appreciation to every one of them.

I would like to express my deepest gratitude to my advisor, Professor Zhi-Pei Liang, for his constant and selfless support and guidance in my research, career development and personal growth, and for willingly sharing his passion for scientific pursuit, his ideas and his visions with me. The invaluable experience of working with him and following his advice has shaped me into the researcher I am today. I am grateful to my doctoral committee members, Professors Brad Sutton, Stephen Boppart and Minh Do, for their time, help and insightful comments on my thesis research.

I thank my labmates for building a vibrant and inspiring research environment in the group. I am thankful to Dr. Justin Haldar, whose creativity, knowledge and critical thinking helped me tremendously during the early stage of my graduate studies; to Drs. Chao Ma and Bo Zhao for the fruitful collaborations and stimulating discussions, and for their support during the rough times of graduate school; and to Mohammed Sheikh for proofreading parts of my dissertation. Special thanks to Anthony Christodoulou, Bryan Clifford, Qiang Ning, Maojing Fu, Jingfei He, Yu Han, Guangpu Shao, Qiegen Liu, and Miguel Moscoso and former group members Drs. Diego Hernando, Hien Nguyen, Derin Babacan, Xiaobo Qu, Xi Peng, Huiqian Du, Zhenghua Wu, Yan Liu, Ling Wang, and Xin Wang and Ding Liu. I would also like to express my gratitude to Dr. Curtis Johnson, for helping us to gain easier access to the scanners, without which we would not have been able to produce the human

in vivo experimental results. Appreciation also goes to Tracey Wszalek, Rochelle Yambert, Ryan Larson, Nancy Dodge and Holly Tracy at the Biomedical Imaging Center.

I am grateful to Drs. Norbert Schuff, Michael Weiner, and Zhuang Song at the University of California at San Francisco, for hosting my visits to the Center for Imaging of Neurodegenerative Diseases, and for the productive collaboration and their support of my diffusion imaging project; to Drs. Chien Ho and Kevin Hitchens and other people at the Pittsburgh NMR Center for Biomedical Research, including Lesley Foley, Li Liu, Yijen Wu and Michelle Waters, for hosting me and helping me conduct the animal experiments during the early efforts on demonstrating the potential of SPICE for in vivo MRSI studies.

I would like to acknowledge the financial support from the Computational Science and Engineering program, the Beckman Institute, and the University of Illinois during my graduate studies.

Thank Chong, Minhao, Hanchao, Yang and Huiguang for their friendship and inspiration.

Finally, I am indebted to my parents, for their unconditional love and support. I am particularly grateful to my wife, Huimin, for her love, companionship, support and constant inspiration. They make me who I am.

TABLE OF CONTENTS

LIST OF ABBREVIATIONS

1D	One-dimensional
2D	Two-dimensional
3D	Three-dimensional
BW	Bandwidth
CG	Conjugate gradient
Cho	Choline
CP	Conjugate phase
Cr	Creatine
CRB	Cramér-Rao bound
CS	Compressed sensing
CSF	Cerebrospinal fluid
CSI	Chemical-shift imaging
EPI	Echo-planar imaging
EPSI	Echo-planar spectroscopic imaging
FE	Frequency encoding
FID	Free induction decay
FIM	Fisher information matrix
FOV	Field of view
Gln	Glutamine
Glu	Glutamate

GRE	Gradient echo
i.i.d.	Independent and identically distributed
mI	Myo-inositol
MPRAGE	Magnetization-prepared rapid gradient-echo
MRI	Magnetic resonance imaging
MRS	Magnetic resonance spectroscopy
MRSI	Magnetic resonance spectroscopic imaging
NAA	N-acetylaspartate
NRMSE	Normalized root mean squared error
OVS	Outer volume suppression
PE	Phase encoding
ppm	Parts per million
PRESS	Point Resolved Spectroscopy
PS	Partial separability
PSF	Partially separable function
RF	Radio-frequency
RMSE	Root mean squared error
SE	Spin echo
SPICE	Spectroscopic imaging by exploiting spatiospectral correlation
SVD	Singular value decomposition
TE	Echo time
TR	Repetition time
VOX	Volume of excitation
ms	Millisecond
μs	Microsecond

CHAPTER 1

INTRODUCTION

1.1 Motivation

The potential of using MR signals to resolve spatially dependent metabolic profiles was realized soon after the inception of MRI [1–3]. The resulting imaging modality, coined MR spectroscopic imaging (MRSI), provides us a unique noninvasive window into the biochemical profiles of the human body [4,5] and therefore has been recognized as a promising tool for in vivo metabolic studies. Various research and clinical applications of in vivo MRSI have been identified, including detection, characterization and treatment monitoring of cancers [5–7], neurological and psychiatric disorders, and various other metabolic diseases [8–13]. However, the development of in vivo MRSI has been slower than expected. This is mainly due to the following fundamental technical hurdles:

- **Low signal-to-noise-ratio (SNR)**: The molecules (also referred to as metabolites in this thesis) being imaged in MRSI typically have more than a thousand times lower concentration than the water molecules that are imaged in conventional magnetic resonance imaging (MRI) experiments [14]. Therefore, MRSI is an imaging modality with extremely low sensitivity.

- **Long data acquisition time**: Due to the low SNR challenge, multiple signal averages are often acquired to improve the SNR in MRSI experiments. Furthermore, conventional MRSI methods mostly rely on very slow spatial encoding schemes [2,15]. These approaches significantly prolong the data acquisition time and limit the practical utility of MRSI in research and clinical applications, especially for in vivo studies.

- **Poor spatial resolution**: To shorten the data acquisition time, the existing MRSI

methods typically constrain themselves to a limited number of spatial encodings, and obtain reconstructions with large voxel sizes (on the order of 1 cm^3) to ensure sufficient SNR. This results in poor spatial resolution with severe voxel interference, which counteracts the unique advantage of MRSI in obtaining spatially-resolved spectroscopic information.

- **Overwhelming nuisance signals**: In some MRSI experiments, strong nuisance components can conceal the underlying signals of interest. One typical example is the overwhelming nuisance water and lipid signals in ^{1}H-MRSI. These nuisance signals, if not effectively removed, can have detrimental effects on estimation of the desired metabolite spatiospectral distributions.

Over the past four decades, significant efforts have been made to address these challenges for improved MRSI. Besides the advancement in hardware such as scanners with higher field strengths and better stability [5, 12, 16] and parallel transmission/receiver arrays [17–22], which is expected to be an integral part of any advanced imaging method, a large number of fast sequences and advanced reconstruction methods have been proposed. For fast data acquisition, one key approach is to incorporate echo-planar type of data acquisition schemes with spectroscopic imaging. Many methods (and pulse sequences) have been proposed to implement this data acquisition strategy (see [15, 23–33] for a more detailed discussion of some of the fast-scanning methods). While these methods can significantly reduce the data acquisition time for high-resolution spatiospectral encoding, it is at the expense of SNR, which is already a significant limitation for in vivo MRSI experiments. Advanced image reconstruction methods have been focusing on using prior information to compensate for the lack of sufficient measurements or SNR. To this end, a number of image models have been proposed to incorporate anatomical prior [34–39], sparsity and rank constraints [40–45], and explicit parametric model constraints [41, 46] to improve MRSI reconstruction from noisy or undersampled data. However, reconstruction methods alone have not been able to provide the level of improvement in spatial resolution, data acquisition speed, and SNR necessary to have a major impact on in vivo MRSI.

This thesis research aims at developing a new subspace imaging approach to both data acquisition and image reconstruction to enable accelerated high-resolution MRSI with high SNR.

1.2 Main Results

In this thesis,

- We propose a new subspace imaging approach to accelerate spectroscopic imaging. The proposed approach, called SPICE (Spectroscopic Imaging by Exploiting Spatiospectral Correlation), exploits the unique property known as partial separability (PS) of spectroscopic signals [47–50]. This property indicates that high-dimensional spectroscopic signals reside in a very low-dimensional subspace and enables the design of special data acquisition and image reconstruction strategies to achieve high-resolution MRSI with good SNR. More specifically, for data acquisition, SPICE proposes to sparsely sample the (k, t)-space in two complementary data sets, one with dense temporal sampling (capturing full spectral information) and high SNR but limited k-space coverage (denoted as $\mathcal{D}_1$), and the other with extended k-space coverage (for the desired spatial resolution) but sparse temporal sampling (denoted as $\mathcal{D}_2$). With these data, SPICE proposes a two-step reconstruction strategy that estimates the subspace from $\mathcal{D}_1$ and the high-resolution spatiotemporal/spatiospectral function of interest from $\mathcal{D}_2$. Theoretical analysis and numerical simulations are performed to evaluate the performance of the SPICE framework.

- We propose special pulse sequences to implement the hybrid sparse sampling strategy in the SPICE framework for high-resolution ^{1}H-MRSI of the brain. Specifically, a hybrid chemical shift imaging (CSI)/echo-planar spectroscopic imaging (EPSI) sequence is developed for rapid two-dimensional (2D) spatial plus spectral encoding. The CSI component has limited k-space coverage but high SNR, and uses the entire free induction decay (FID) period for spectral encoding, and thus an ideal option to generate $\mathcal{D}_1$ for accurate subspace estimation. The EPSI component has high speed and allows for

an extended k-space coverage within a short period, thus providing the $\mathcal{D}_2$ needed for high-resolution spatiospectral reconstruction. For high-resolution three-dimensional (3D) MRSI using SPICE, however, this sequence is too slow to provide the number of spatial encodings needed in a short time frame. To address this issue, we propose a dual-density, dual-speed sequence that performs a hybrid of slow EPSI scans (to acquire $\mathcal{D}_1$) and rapid EPSI-like scans (to acquire $\mathcal{D}_2$). These proposed hybrid sampling schemes effectively combine the advantages of slow scans (i.e., high SNR and full spectral encoding) and rapid scans (i.e., high resolution and speed) for accelerated MRSI using sparse sampling.

- Given the data generated by the proposed sequences, the main issues for SPICE reconstruction are estimation of the subspace structure (or the set of basis spanning the low-dimensional subspace) from $\mathcal{D}_1$ and reconstruction of the unknown spatiotemporal/spatiospectral function from $\mathcal{D}_2$. The key problem to subspace estimation is the removal of B_0 field inhomogeneity effects from the limited k-space data. Assuming the availability of a high-resolution field map, we utilize a regularized super-resolution reconstruction scheme to solve this problem. With the subspace determined from the field corrected data, the reconstruction problem can be translated into the estimation of a set of spatial coefficients, which has a significantly reduced number of degrees-of-freedom compared to the high-dimensional spatiospectral function of interest (rendering high SNR reconstruction from the very noisy and sparse data possible). This problem can then be solved using a regularized linear least-squares formulation that incorporates an explicit low-rank model with the capability of field inhomogeneity correction and regularization. The use of regularization not only serves to stabilize the coefficient fitting problem but also incorporates additional prior information for improved reconstruction. Different choices of regularization functional are discussed, and efficient algorithms for solving the resulting optimization problems are presented.

- We have systematically evaluated the performance of the proposed methods through metabolite phantom and in vivo ^{1}H-MRSI studies conducted on a 3T scanner. Results from these experiments demonstrate the unprecedented capability of SPICE in

achieving fast, high-resolution ^{1}H-MRSI with very high SNR. In particular, for 2D in vivo experiments, SPICE is able to produce high-SNR ^{1}H metabolite maps from the human brain with an approximately 2 mm in-plane resolution in 15 minutes. For 3D in vivo experiments, SPICE is able to produce metabolite maps with an approximately 3 mm in-plane and 4 mm through-plane resolution in about 26 minutes. To the best of our knowledge, these are the highest resolution ^{1}H metabolite maps ever obtained from the human brain on a 3T system [12, 51].

1.3 Organization of the Dissertation

This dissertation is organized as follows:

Chapter 2 reviews the concepts essential for understanding the materials in this thesis. Specifically, the mechanisms underlying MR imaging and spectroscopic imaging are briefly discussed. The mathematical preliminaries for the proposed subspace imaging approach are also covered. Chapter 3 introduces the SPICE subspace imaging framework for high-resolution MRSI. The subspace model, the overall data acquisition and image reconstruction strategies dictated by the subspace model are described. Theoretical analysis and numerical simulation results are shown to demonstrate the properties and potential of the SPICE framework. Chapter 4 describes the proposed data acquisition methods that implement the SPICE sparse sampling strategy to achieve rapid spatiospectral encoding for high-resolution ^{1}H-MRSI of the brain. Chapter 5 presents the proposed image reconstruction methods for subspace estimation and spatiospectral reconstruction from the sparse data generated by the proposed acquisition methods described in Chapter 4. Chapter 6 presents experimental results obtained from carefully designed brain metabolite phantoms and human brain to evaluate the performance of the proposed methods in practical ^{1}H-MRSI experiments. Chapter 7 concludes the thesis and highlights some exciting future research directions.

CHAPTER 2

BACKGROUND

2.1 Magnetic Resonance Imaging (MRI)

When placed in a strong static magnetic field $\vec{B_0} = B_0\vec{k}$ (assuming homogeneous field), a macroscopic sample can generate a bulk magnetization that precesses around the direction of the $\vec{B_0}$ field as

$$\vec{M} = \sum_{i=1}^{N_e} \vec{\mu}_i, \tag{2.1}$$

where $\vec{\mu}_i = \mu\vec{k}$ corresponds to the magnetic momentum for the ith nucleus with nonzero spin quantum number in the sample and N_e denotes the total number of such nuclei.[1] Based on the theory of quantum mechanics, spins in the applied magnetic field ($\vec{B_0}$) will split into two states, one with lower energy

$$\vec{\mu}_i \cdot \vec{B_0} = -\frac{1}{2}\gamma\hbar B_0$$

and the other with higher energy

$$\vec{\mu}_i \cdot \vec{B_0} = \frac{1}{2}\gamma\hbar B_0.$$[2]

γ is the gyromagnetic ratio and $\hbar$ the Planck constant. According to the Boltzmann distribution [52], the numbers of spins in the lower energy state (N_u) and the higher energy state

[1] $\vec{i}$,$\vec{j}$, and $\vec{k}$ denote unit directional vectors along x, y and z directions.

[2] Only spin-$\frac{1}{2}$ is considered in this thesis.

(N_d) have the following relationship:

$$N_u - N_d \approx N_e \frac{\gamma \hbar B_0}{2KT_s},$$

where K is the Boltzmann constant and T_s is the absolute temperature of the spin system. Therefore, the magnitude of the bulk magnetization can be calculated as [52]

$$M_z^0 = |\vec{M}| \approx \left| \frac{1}{2}(N_u - N_d)\gamma \hbar \vec{k} \right| = \frac{\gamma^2 \hbar^2 B_0 N_e}{4KT_s}, \tag{2.2}$$

which fundamentally determines the amount of signal that can be generated in an NMR experiment. For example, in a static magnetic field with a strength of 3 T, only about 10 spins contribute to the bulk magnetization in a group of 1 million spins. Therefore, MRI is inherently a low-sensitive imaging modality. Fortunately, there are abundant spins in the human body. In particular, within a 1 mm^3 voxel in the human brain, there are approximately 10^{20} protons in the water molecules (assuming a 50 mol/L concentration), giving rise to a population difference of 10^{15} spins at $B_0 = 3$ T which also increases w.r.t. the strength of the B_0 field.[3]

The state of the spin system in a polarized sample with the presence of $\vec{B}_0$ alone (with the bulk magnetization in Eq. (2.2)) is generally referred to as the equilibrium. At equilibrium, the magnetic moments from the ensemble of spins have randomly distributed phase, which amounts to a zero transverse component of $\vec{M}$. To generate signal from such a sample, an additional magnetic field needs to be applied to perturb the system from equilibrium and establish a nonzero transverse component of $\vec{M}$ (i.e., to establish a phase coherence among the ensemble of spins). This field, coined as $\vec{B}_1(t)$, is time-varying as opposed to the static $\vec{B}_0$ field and needs to oscillate at the same frequency as the polarized spins in order to establish phase coherence (also referred to as *resonance*). Mathematically, the behavior of $\vec{M}$ in the

[3]Modern human MRI scanners have field strengths ranging from 1.5 to 11.7 T.

presence of a time-varying magnetic field $\vec{B}$ can be described by the *Bloch equation* below

$$\frac{d\vec{M}}{dt} = \gamma\vec{M} \times \vec{B} - \frac{M_x\vec{i} + M_y\vec{j}}{T_2} - \frac{(M_z - M_z^0)\,\vec{k}}{T_1}, \tag{2.3}$$

where $\vec{B} = \vec{B}_0 + \vec{B}_1(t)$, $M_x\vec{i} + M_y\vec{j}$ represents the transverse component of $\vec{M}$, $M_z\vec{k}$ represents the longitudinal component of $\vec{M}$ with initial value M_z^0, and T_1 and T_2 are time constants that characterize the relaxation process of the spin system back to equilibrium after being disturbed by the $\vec{B}_1$ field. At the end of $\vec{B}_1(t)$ (also referred to as the RF pulse), a transverse magnetization is generated $\vec{M}_{xy}(\mathbf{r}, t) = M_x(\mathbf{r}, t)\vec{i} + M_y(\mathbf{r}, t)\vec{j}$, which can be detected by a receiver coil placed closed to the object.[4]

Based on derivations using the Faraday law of induction and the reciprocity principle [53], the voltage signal induced in the receiver coil can be mathematically expressed as

$$V(t) \;=\; -\frac{\partial}{\partial t}\int_{object} \vec{B}_r(\mathbf{r}) \cdot \vec{M}(\mathbf{r}, t)d\mathbf{r}, \tag{2.4}$$

where $\vec{B}_r(\mathbf{r})$ is the receiver sensitivity profile, which is defined as the magnetic field generated by passing an unit current through the coil [52, 53]. Modern MRI scanners normally use a quadrature detection, in which case the signal that is actually being sampled has the following mathematical expression:

$$\begin{aligned} s(t) \;&\propto\; \omega_0 \int_{object} \bar{B}_{r,xy}(\mathbf{r}) M_{xy}(\mathbf{r}, 0) e^{-t/T_2(\mathbf{r})} e^{-i\int_0^t \Delta\omega(\mathbf{r},\tau)d\tau} d\mathbf{r} \\ &=\; \omega_0 \int_{object} \bar{B}_{r,xy}(\mathbf{r}) M_{xy}(\mathbf{r}, 0) e^{-t/T_2(\mathbf{r})} e^{-i\gamma\int_0^t \Delta B(\mathbf{r},\tau)d\tau} d\mathbf{r}, \end{aligned} \tag{2.5}$$

where ω_0 ($\omega_0 = \gamma B_0$) is the center resonance frequency of the spins (without field inhomogeneity) and $\Delta B(\mathbf{r}, t)$ represents a time-dependent field inhomogeneity term ($\Delta\omega(\mathbf{r}, t) =$

[4] The characteristics and excitation effects of an RF pulse are normally simpler to describe in the rotating reference frame, a comprehensive description of which is given in Ref. [52] and thus not repeated here.

$\gamma\Delta B(\mathbf{r},t)$). The quantities $B_{r,xy}$ and M_{xy} are defined as

$$\begin{aligned} B_{r,xy}(\mathbf{r}) &= B_{r,x}(\mathbf{r}) + iB_{r,y}(\mathbf{r}) \\ M_{xy}(\mathbf{r},0) &= M_x(\mathbf{r},0) + iM_y(\mathbf{r},0), \end{aligned}$$

and $\bar{B}_{r,xy}$ denotes the complex conjugate of $B_{r,xy}$. For a detailed derivation of Eq. (2.5) from Eq. (2.4), please refer to Ref. [52].

The signal model in Eq. (2.5) is the governing equation for devising encoding and decoding schemes for most MRI experiments. The field inhomogeneity $\Delta B(\mathbf{r},t)$ can be mainly attributed to two sources: (i) the inherent heterogeneous field distribution due to scanner imperfection and (ii) applied gradient fields to induced local resonance frequency changes for spatial encodings. Specifically, when a linear gradient field is applied, $\vec{G}(t) = G_x(t)\vec{i} + G_y(t)\vec{j} + G_z(t)\vec{k}$, the induced change in the magnetic field $\vec{B}_0$ is

$$\Delta B(\mathbf{r},t) = \vec{G}(t)\cdot\mathbf{r}. \tag{2.6}$$

The signal equation in (2.5) can then be rewritten as (ignoring the scaling constants)

$$\begin{aligned} s(t) &= \int_{object} \bar{B}_{r,xy}(\mathbf{r}) M_{xy}(\mathbf{r},0) e^{-t/T_2(\mathbf{r})} e^{-i\gamma\int_0^t \vec{G}(\tau)\cdot\mathbf{r}d\tau} d\mathbf{r} \\ &= \int_{object} \bar{B}_{r,xy}(\mathbf{r}) M_{xy}(\mathbf{r},0) e^{-t/T_2(\mathbf{r})} e^{-i2\pi\mathbf{k}(t)\cdot\mathbf{r}} d\mathbf{r}, \end{aligned} \tag{2.7}$$

where

$$\mathbf{k} = \gamma\!\!\!^{-}\int_0^t \vec{G}(\tau)d\tau \tag{2.8}$$

and $\gamma\!\!\!^{-} = \dfrac{\gamma}{2\pi}$. With some further simplification, e.g., ignoring relaxation effects during the data sampling period, we arrive at the most commonly used Fourier encoding signal model

for MR image reconstruction

$$s(\mathbf{k}) \quad = \quad \int_{object} \rho(\mathbf{r}) e^{-i2\pi \mathbf{k}\cdot\mathbf{r}} d\mathbf{r}, \tag{2.9}$$

where $\rho(\mathbf{r}) = \bar{B}_{r,xy}(\mathbf{r}) M_{xy}(\mathbf{r}, t_0)$, with t_0 denoting an initial time point for the start of the acquisition, is the image function of interest and $s(\mathbf{k})$ represents the well-known k-space measurement. Therefore, $\rho(\mathbf{r})$ can be reconstructed from a set of discrete samples $\{s(\mathbf{k}_m)\}_{m=1}^{M}$ by performing inverse Fourier transform on the data. For a majority of current MRI applications, multiple receiver coils are used in the acquisition, and a receiver sensitivity independent image function of interest (i.e., $M_{xy}(\mathbf{r})$) can be generated using special coil combination methods.

2.2 Magnetic Resonance Spectroscopic Imaging (MRSI)

2.2.1 Chemical Shift and NMR Spectroscopy

While most MRI experiments are only concerned with one type of spin that is in the same chemical environment (e.g., the protons on the water molecules), the nuclei in a biological object are often attached to different chemical environments. For example, the nuclei in different molecules are surrounded by orbiting electrons, which produce different magnetic fields that "locally" perturb the field felt by the nuclei to various extents. This effect, illustrated in Fig. 2.1, is referred to as the electron shielding effect. More specifically, the nuclei in different chemical environments (thus subject to different electron shielding effects) resonate at different frequencies specified by

$$\omega \quad = \quad \gamma B_0 (1 - \sigma), \tag{2.10}$$

where B_0 is the strength of the main magnetic field and σ is the shielding constant (can be both positive and negative). This frequency dispersion gives rise to the chemical shift phenomenon that is fundamental to the subject of NMR spectroscopy. As an example,

different proton groups in the N-acetylaspartate (NAA) molecules have distinct resonance frequencies compared to the protons in the water molecules (as illustrated in Fig. 2.2), allowing us to measure and quantify the concentration and other properties of NAA through quantitative analysis of the NMR signals.

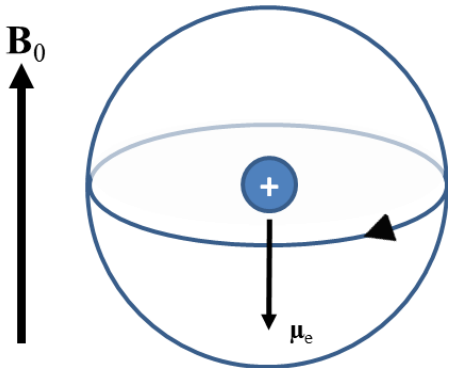

Figure 2.1: Illustration of the electron shielding effect that gives rise to chemical shift. As can be seen, the electron orbiting around the nuclei (denoted by the big black arrow) can be viewed as a small current, which generates a magnetic moment $\boldsymbol{\mu}_e$ that opposes the main magnetic field B_0, thus perturbs the magnetic field felt "locally" by the nuclei.

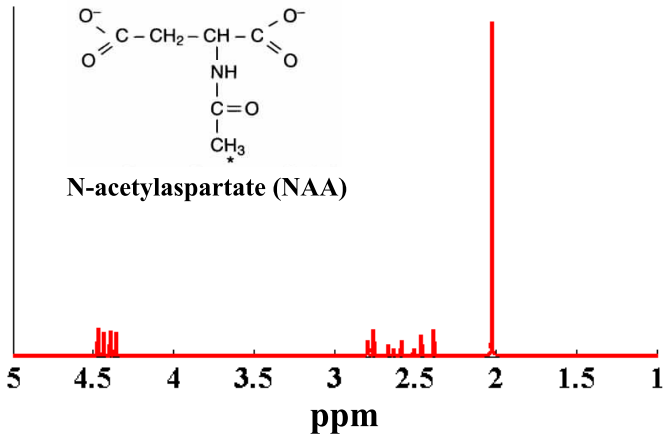

Figure 2.2: The proton NMR spectrum of NAA generated by a quantum mechanical simulation at 3 T field strength (128 MHz) and TE=20 ms. The frequency components between 1 and 5 ppm (parts per million) are shown. The chemical structural of NAA is also shown in the left corner of the image. As can be seen, there are multiple peaks for some of the proton groups due to spin-spin coupling (i.e., J-coupling), which is not discussed in this thesis.

Due to the existence of spins resonating at different frequencies, an intrinsic frequency dimension [1] can be introduced to mathematically describe the signal acquired in the free

induction decay (FID) period (the period after the RF pulse). Assume a spatially homogeneous sample, the FID signal acquired can be modeled as [52]

$$s(t) = \int_{\omega_M} \rho(\omega) e^{-t/T_2(\omega)} e^{-i\omega t} d\omega, \tag{2.11}$$

where $\rho(\omega)$ defines a spectral density function characterizing the frequency distribution and $T_2(\omega)$ captures the relaxation effect. Based on different assumptions for $\rho(\omega)$, different models can then be derived from Eq. (2.11) to analyze and extract information from the FID signal in spectroscopy experiments [14, 52].

Using NMR spectroscopy to study different chemical shift frequencies and the spin densities associated with these frequencies has far-reaching impacts in chemical and biological studies. For example, it has been applied to determine the structures of various macromolecules [54], to quantify metabolic profiles in biological samples in order to detect and characterize diseases [14], and to understand the basic metabolic and physiological processes in the human body. However, for in vivo studies, spectroscopy data acquired from a single large volume of interest is inherently limited by the lack of spatial specificity, which is critical since the metabolic processes in the human body are spatially dependent. Therefore, the concept of spatially-resolved spectroscopy or spectroscopic imaging is introduced to address this problem.

2.2.2 MRSI

MRSI aims to generate spatially-resolved spectroscopic information from the imaging object through combining the spectral encoding during the FID period and spatial encoding using gradients [1, 2, 23]. Since additional frequency dimensions are introduced in MRSI experiments, the measured data $s(\cdot)$ can then be modeled in a (k, t)-space as

$$s\left(\mathbf{k}_m, \mathbf{t}_q\right) = \int_V \int_{\omega_M} \tilde{\rho}\left(\mathbf{r}, \mathbf{f}\right) e^{-i2\pi \mathbf{f}\cdot\mathbf{t}_q} e^{-i\gamma\Delta B(\mathbf{r}) t_{1,q}} e^{-i2\pi \mathbf{k}_m\cdot\mathbf{r}} d\mathbf{f} d\mathbf{r} + \xi\left(\mathbf{k}_m, \mathbf{t}_q\right), \tag{2.12}$$

where $\tilde{\rho}(\mathbf{r}, \mathbf{f})$ is the spatiospectral function of interest (containing both spatial and spectral variations),[5] V denotes the excited volume of interest, ω_M the spectral bandwidth (determined by the range of chemical shift), γ the gyromagnetic ratio, $\Delta B(\mathbf{r})$ the B_0 field inhomogeneity distribution,[6] t_1 the first temporal dimension in $\mathbf{t}$ [14] and $\xi(\cdot)$ the measurement noise (modeled as white Gaussian). When integrated over the frequency domain, Eq. (2.12) can be simplified into

$$s(\mathbf{k}_m, t_q) = \int_V \rho(\mathbf{r}, t_q)\, e^{-i\gamma\Delta B(\mathbf{r})t_q} e^{-i2\pi\mathbf{k}_m\cdot\mathbf{r}} d\mathbf{r} + \xi(\mathbf{k}_m, t_q), \tag{2.13}$$

where $\rho(\mathbf{r}, t)$ is the Fourier counterpart of $\tilde{\rho}(\mathbf{r}, f)$, $\mathbf{k}_m = (m_x\Delta k_x, m_y\Delta k_y, m_z\Delta k_z)$ and $t_q = q\Delta t$. m_x, m_y, m_z and q are the sample indices along different spatial and spectral dimensions. Δk_x, Δk_y, Δk_z and Δt are the corresponding sampling intervals. With the signal models in Eqs. (2.12) and (2.13), the imaging problem in MRSI is to recover $\tilde{\rho}(\mathbf{r}, f)$ or $\rho(\mathbf{r}, t)$ from the set of (k, t)-space measurement $\{s(\mathbf{k}_m, t_q)\}_{m=1,q=1}^{M,Q}$.

CSI

The most common approach to produce the spatiospectral encodings for MRSI is the chemical shift imaging (CSI) method [2] that uses pulsed gradients to phase encode all spatial dimensions after each excitation and uses the entire FID period for spectral encoding. The encoding gradients end at the same time after each excitation to ensure the same initial chemical shift state. Figure 2.3 illustrates some representative sequences for two-dimensional (2D) CSI (extension to 3D is straightforward by adding phase encodings using a third gradient). Given the (k, t)-space data $\{s(\mathbf{k}_m, t_q)\}$ generated by these sequences, and assuming $\tilde{\rho}(\mathbf{r}, f)$ is support limited and bandlimited and $s(\cdot)$ is sampled at the Nyquist rate [52], a truncated Fourier series approximation of $\tilde{\rho}(\mathbf{r}, f)$, $\hat{\tilde{\rho}}(\mathbf{r}, f)$, can be obtained by performing Fourier

[5] The variables $\mathbf{f}$ and $\mathbf{t}$ are expressed here as vectors to take into account multidimensional spectroscopy experiments. The underlying physical principles, i.e., spin coupling, are not considered in this thesis. Accordingly, we will only consider one dimensional spectrum, and replace $\mathbf{f}$ and $\mathbf{t}$ with scalars f and t from now on.

[6] Note that in this thesis, field inhomogeneity is equivalent to B_0 field inhomogeneity unless specified otherwise.

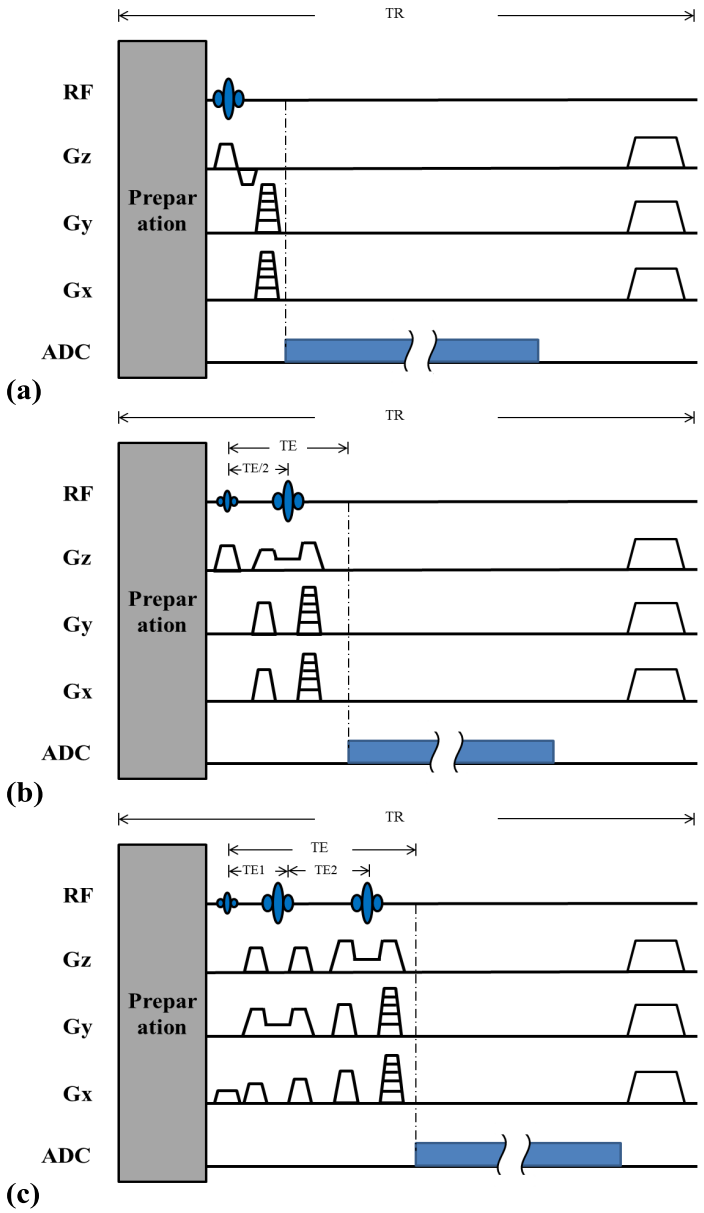

Figure 2.3: Some representative 2D CSI sequences: (a) An FID acquisition scheme with slice-selective excitation; (b) A spin-echo excitation scheme with the same encoding fashion as in (a); (c) A PRESS excitation scheme with the same encoding fashion as in (a) and (b). Note that PRESS excitation provides the capability to selectively excite a region of interest but also limits the choice of echo time and is susceptible to chemical shift displacement [14]. The FID acquisition offers the shortest echo time with SNR benefits but is susceptible to phase errors. The preparation module is application dependent. In ^{1}H-MRSI, for instance, this module typically involves water and lipid suppression pulses with spoiler gradients to reduce the nuisance water and fat signals.

transform on the data

$$\hat{\tilde{\rho}}(\mathbf{r}, f) = \sum_{q=1}^{Q} \sum_{m=1}^{M} s\left(\mathbf{k}_m, t_q\right) e^{i2\pi(\mathbf{k}_m \cdot \mathbf{r} + t_q f)}. \tag{2.14}$$

With a sufficiently large M and Q, this Fourier reconstruction yields accurate results with an optimal SNR efficiency [2, 15]. However, due to the slow encoding fashion of CSI (only one spatial encoding is obtained in each excitation), only very limited M and Q can be acquired in practical experiments, thus leading to significant truncation artifacts and poor spatial resolution. In order to achieve high-resolution MRSI in a short imaging time, accelerated data acquisition is needed.

2.2.3 Accelerated MRSI — A Brief Review

Fast Scanning Methods

One main approach to accelerate MRSI data acquisition is to incorporate echo-planar type of encoding schemes with spectroscopic imaging. These methods, also referred to as echo-planar spectroscopic imaging (EPSI) methods, [15, 23, 24, 27, 33], are characterized by applying spatial encoding gradients during the FID period for simultaneous spatial encoding and spectral encoding. Among them, the Cartesian EPSI is the most used (first proposed in [24] and later further developed by other groups [26, 29, 32, 51]). It uses oscillating gradients to encode one spatial dimension and the temporal spacing between the gradient echoes to encode the spectral dimension after each excitation. This significantly shortens the imaging time. As illustrated by the representative 2D EPSI sequences in Fig. 2.4, the number of excitations needed for $M_x \times M_y$ spatial encodings using CSI (Fig. 2.3) is reduced to M_y (the number of phase encodings), leading to a factor of M_x acceleration.

Another important fast acquisition method is the spiral CSI [27], which plays out a series of repeated short spiral shots during the FID. Each spiral trajectory encodes two spatial dimensions and the time intervals between the trajectories serves as spectral encoding. Several spatial and temporal interleaves (or echo shifts) are often needed to achieve the desired

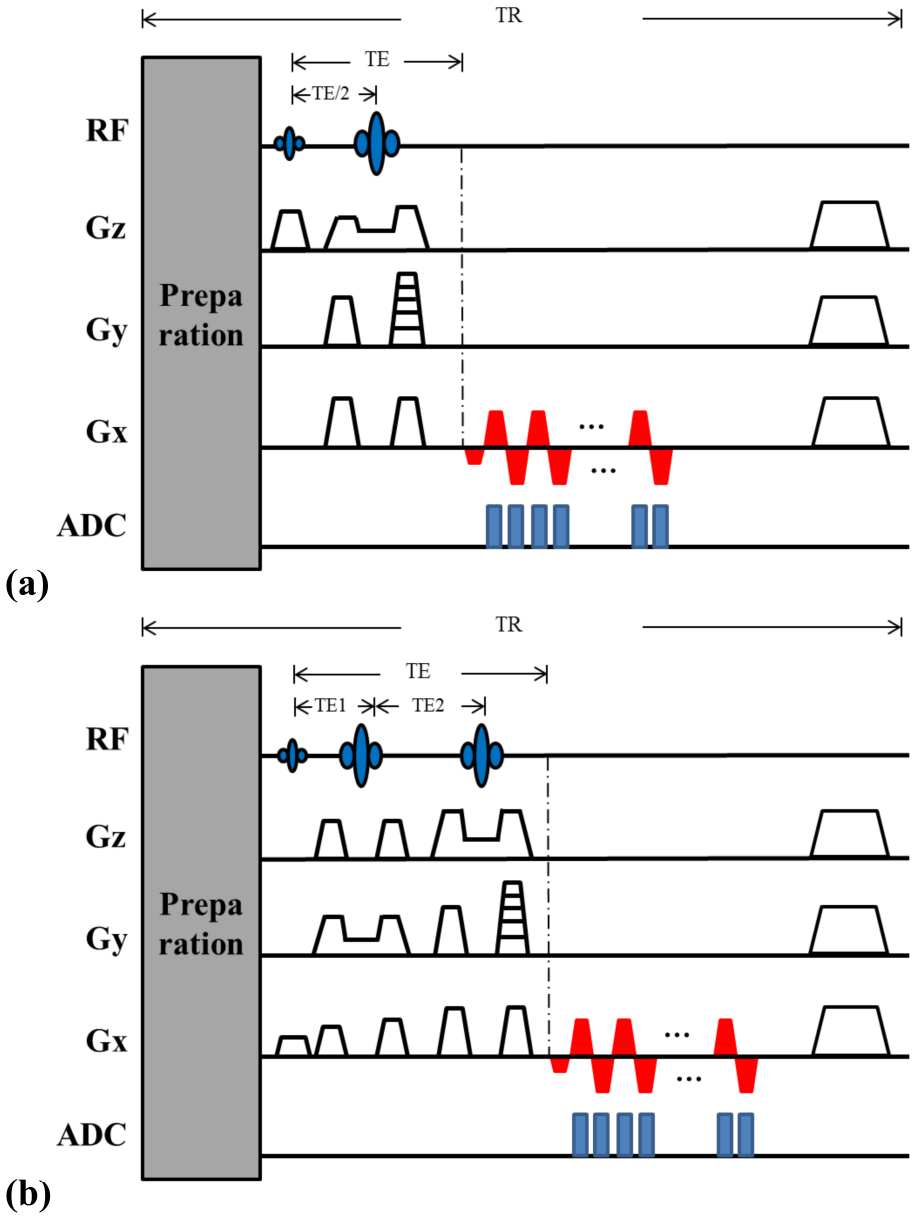

Figure 2.4: Some representative 2D EPSI sequences: (a) A spin-echo excitation scheme with y-direction being the phase encoding direction and (b) A PRESS excitation scheme with the same encoding fashion as in (a). Data are acquired on the plateau of each gradient.

k-space coverage and spectral bandwidth. Since spiral trajectories have higher spatial encoding efficiency, they may be used to further accelerate the spatiospectral encoding for high-resolution MRSI. However, they also pose greater computational challenges due to the non-uniform k-space sampling [55–57].

Although the EPSI-based fast acquisition methods offer higher imaging speed,[7] they require much higher sampling bandwidth (and stronger gradients) which leads to stronger noise. Therefore, the acceleration provided by conventional EPSI sequences is at the expense of SNR, which is a major limitation for in vivo MRSI. Additionally, intensive usage of strong oscillating gradients can cause other practical issues such as field drift (due to gradient heating) which can be detrimental to MRSI experiments [58, 59]. Exiting EPSI-based MRSI methods still limit themselves to a low spatial resolution (voxel size on the order of 1 cc) to maintain sufficient SNR.

Sparse Sampling Methods

Another major approach to accelerate MRSI is to sample limited or sparse data and incorporate constraints into the reconstruction process to compensate the insufficient measurements. In this category, various model/constraints have been proposed in the existing literature. The well-known SLIM-based (spectral localization by imaging) methods model the underlying spatiospectral function as a superposition of several arbitrarily anatomically defined compartments, each of which is homogeneous and has a distinct spectrum, and obtain a localized spectrum for each compartment from a set of limited data [34, 39, 60, 61]. Other methods that make use of anatomical prior for improved MRSI reconstruction can be found in [35–38].

Motivated by the recent success in sparse signal recovery (compressed sensing) [62–65] and its application to accelerated MRI [66–69], a number of methods have been proposed to use sparse and low-rank model based regularization for either super-resolution reconstruction from low-resolution MRSI data or reconstruction from undersampled data (examples include [40–45]). Furthermore, based on knowledge about the spectral structures of different metabolites, explicit parametric models [41, 46] have also been used for MRSI reconstruction from limited or undersampled data. It is important to note that compressed sensing based sparse sampling methods require high SNR data for joint subspace pursuit and missing data

[7] Here we categorize both spiral and radial MRSI methods as EPSI because they are derived from a similar methodology that is using gradients to simultaneously encode spatial and spectral information during the FID period and ignoring the chemical shift evolution during each readout for reconstruction.

recovery. Therefore, while such an approach is useful for hyperpolarized ^{13}C-MRSI [40, 42], it offers limited accelerations for regular MRSI experiments.

In the next section, a new mathematical model will be introduced, which allows us to develop new approaches to both data acquisition and image reconstruction to enable fast, high-resolution MRSI with high SNR.

2.3 Partial Separability and Low-Rank Tensor Model

In this section, we review the fundamental mathematical concepts which this thesis is built upon. In particular, we discuss the theories and applications of partially separable functions (PSF) [70] that lead to the subspace model underlying the proposed data acquisition, processing and reconstruction strategies for high-resolution MRSI.

Consider a multivariate image function of interest $f(x_1, x_2, \cdots, x_D)$; the degrees-of-freedom for an imaging problem grow exponentially as D increases, inevitably prolonging the data acquisition time and/or limit the achievable resolution. To address this fundamental challenge for multi-dimensional imaging, efficient representation of $f(x_1, x_2, \cdots, x_D)$ is necessary. In this line of pursuit, the PSF-based model (also referred to as the partial separability model) proposed by Liang in [47] is among the most influential. Specifically, the partial separability (PS) model approximates the multi-dimensional $f(\cdot)$ as

$$f(\mathbf{x}_1, \mathbf{x}_2, \cdots, \mathbf{x}_d) \approx \sum_{l_1=1}^{L_1} \sum_{l_2=1}^{L_2} \cdots \sum_{l_d=1}^{L_d} c_{l_1,l_2,\cdots,l_d} \phi_{l_1}(\mathbf{x}_1) \phi_{l_2}(\mathbf{x}_2) \cdots \phi_{l_d}(\mathbf{x}_d), \tag{2.15}$$

where $[\mathbf{x}_1, \mathbf{x}_2, \cdots, \mathbf{x}_d]$ are d separable groups of $[x_1, x_2, \cdots, x_D]$ with $\mathbf{x}_i = [x_{i_1}, x_{i_2}, \cdots, x_{i_m}]$ and L_1 to L_d correspond to the model orders. In the context of imaging, each group can contain variables with the same physical meaning. For example, for $d = 2$, $\mathbf{x}_1$ can include the spatial variables and $\mathbf{x}_2$ can include the temporal variables or some parametric dimensions result from different image acquisition parameters. The representation in Equation (2.15) is

an extension of the Lth-order separable functions

$$f(x_1, x_2, \cdots, x_D) = \sum_{l_1=1}^{L_1} \sum_{l_2=1}^{L_2} \cdots \sum_{l_D=1}^{L_D} c_{l_1,l_2,\cdots,l_D} \phi_{l_1}(x_1)\phi_{l_2}(x_2)\cdots\phi_{l_D}(x_D), \tag{2.16}$$

which is mathematically justified by the following theorem [47, 71].

Theorem 2.1 *Let $\mathbf{X}_1$ and $\mathbf{X}_2$ be two measure spaces and $\mathbf{X}_1 \times \mathbf{X}_2$ be the Cartesian product of $\mathbf{X}$ and $\mathbf{X}_2$. Let $\mathcal{H}$ be the set of square integrable functions defined on $\mathbf{X}_1 \times \mathbf{X}_2$, i.e., $\mathcal{H} = L^2(\mathbf{X}_1 \times \mathbf{X}_2)$, then the set of all the functions in the form of $\sum_{l=1} \phi_l(x_1)\psi_l(x_2)\ \forall\ \phi_l(x_1) \in L^2(\mathbf{X}_1)$ and $\psi_l(x_2) \in L^2(\mathbf{X}_2)$ is dense in $\mathcal{H}$. Thus, for any $f(x_1, x_2) \in \mathcal{H}$, and appropriately defined $\phi_l(\cdot)$ and $\psi_l(\cdot)$*

$$\left\| f(x_1, x_2) - \lim_{L\to\infty} \sum_{l=1}^{L} \phi_l(x_1)\psi_l(x_2) \right\|_2 = 0.$$

The definitions and results in this theorem can be generalized to more than two measure spaces. Since it is safe to assume that any function of interest ($f(x_1, x_2, \cdots, x_D)$) for an imaging problem belongs to $L^2(\mathbf{X}_1 \times \mathbf{X}_2 \cdots \times \mathbf{X}_D)$, the above theorem ensures that as L goes to infinity, the PS model can approximate f to arbitrary accuracy. Furthermore, using the more general PS model in the form of Eq. (2.15) instead of Eq. (2.16) often leads to significantly smaller L necessary for accurate approximation in imaging problems. More importantly, it offers better physical interpretation and allows for more flexible acquisition designs than conventional imaging paradigms [47, 48, 50, 72–74].

It has also been shown that PS model implies low-rank representation, which has been used in different areas of signal and image processing [47, 75–77]. Specifically, given a point set $\{\mathbf{x}_{1,i_1}, \mathbf{x}_{2,i_2}, \cdots, \mathbf{x}_{d,i_d}\}_{i_1,i_2,\cdots,i_d=1}^{N_1,N_2,\cdots,N_d}$, the multi-linear array $\mathbf{T}$ formed as

$$\mathbf{T}_{i_1,i_2,\cdots,i_d} = f(\mathbf{x}_{1,i_1}, \mathbf{x}_{2,i_2}, \cdots, \mathbf{x}_{d,i_d})$$

is a low-rank tensor [78, 79]. Particularly, when $d = 2$ and given $\mathbf{x}_1 = \mathbf{r}$, $\mathbf{x}_2 = t$, if the

function $f(\mathbf{r},t)$ has the PS representation as[8]

$$f(\mathbf{r},t)=\sum_{l=1}^{L}c_l(\mathbf{r})\phi_l(t), \tag{2.17}$$

the Casorati matrix formed from $f(\mathbf{r},t)$ over any point set $\{(\mathbf{r}_p,t_q)\}_{p,q=1}^{P,Q}$

$$\mathcal{C}\left(\{f(\mathbf{r}_p,t_q)\}_{p,q=1}^{P,Q}\right) = \begin{bmatrix} f(\mathbf{r}_1,t_1) & f(\mathbf{r}_1,t_2) & \cdots & f(\mathbf{r}_1,t_Q) \\ f(\mathbf{r}_2,t_1) & f(\mathbf{r}_2,t_2) & \cdots & f(\mathbf{r}_2,t_Q) \\ \vdots & \vdots & \ddots & \vdots \\ f(\mathbf{r}_P,t_1) & f(\mathbf{r}_P,t_2) & \cdots & f(\mathbf{r}_P,t_Q) \end{bmatrix} \tag{2.18}$$

has a rank upper-bounded by L [47]. This implies that the original high-dimensional signal (with dimensionality $P\times Q$) can be specified by a much smaller number of degrees-of-freedom (e.g., $(P+Q)\times L$), which is extremely useful in the context of multi-dimensional imaging. More specifically, it means that with the PS model the number of measurements required for accurately estimating the unknown image function of interest dramatically decreases. Moreover, the decoupled structure for different variables offered by the PS model enables the design of a richer class of strategies for encoding and decoding $f(\cdot)$, of which the work to be presented in this thesis is an excellent example.

The PS/low-rank model has been successfully applied to several MR imaging applications. Examples include sparse sampling for real-time cardiac imaging [72, 80–82], flow imaging [83], dynamic speech imaging [74], fast MR relaxometry [84], functional imaging [85, 86], accelerated MR elastography [87], and denoising for high-resolution diffusion imaging [88,89] and spectroscopic imaging [43, 49].

[8]We choose $\mathbf{r}$ and t because they have specific physical meaning in imaging applications. For example, in dynamic imaging, $\mathbf{r}$ typically represents the spatial dimensions and t the temporal dimension. For spectroscopic imaging, t denotes the axis for the FID signal evolution. Furthermore, it is easy to show that the general PS model in Eq. (2.15) reduces to the form in Eq. (2.17) when $d=2$.

2.4 Cramér-Rao Bound

Consider the problem of estimating an unknown $N \times 1$ parameter vector $\boldsymbol{\theta}$ from a set of measurements $\mathbf{d}$ generated by a signal model (dependent on $\boldsymbol{\theta}$) as

$$\mathbf{d} \quad = \quad g(\boldsymbol{\theta}, \boldsymbol{\xi}), \tag{2.19}$$

where $g(\cdot)$ characterizes the data generation process and $\boldsymbol{\xi}$ represents the randomness in the data, e.g., noise. A commonly used noise model is the additive noise such that Eq. (2.19) can be written as

$$\mathbf{d} \quad = \quad g(\boldsymbol{\theta}) + \boldsymbol{\xi}, \tag{2.20}$$

where elements in $\boldsymbol{\xi}$ follow i.i.d. distributions. The Cramér-Rao Bound (CRB) [90] provides a fundamental limit on the performance of any unbiased estimator of $\boldsymbol{\theta}$ ($\hat{\boldsymbol{\theta}}$) obtained from $\mathbf{d}$. Specifically, it states that [91]

$$\Sigma_{\hat{\boldsymbol{\theta}}} \quad \geq \quad \mathbf{J}_{\boldsymbol{\theta}}^{\dagger}, \tag{2.21}$$

where $\Sigma_{\hat{\boldsymbol{\theta}}}$ is the covariance matrix of the estimate $\hat{\boldsymbol{\theta}}$ and $\dagger$ denotes the pseudoinverse.[9] $\mathbf{J}_{\boldsymbol{\theta}}$ is the Fisher information matrix (FIM) that is dependent on $g(\boldsymbol{\theta})$ and $\boldsymbol{\xi}$ and can be calculated as [91]

$$(\mathbf{J}_{\boldsymbol{\theta}})_{i,j} \quad = \quad E\left[\left(\frac{\partial \log p(\mathbf{d};\boldsymbol{\theta})}{\partial \boldsymbol{\theta}_i}\right)\left(\frac{\partial \log p(\mathbf{d};\boldsymbol{\theta})}{\partial \boldsymbol{\theta}_j}\right) \mid \boldsymbol{\theta}\right], \tag{2.22}$$

where $p(\mathbf{d};\boldsymbol{\theta})$ is the likelihood function of $\mathbf{d}$ given a particular $\boldsymbol{\theta}$ (assuming finite second moment), $E(\cdot)$ denotes the expectation and $(\mathbf{J})_{i,j}$ the element of $\mathbf{J}$ at the ith row and the jth column. Moreover, it can be shown that the variance for each element in $\hat{\boldsymbol{\theta}}$ is lower

[9] Given two matrices $\mathbf{A}$ and $\mathbf{B}$, $\mathbf{A} \geq \mathbf{B}$ means $\mathbf{A} - \mathbf{B}$ is a positive semidefinite matrix.

bounded by

$$(\Sigma_{\hat{\boldsymbol{\theta}}})_{i,i} \;\geq\; \left(\mathbf{J}_{\boldsymbol{\theta}}^{\dagger}\right)_{i,i}, \text{ for } i = 1, 2, \cdots, N. \tag{2.23}$$

If $\boldsymbol{\theta}$ can be further assumed to reside in a constrained parameter space Ω_C, the following constrained CRB can be derived for any locally unbiased estimator of $\boldsymbol{\theta}$ [92]:

$$\Sigma_{\hat{\boldsymbol{\theta}}} \;\geq\; \mathbf{R}\left[\mathbf{R}^H \mathbf{J}_{\boldsymbol{\theta}} \mathbf{R}\right]^{\dagger} \mathbf{R}^H, \tag{2.24}$$

where $\mathbf{R}$ is a matrix with columns spanning the same subspace as the set of $N \times 1$ vectors $\{\boldsymbol{\nu}_s\}_{s=1}^{S}$, which satisfy

$$\{\boldsymbol{\theta}_s = \boldsymbol{\theta} + \Delta_s \boldsymbol{\nu}_s\} \in \Omega_C \;, \tag{2.25}$$

for any sufficiently small Δ_s. When $\Omega_C = \mathbb{R}^N$ or $\mathbb{C}^N$, the constrained CRB becomes the conventional CRB. Generalizations of Eqs. (2.21) and (2.24) for biased estimators can be found in the literature, e.g., [92–94]. CRB and constrained CRB analysis have been widely used in many signal processing problems [91]. In the field of imaging, they have been shown very useful in analyzing and characterizing different image reconstruction models [95–97], parameter quantification methods [98–100] and also in optimizing data acquisition designs [101–104].

For the special case where the signal follows the linear Gaussian measurement model as

$$\mathbf{d} \;=\; \mathbf{A}\boldsymbol{\theta} + \boldsymbol{\xi}, \tag{2.26}$$

where $\mathbf{A}$ is the measurement matrix and $\boldsymbol{\xi}$ contains white Gaussian noise with mean zero and variance σ^2, the likelihood function is a joint Gaussian distribution with the form of

$$p(\mathbf{d}; \boldsymbol{\theta}) = \frac{1}{(2\pi)^{N/2}\sigma^N} \exp\left(-\frac{\|\mathbf{d} - \mathbf{A}\boldsymbol{\theta}\|_2^2}{2\sigma^2}\right). \tag{2.27}$$

Accordingly, the FIM for the model in Eq. (2.26) can be derived as

$$\mathbf{J}_{\boldsymbol{\theta}} = \frac{1}{\sigma^2}\mathbf{A}^H\mathbf{A}. \tag{2.28}$$

In this thesis, we will apply Eqs. (2.26) and (2.28) to obtain a theoretical analysis of the proposed model and to optimize the proposed data acquisition methods.

CHAPTER 3

SPECTROSCOPIC IMAGING BY EXPLOITING SPATIOSPECTRAL CORRELATION (SPICE)

In this chapter, we describe the proposed subspace approach to high-resolution spectroscopic imaging, coined SPICE (Spectroscopic Imaging by Exploiting Spatiospectral Correlation). The signal model, subspace-driven data acquisition strategies and reconstruction framework of SPICE will be presented.

3.1 Subspace Model

To recover the underlying spatiotemporal/spatiospectral function of interest with high resolution and high SNR, SPICE exploits the spatiotemporal partial separability (PS) [47] of the spectroscopic signals $\rho(\mathbf{r},t)$ (considering only one spectral dimension) and models it as [49, 50]

$$\rho(\mathbf{r},t) \;=\; \sum_{l=1}^{L} c_l(\mathbf{r})\phi_l(t), \tag{3.1}$$

where $\{\phi_l(t)\}_{l=1}^{L}$ represents a set of temporal basis functions, $\{c_l(\mathbf{r})\}_{l=1}^{L}$ contains the corresponding spatial coefficients, and L is the model order. The model in Eq. (3.1) can be further extended to include multiple components in experimentally acquired spectroscopic data (i.e., a union-of-subspaces model [105]) as

$$\rho_m(\mathbf{r},t)+\rho_b(\mathbf{r},t)+\rho_{ns}(\mathbf{r},t) = \sum_{l_m=1}^{L_m} c_{l_m}(\mathbf{r})\phi_{l_m}(t) + \sum_{l_b=1}^{L_b} c_{l_b}(\mathbf{r})\phi_{l_b}(t) + \sum_{l_{ns}=1}^{L_{ns}} c_{l_{ns}}(\mathbf{r})\phi_{l_{ns}}(t), \tag{3.2}$$

where $\{\phi_{l_m}(t)\}_{l_m=1}^{L_m}$, $\{\phi_{l_b}(t)\}_{l_b=1}^{L_b}$ and $\{\phi_{l_{ns}}(t)\}_{l_{ns}=1}^{L_{ns}}$ denote the temporal subspaces for the metabolite signal of interest (ρ_m), the baseline signal (ρ_b) and the nuisance signals (ρ_{ns})

with dimensions L_m, L_b and L_{ns}, respectively. $\{c_{l_m}(\mathbf{r})\}$, $\{c_{l_b}(\mathbf{r})\}$, and $\{c_{l_{ns}}(\mathbf{r})\}$ denote their corresponding spatial coefficients. In particular, for ^{1}H-MRSI experiments focused on in this thesis, the nuisance signals can be decomposed into the water and subcutaneous fat components as[1]

$$\sum_{l_{ns}=1}^{L_{ns}} c_{l_{ns}}(\mathbf{r})\phi_{l_{ns}}(t) \;=\; \sum_{l_w=1}^{L_w} c_{l_w}(\mathbf{r})\phi_{l_w}(t) + \sum_{l_f=1}^{L_f} c_{l_f}(\mathbf{r})\phi_{l_f}(t). \tag{3.3}$$

In spectroscopic imaging, the above PS representations can be justified from different perspectives, e.g., the object being imaged has only a finite (L) number of tissue types, each of which has a distinct spectral structure, or $\tilde{\rho}\,(\mathbf{r}, f)$ has only a finite number (L) of spectral components which are linearly combined to generate the spectrum at a particular voxel. It can also be justified from the theory of quantum mechanics that the solution of the Schrödinger equation describing the chemical-shift effects has a partially separable form. Accordingly, assuming that $\rho(\mathbf{r}, t)$ can be specified by $\{\rho\,(\mathbf{r}_n, t_q)\}_{n,q=1}^{N,Q}$ in the conventional pixel representation given a high-resolution point set $\{(\mathbf{r}_n, t_q)\}_{n,q=1}^{N,Q}$, SPICE, based on the PS theory, models the Casorati matrix ($\boldsymbol{\rho}$) for each component in Eq. (3.2) as a low-rank matrix. For instance, $\boldsymbol{\rho}_m$ (formed from $\{\rho_m\,(\mathbf{r}_n, t_q)\}$) is expressed as

$$\boldsymbol{\rho}_m \;=\; \mathbf{C}_m\boldsymbol{\Phi}_m, \tag{3.4}$$

where $\boldsymbol{\Phi}_m = \{\phi_{l_m}(t_q)\}$ and $\mathbf{C}_m = \{c_{l_m}(\mathbf{r}_n)\}$ are rank-L_m matrices (with $L_m < \min\{N, Q\}$). This implies that, when viewed as a vector, $\boldsymbol{\rho}_m$ actually resides in a very low-dimensional subspace (spanned by $\{\phi_{l_m}(t)\}$, for example), which also means that $\boldsymbol{\rho}_m$ has a much smaller number of degrees-of-freedom compared to its original NQ-dimensional representation. More importantly, this low-dimensional subspace model enables special data acquisition and image reconstruction strategies to be used to obtain high-resolution spatiospectral distributions with good SNR.

[1] Although baseline signal, attributed to macromolecules such as nucleic acids, proteins, and lipids, is usually considered to be nuisance signal, we separate it from the nuisance water and subcutaneous fat signals because (i) they have highly distinct signal characteristics which require different processing treatments; (ii) the magnitude of baseline signal is orders of magnitude weaker than that of water and fat.

It is important to note that the nuisance water and fat signals (ρ_{ns}) are much stronger (even with water and lipid suppression in the pulse sequences) than the metabolite signal. Therefore, preprocessing is typically required to remove them from the acquired signal first to ensure accurate estimation of the spatiospectral distribution of the metabolites. Additional prior information is also needed for accurately determining the temporal subspaces ($\{\phi_{l_w}(t)\}$ and $\{\phi_{l_f}(t)\}$) and the corresponding spatial coefficients ($\{c_{l_w}(\mathbf{r})\}$ and $\{c_{l_f}(\mathbf{r})\}$) for water and fat [105]. Note also that whether to include the ρ_b component in the reconstruction is dependent on the imaging parameters. For example, the baseline signal is normally negligible for echo times greater than 40 ms.

In the following sections, the data acquisition and image reconstruction strategies for SPICE will be described.

3.2 Data Acquisition: Sparse Sampling of (k, t)-Space

To exploit the PS property for high-resolution spectroscopic imaging, SPICE uses a special subspace-driven data acquisition (or spatiospectral encoding) strategy to achieve extended (k, t)-space coverage with sparse sampling. The data acquisition scheme has two key features: (a) acquisition of a data set, $\mathcal{D}_1$ (with limited k-space coverage but dense temporal sampling), for determination of the temporal basis $\{\phi_l(t)\}$ (with fully specified spectral information), and (b) acquisition of a data set, $\mathcal{D}_2$ (with extended k-space coverage but sparse temporal sampling), for determination of the spatial coefficients $\{c_l(\mathbf{r})\}$ (with the desired spatial resolution).[2] Figure 3.1 illustrates an example of such a sampling strategy, which can be implemented using a hybrid CSI/EPSI pulse sequence shown in Fig. 3.2. As illustrated, the CSI component is used to generate $\mathcal{D}_1$ (with high SNR) while the EPSI-like component is used to generate $\mathcal{D}_2$ (with high data acquisition speed and extended k-space coverage). More specifically, the EPSI-like scan encodes two spatial dimensions (with the k_x axis perpendicular to the paper) during the FID period (in contrast to traditional EPSI sequences that usually encode one spatial dimension [24]) and uses echo shifts (in different excitations)

[2] We drop the subscript in l for different signal components for a general data acquisition and reconstruction discussion.

for additional spectral encoding. As a result, this SPICE acquisition strategy samples the (k,t)-space only sparsely. This sparse sampling scheme is enabled by the PS model with temporal basis capturing the full spectral information. Moreover, since the CSI only has a small number of spatial encodings and the EPSI-like component has high encoding efficiency, this type of acquisition strategy can significantly accelerate the overall spatiospectral encoding for high-resolution MRSI.

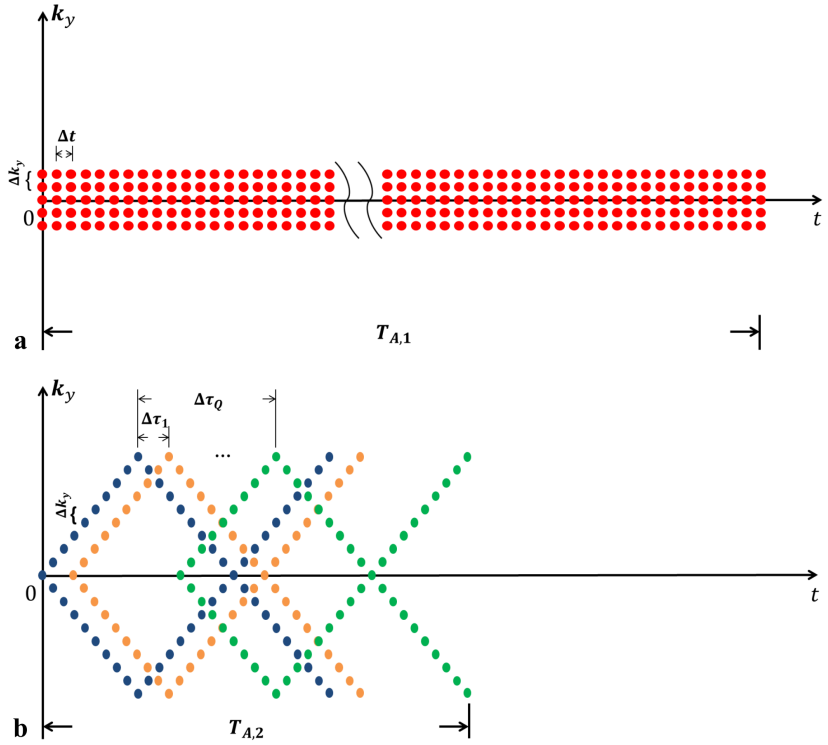

Figure 3.1: An example of SPICE (k,t)-space sampling for 2D spectroscopic imaging (with k_x pointing into the page): (a) (k,t)-space sampling for data in $\mathcal{D}_1$ for subspace estimation. $\mathcal{D}_1$ covers only a limited region of central k-space (based on SNR consideration), and sample the FID period ($T_{A,1}$) fully (to capture the spectral information); (b) (k,t)-space sampling for data in $\mathcal{D}_2$ for determination of the spatial coefficients. Note that a set of FIDs with different echo shifts $(\Delta\tau_1, \Delta\tau_2, \cdots, \Delta\tau_q)$ is collected, each of which traverses the entire k-space but with limited spectral encoding ($T_{A,2} < T_{A,1}$).

The proposed SPICE acquisition strategy also offers a range of flexibility for generating both $\mathcal{D}_1$ and $\mathcal{D}_2$. For example, the acquisition of $\mathcal{D}_1$ can be done using the conventional EPSI sequence if further acceleration is needed. The acquisition of $\mathcal{D}_2$ can also be done using alternative (k,t)-space trajectories, e.g., the traditional EPSI trajectories or spiral-

like trajectories as shown in Fig. 3.3. However, note that given the subspace model, each readout in these trajectories (for $\mathcal{D}_2$) need not be treated as instantaneously sampled as in conventional EPSI or spiral CSI methods (e.g., [15, 24, 27, 28]). Detailed discussion of the design of specific pulse sequences to implement the SPICE acquisition strategy for practical MRSI experiments will be given in Chapter 4.

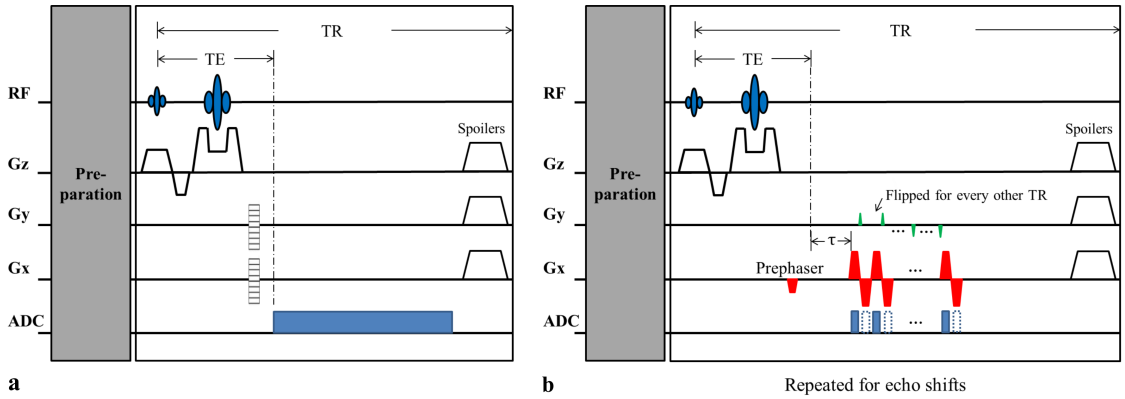

Figure 3.2: A prototypical sequence for realizing the SPICE sampling pattern in Fig. 3.1: (a) the CSI component used to collect the data in $\mathcal{D}_1$ with limited k-space coverage but full spectral encoding, and (b) the EPSI-like component used to acquire the data in $\mathcal{D}_2$ with extended k-space coverage but limited spectral encoding. Note that there is only one k_y reversal in each TR due to SNR consideration, although more k_y reversals can be included in principle. Note also that acquiring data on both polarities of the gradients improves encoding efficiency (as illustrated in this figure) but requires additional correction if all the acquired data are used.

3.3 Reconstruction from Sparse Data

Given the two data sets described above, special reconstruction strategy can be designed for SPICE image reconstruction. For notation convenience, we assume that $\mathcal{D}_1 = \{s_1(\mathbf{k}_n, t_q)\}_{n,q=1}^{N_1,Q_1}$ and $\mathcal{D}_2 = \{s_2(\hat{\mathbf{k}}_n, \hat{t}_q)\}_{n,q=1}^{N_2,Q_2}$. According to the descriptions in the previous chapter, we have: (a) $\{t_q\}_{q=1}^{Q_1}$ sample the time interval of interest in high resolution while $\{\hat{t}_q\}_{q=1}^{Q_2}$ sample the interval sparsely, and (b) $\{\mathbf{k}_n\}_{n=1}^{N_1}$ cover limited k-space locations while $\{\hat{\mathbf{k}}_n\}_{n=1}^{N_2}$ cover an extended region of k-space (to provide the desired spatial resolution). With these data, SPICE reconstructs $\rho(\mathbf{r}, t)$ using a two-step procedure: (a) determination of the temporal basis from $\mathcal{D}_1$, and (b) determination of the spatial coefficients from $\mathcal{D}_2$.

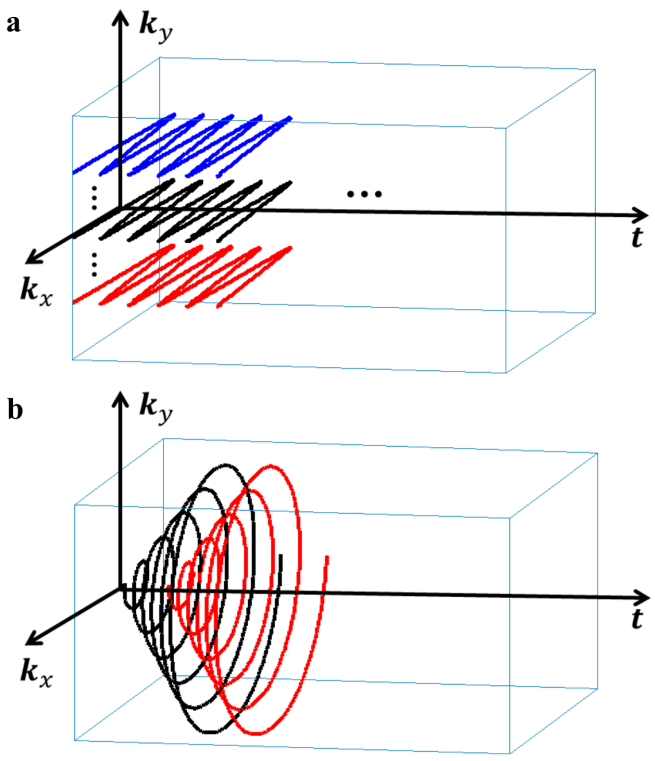

Figure 3.3: Two alternative (k,t)-space sampling trajectories that can be used to generate $\mathcal{D}_2$: (a) conventional EPSI trajectories, and (b) spiral trajectories. Note that in (a), the echo spacing is not necessarily constrained by the spectral Nyquist criterion as in traditional EPSI schemes. In both cases, different colors represent trajectories for different excitations.

Determination of the temporal basis (or temporal subspace), $\{\phi_l(t_q)\}_{l=1}^{L}$ for $q = 1, 2, \cdots, Q_1$, from $\mathcal{D}_1$ is fairly easy if the effect of field inhomogeneity $\Delta B(\mathbf{r})$ on $s_1(\mathbf{k}_n, t_q)$ is negligible. In practice, $\Delta B(\mathbf{r})$ can be significant, and we need to first remove/reduce its effect on s_1. Assuming that $\Delta B(\mathbf{r})$ is available (which can be acquired during the MRSI experiment), field inhomogeneity correction on limited k-space spectroscopic data can be done by using different methods (e.g., [106–108]). The corrected data, denoted as $\hat{s}_1(\mathbf{k}_n, t_q)$, can then be used to form an $N_1 \times Q_1$ Casorati matrix $\boldsymbol{\mathcal{C}}\left(\{\hat{s}_1(\mathbf{k}_n, t_q)\}_{n,q=1}^{N_1,Q_1}\right)$, to which the SVD is applied. The resulting first L principal right singular vectors are then chosen as $\boldsymbol{\Phi}$ (with $\boldsymbol{\Phi}_{lq} = \phi_l(t_q)$). In this chapter, we will use the method in [108] for field correction to demonstrate the concept of SPICE. A more comprehensive discussion of field correction on limited k-space data through regularized reconstruction will be presented in Chapter 5.

After $\mathbf{\Phi}$ is determined, the spatial coefficients, $\{c_l(\mathbf{r}_n)\}_{l=1}^{L}$, can be determined from the sparse data in $\mathcal{D}_2$ by solving a least-squares problem. Based on the low-rank representation in Eq. (3.4), we rewrite the spatiotemporal function of interest as

$$\{\rho(\mathbf{r}_n, t_q)\}_{n,q=1}^{N,Q} = \{\sum_{l=1}^{L} c_l(\mathbf{r}_n)\phi_l(t_q)\}_{n,q=1}^{N,Q} = \mathbf{C}\mathbf{\Phi}$$

with $\mathbf{C} \in \mathbb{C}^{N\times L}$ and $\mathbf{\Phi} \in \mathbb{C}^{L\times Q}$ such that $\mathbf{C}_{nl} = c_l(\mathbf{r}_n)$ and $\mathbf{\Phi}_{lq} = \phi_l(t_q)$. For the proposed data acquisition scheme, we have $N = N_2$ and $Q = Q_1$. Accordingly, we can construct a discretized acquisition model for the data in $\mathcal{D}_2$ as

$$\mathbf{s}_2 = \mathcal{F}_\Omega\{\mathbf{B} \odot \mathbf{C}\mathbf{\Phi}\} + \boldsymbol{\xi}, \tag{3.5}$$

where $\mathbf{s}_2 \in \mathbb{C}^{N_2Q_2\times 1}$ denotes the vector containing all the data in $\mathcal{D}_2$, $\mathcal{F}_\Omega$ represents the Fourier encoding operator with a (k,t)-space sampling pattern Ω for $\mathcal{D}_2$, $\mathbf{B}$ is a matrix containing phase terms modeling the B_0 field inhomogeneity effect described in Eq. (2.13), $\odot$ denotes a point-wise multiplication operation, and $\boldsymbol{\xi}$ is a vector containing the measurement noise (assumed to be white Gaussian). The spatial coefficients, $\mathbf{C}$, can be determined by solving

$$\hat{\mathbf{C}} \;=\; \arg\min_{\mathbf{C}} \|\mathbf{s}_2 - \mathcal{F}_\Omega\{\mathbf{B} \odot \mathbf{C}\mathbf{\Phi}\}\|_2^2 + \lambda R\left(\mathbf{C}\right), \tag{3.6}$$

where the $\|\cdot\|_2^2$ term measures the data consistency of a reconstruction and $R(\cdot)$ is a regularization functional with regularization parameter λ. There are many choices for $R(\cdot)$ to incorporate prior information about $\rho\left(\mathbf{r}, t\right)$ or $\tilde{\rho}(\mathbf{r}, f)$ (including both quadratic and sparsity-promoting penalties [37, 38, 41, 43]) for improved estimation. In this chapter, we focus on demonstrating the concept and potential of SPICE and use the following ℓ_2 regularization:

$$R\left(\mathbf{C}\right) = \|\mathbf{W}\mathbf{D}\mathbf{C}\mathbf{\Phi}\|_F^2, \tag{3.7}$$

for simulation studies. In Eq. (3.7), $\mathbf{D}$ is a finite difference operator and $\mathbf{W}$ contains edge weights derived from a high-resolution reference image (as in [37]). Integrating this regu-

larization term into Eq. (3.6) yields a weighted-ℓ_2 regularized least-squares problem that can be solved efficiently (e.g., using the linear conjugate gradient method). The use of more sophisticated regularization functional for improved reconstruction will be presented in Chapter 5.

3.4 Analysis and Characterization

In the acquisition and reconstruction strategies described above, a number of parameters play important roles in determining the performance of SPICE. In this section, we will analyze the effects of these parameters for optimized SPICE data acquisition and reconstruction through theoretical calculation and/or simulation studies. In particular, we will discuss the sampling requirements for $\mathcal{D}_1$ and $\mathcal{D}_2$, and the optimization of spectral encoding for the acquisition of $\mathcal{D}_2$.

3.4.1 Sampling Requirements for $\mathcal{D}_1$ and $\mathcal{D}_2$

Given the subspace model with model order L, the number of spatial encodings in $\mathcal{D}_1$ theoretically has at least to be greater than L, i.e., $N_1 \geq L$. This can be shown using the low-rank model in Eq. (3.4). Consider the matrix representation of the underlying spatiotemporal function, $\boldsymbol{\rho}$ with $\text{rank}(\boldsymbol{\rho}) = L$, and the property of $\mathcal{D}_1$ (i.e., the same k-space area is covered for all the time points); the sampled data $\mathbf{S}_1$ can be expressed as (in the noiseless case)

$$\mathbf{S}_1 \quad = \quad \mathbf{A}\boldsymbol{\rho}, \tag{3.8}$$

where $\mathbf{A}$ is an $M \times N$ encoding matrix ($M < N$) that is the same for all the columns in $\boldsymbol{\rho}$ (ignoring field inhomogeneity). Since the row space of $\mathbf{S}_1$ is a subspace of the row space of $\boldsymbol{\rho}$ (with dimensionality L), the number of rows in $\mathbf{S}_1$ has at least to be larger than L in order to span the same row space as $\boldsymbol{\rho}$. This is easy to satisfy since L is typically a small number [49,50]. Moreover, given an arbitrary rank-L $\boldsymbol{\rho}$, N_1 needs to be larger than a certain

threshold to ensure that

$$\text{rank}(\mathbf{S}_1^H \mathbf{S}_1) \quad = \quad L, \tag{3.9}$$

i.e., $\mathbf{S}_1$ has the same row space as $\boldsymbol{\rho}$. A theoretical threshold on N_1 for this condition to hold can be found in [109], which studied the singular value and singular vector relationships between two matrices connected by the model in Eq. (3.8). With the condition in Eq. (3.9) held, unique (or accurate) subspace recovery from $\mathbf{S}_1$ can be guaranteed. Considering the theoretical bound (e.g., the one in [109]) is hard to calculate in practice, we aim to understand this issue through carefully designed simulation studies. Meanwhile, it is important to note that the choice of N_1 in practical experiments will also be affected by other factors, such as noise, field inhomogeneity correction and nuisance signal removal. We will discuss the effects of noise and field inhomogeneity in Section 3.5 and field correction and nuisance signal removal in Chapter 5.

As for $\mathcal{D}_2$, it is understood that the corresponding k-space coverage needs to provide the desired spatial resolution. However, how many temporal samples are needed for each k-space point remains an important question. With the temporal subspace estimated, we perform a CRB analysis on the spatial coefficient estimation problem to answer this question. Given the model in Eq. (3.5) with the existence of B_0 field inhomogeneity, the CRB can be obtained by computing the joint FIM for all the spatial coefficients. However, this will involve intensive computations and memory usage.[3] Therefore, to simplify the computation, we first ignore the field inhomogeneity, which enables the analysis using a point-by-point fitting model (in k-space). This analysis, although simplified, suffices in understanding the effects of the number of temporal samples per k-space point given a particular sampling trajectory design. Specifically, assume the temporal basis $\boldsymbol{\Phi} \in \mathbb{C}^{L \times Q}$ is given; a fitting matrix $\boldsymbol{\Phi}_k \in \mathbb{C}^{M_e \times L}$ can be constructed by selecting M_e columns of $\boldsymbol{\Phi}$ corresponding to the temporal sampling grids for different k-space locations, where M_e denotes the number of temporal samples.

[3] For a $\mathbf{C}$ with the size of $N \times L$, the size of the FIM will be $N^2 \times L^2$.

Accordingly, for the data acquired at k_0, denoted as $\mathbf{d}_{k_0} \in \mathbb{C}^{M_e \times 1}$, we have

$$\mathbf{d}_{k_0} = \mathbf{\Phi}_{k_0} \mathbf{c}_{k_0} + \boldsymbol{\xi}_{k_0}, \tag{3.10}$$

where $\mathbf{c}_{k_0} \in \mathbb{C}^{L \times 1}$ and $\boldsymbol{\xi}_{k_0} \in \mathbb{C}^{M_e \times 1}$ represent the unknown coefficients for k_0 and the noise vector, respectively. Based on the linear measurement model in Eq. (3.10), we can derive the following FIM (by treating the real and imaginary parts of $\mathbf{c}_{k_0}$ separately)

$$\mathbf{I}_{k_0} = \frac{1}{\sigma^2} \begin{bmatrix} Re\{\mathbf{\Phi}_{k_0}^H \mathbf{\Phi}_{k_0}\} & -Im\{\mathbf{\Phi}_{k_0}^H \mathbf{\Phi}_{k_0}\} \\ Im\{\mathbf{\Phi}_{k_0}^H \mathbf{\Phi}_{k_0}\} & Re\{\mathbf{\Phi}_{k_0}^H \mathbf{\Phi}_{k_0}\} \end{bmatrix}, \tag{3.11}$$

where σ^2 is the noise variance,[4] $Re\{\cdot\}$ and $Im\{\cdot\}$ are the operations of taking the real part and the imaginary part, respectively. More details on CRB derivation can be found in the Background chapter. Based on the property of CRB, the total variance of any unbiased estimator of $\mathbf{c}_{k_0}$, denoted as $\hat{\mathbf{c}}_{k_0}$, is bounded as

$$\mathrm{Var}_{\hat{\mathbf{c}}_{k_0}} \geq \mathrm{Tr}\{\mathbf{I}_{k_0}^{-1}\}. \tag{3.12}$$

Therefore, calculating $\mathrm{Tr}\{\mathbf{I}_{k_0}^{-1}\}$ with different choices of M_e will provide important insights into the performance of spatial coefficient estimation w.r.t. M_e.

Figure 3.4 shows the change of $\mathrm{Tr}\{\mathbf{I}_{k_0}^{-1}\}$ w.r.t. the ratio between M_e and the model order L for a simulated data set with $\sigma = 1$. The detail on simulations is described in the next section. As can be seen, the theoretical minimum for M_e (i.e., $M_e/L = 1$ for making the problems in Eqs. (3.5) and (3.10) well-posed) gives rise to significantly greater CRB (about a factor of 100) compared to the cases where $M_e/L > 1$ (see the sharp transition between $M_e/L = 1$ and $M_e/L = 2$). Meanwhile, the CRB decreases as M_e increases, as expected, but it becomes stable when M_e reaches a certain threshold (e.g., $M_e/L \geq 6$). This result provides critical guidance in designing the sampling of $\mathcal{D}_2$, especially for making the tradeoff between the imaging time and the reconstruction performance. Moreover, the ill-conditioning problem (e.g., significantly amplified variances when M_e is small) also well

[4] Here we assume that the real and imaginary parts of $\boldsymbol{\xi}$ are both white Gaussian noise with variance σ^2.

motivates the incorporation of prior information through regularization, which is to be discussed in detail in Chapter 5.

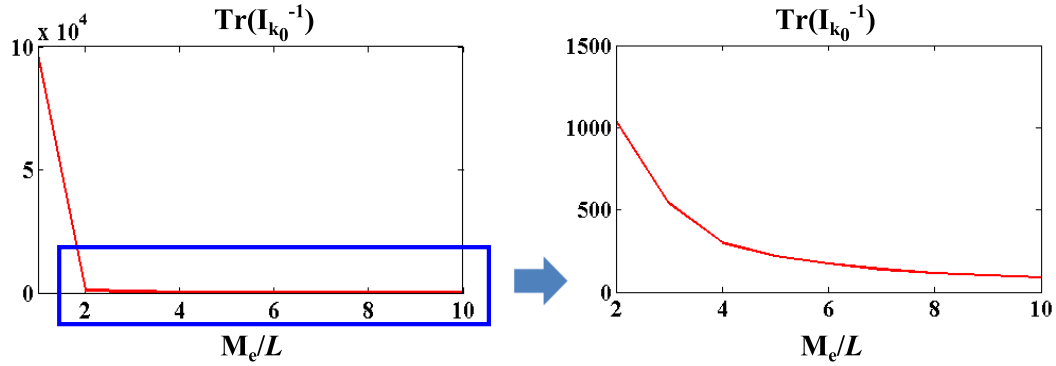

Figure 3.4: Plots of CRB against different values of M_e/L for $\hat{\mathbf{c}}_{k_0}$ ($\mathrm{Tr}\{\mathbf{I}_{k_0}^{-1}\}$). Note that the plot on the right is a zoomed-in version of the plot on the left, obtained by throwing away the point where $M_e = L$.

3.4.2 Spatiospectral Encoding Design for $\mathcal{D}_2$

As mentioned in Section 3.2, SPICE offers a range of flexibility for spatiospectral encoding, especially for acquiring $\mathcal{D}_2$, thus offering additional degrees-of-freedom in optimizing the sampling design. For example, different choices of spatiospectral sampling pattern and/or the temporal interval (denoted as τ, also referred to as the echo shift time) between different echo shifts can lead to rather different spatial coefficient estimation performance. Here, we compare three representative spatiospectral encoding patterns for $\mathcal{D}_2$ and analyze the effects of τ on the estimation of $\mathbf{C}$ with fixed M_e and L, again through a CRB calculation. But in this case, we are considering the joint FIM for the entire $\mathbf{C}$ to take into account the B_0 field inhomogeneity and k-space dependent estimation variances, which is important when comparing different sampling trajectories. Specifically, we derive that the model in Eq. (3.5) can be rewritten as

$$\begin{aligned} \mathbf{s}_2 &= \tilde{\boldsymbol{\Omega}}\tilde{\mathbf{F}}\tilde{\mathbf{B}}\tilde{\boldsymbol{\Phi}}vec\{\mathbf{C}\} + \boldsymbol{\xi} \\ &= \mathbf{A}vec\{\mathbf{C}\} + \boldsymbol{\xi}. \end{aligned} \tag{3.13}$$

$vec\{\mathbf{C}\}$ denotes a vectorization of $\mathbf{C}$. $\tilde{\mathbf{\Phi}}$ is an $NQ \times NL$ matrix generated from $\mathbf{\Phi}$ with the form of

$$\tilde{\mathbf{\Phi}} = \begin{bmatrix} \tilde{\mathbf{\Phi}}_1 \\ \tilde{\mathbf{\Phi}}_2 \\ \vdots \\ \tilde{\mathbf{\Phi}}_Q \end{bmatrix},$$

where the qth block $\tilde{\mathbf{\Phi}}_q$ $(q = 1, 2, \cdots, Q)$ has a size of $N \times NL$ and can be expressed as

$$\tilde{\mathbf{\Phi}}_q = [\mathbf{\Phi}_{1q}, \mathbf{\Phi}_{2q}, \cdots, \mathbf{\Phi}_{Lq}] \otimes \mathbf{I}_{N\times N},$$

where $\otimes$ denotes the Kronecker product and $\mathbf{I}_{N\times N}$ an $N \times N$ identity matrix. $\tilde{\mathbf{B}}$ is a sparse $NQ \times NQ$ diagonal matrix with the phase terms for field inhomogeneity modeling on its diagonal as follows:

$$\begin{bmatrix} \tilde{\mathbf{B}}_1 & & & \\ & \tilde{\mathbf{B}}_2 & & \\ & & \ddots & \\ & & & \tilde{\mathbf{B}}_Q \end{bmatrix}$$

where $\tilde{\mathbf{B}}_q$ has the form of

$$\tilde{\mathbf{B}}_q = \begin{bmatrix} e^{-i\gamma\Delta B(\mathbf{r}_1)t_q} & 0 & \cdots & 0 \\ 0 & e^{-i\gamma\Delta B(\mathbf{r}_2)t_q} & \cdots & 0 \\ \vdots & \vdots & \ddots & \vdots \\ 0 & 0 & \cdots & e^{-i\gamma\Delta B(\mathbf{r}_N)t_q} \end{bmatrix}.$$

$\tilde{\mathbf{F}}$ is an $NQ \times NQ$ block diagonal matrix each nonzero block of which is an $N \times N$ Fourier transform matrix, and $\tilde{\mathbf{\Omega}}$ is the sampling matrix.

With the model in Eq. (3.13), the joint FIM for $\mathbf{C}$ can be derived as

$$\mathbf{I}_{\mathbf{C}} = \frac{1}{\sigma^2}\begin{bmatrix} Re\{\mathbf{A}^H\mathbf{A}\} & -Im\{\mathbf{A}^H\mathbf{A}\} \\ Im\{\mathbf{A}^H\mathbf{A}\} & Re\{\mathbf{A}^H\mathbf{A}\} \end{bmatrix}. \tag{3.14}$$

Since some of the matrices in constructing $\mathbf{A}$ (e.g., $\mathbf{F}$) are too large to store explicitly in memory, we construct $\mathbf{A}^H\mathbf{A}$ column by column through operating it on unit vectors with 1 as one of the elements and 0 otherwise. Once $\mathbf{I}_{\mathbf{C}}$ is constructed, we can compute the CRB for any unbiased estimator of $\mathbf{C}$, $\hat{\mathbf{C}}$, as

$$\mathrm{COV}_{\hat{\mathbf{C}}} \geq \mathbf{I}_{\mathbf{C}}^{-1}, \tag{3.15}$$

where $\mathrm{COV}_{\hat{\mathbf{C}}}$ denotes the covariance matrix for $\hat{\mathbf{C}}$ and the diagonal elements in $\mathbf{I}_{\mathbf{C}}^{-1}$ are the lower bounds for the variances of each element in $\hat{\mathbf{C}}$.

Figure 3.5 illustrates three alternative (k,t)-space trajectories that can be used to generate $\mathcal{D}_2$. Note that the trajectory of each echo shift in Fig. 3.5c is similar to the one in Fig. 3.5b but with randomly chosen τ for each excitation. Figure 3.6 compares the lower bounds on the total variance (i.e., $\mathrm{Tr}\left\{\mathbf{I}_{\mathbf{C}}^{-1}\right\}$) for the above described three sampling designs with different echo shift times (i.e., $\tau = 1,2,3,4,5$). As can be seen, the center-out sampling pattern in Fig. 3.5b results in similar variance performance to the one with random echo shifts (Fig. 3.5c); both are significantly better than the sampling pattern in Fig. 3.5a for which each echo shift starts from the corner of k-space (similar to the conventional EPI imaging trajectories [52]). Moreover, for the center-out pattern, a $\tau = 3$ yields the best CRB. Either decreasing or increasing τ leads to increased estimation variance. This analysis result offers important insights for designing acquisition methods in practical MRSI experiments.

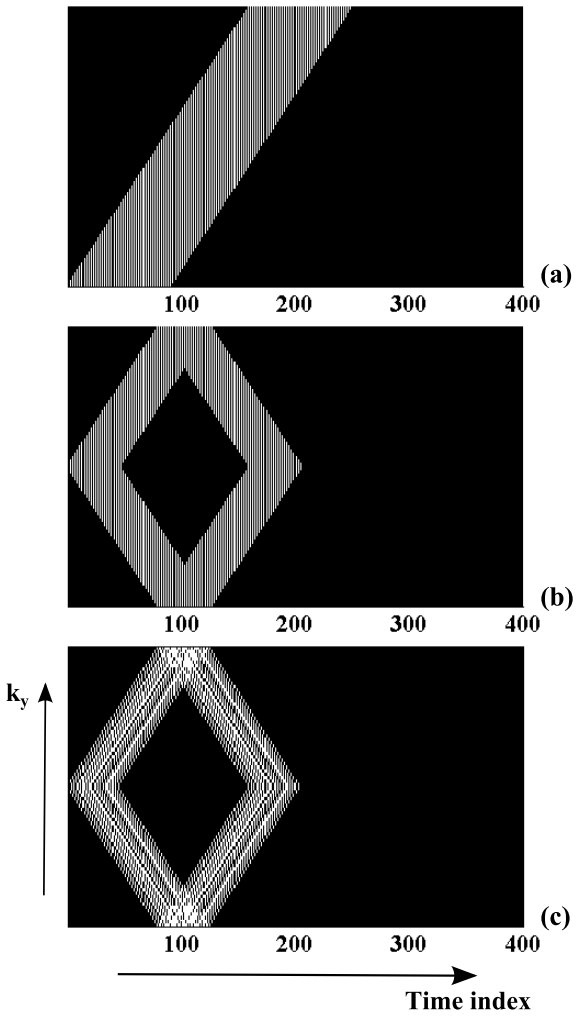

Figure 3.5: Three alternative (k,t)-space trajectories that can be used to generate $\mathcal{D}_2$. The vertical axis denotes k_y (with $k_y = 0$ at the center) and the horizontal axis the time index. The k_x axis is perpendicular to the paper. For the trajectories in (a), each echo shift (in each excitation) starts from the corner of k-space, while for the trajectories in (b), each echo shift starts from the center of k-space leading to a center-out pattern that produces more central k-space measurements in the early portion of the FID period. The trajectories in (c) are similar to those in (b) but with randomly spaced echo shifts (with τ chosen from $\{\tau | \tau = 1, 2, \cdots, 5\}$).

3.5 Simulations

We have evaluated the SPICE framework using results obtained from computer simulations, which are shown in this section.

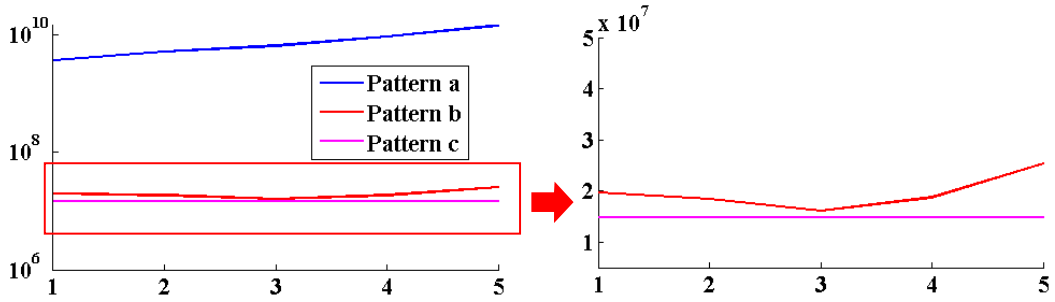

Figure 3.6: Lower bounds on the total variance (i.e., Tr $\left\{\mathbf{I}_{\mathbf{C}}^{-1}\right\}$ from the joint CRB calculation) against different amounts of echo shift (τ) for the three different sampling patterns shown in Fig. 3.5. The image on the right is a zoomed-in version (for the area identified by the red box) of the image on the left which is plotted in logarithmic scale due to the large range of Tr $\left\{\mathbf{I}_{\mathbf{C}}^{-1}\right\}$. An $M_e = 48$, an $L = 6$ and the field inhomogeneity map described for the numerical phantom generation were used to calculate the CRB.

3.5.1 Numerical Phantom Generation

A high-resolution spatiospectral distribution was numerically simulated as described in [49]. First, the spectra for six commonly observed ^{1}H metabolites, including NAA, creatine (Cr), choline (Cho), glutamate (Glu), glutamine (Gln), and myo-inositol (mI), were obtained from quantum mechanical simulation of a spin-echo pulse sequence with TE=30 ms [110]. Second, the composite spectra were then assigned to three segmented brain regions (gray matter, white matter and CSF) with different metabolite concentration ratios (based on literature values [49]). Third, realistic lineshape variations and baseline signals were incorporated into the spectra at each voxel. The resulting FID signal can then be represented by the following model:

$$\rho(\mathbf{r},t) = \sum_{m=1}^{M}\sum_{p_m=1}^{P_m} a_{m,p_m}(\mathbf{r}) e^{-i2\pi f_{m,p_m} t} e^{-t/T_{2,m}(\mathbf{r})} e^{-t/T_2'(\mathbf{r})} + \rho_b(\mathbf{r},t), \tag{3.16}$$

where M is the number of metabolites, P_m is the number of frequency components for the mth metabolite, $\{a_{m,p_m}\}$ control the relative strengths of different components, $\{f_{m,p_m}\}$ and $\{T_{2,m}\}$ are the resonance frequencies and relaxation constants, and $T_2'(\mathbf{r})$ captures the spatially dependent lineshape variations due to field inhomogeneity. $\rho_b(\mathbf{r},t)$ contains simulated baseline signals following a spline model in the frequency domain. The final simulated spatiotemporal distribution has a matrix size of 128×128 and 512 time points sampled at a bandwidth of 2000 Hz.

We then generated (k,t)-space measurements from this phantom with and without field inhomogeneity effects introduced through a coregistered experimentally acquired in vivo ΔB_0 map according to Eq. (2.13) (but without the nuisance components). A simulated full data set without the field inhomogeneity effects and noise contamination was used as the gold standard for comparison. First of all, we studied the dependence of subspace recovery on the number of spatial encodings in $\mathcal{D}_1$, in a noiseless case and a noisy case (with and without field inhomogeneity). To evaluate the accuracy of subspace estimation, the following normalized projection error is defined:

$$\mathrm{err}_p = \frac{\left\| \boldsymbol{\rho}_0 - \boldsymbol{\rho}_0 \hat{\boldsymbol{\Phi}}^H \left(\hat{\boldsymbol{\Phi}} \hat{\boldsymbol{\Phi}}^H \right)^{-1} \hat{\boldsymbol{\Phi}} \right\|_F}{\|\boldsymbol{\rho}_0\|_F}, \tag{3.17}$$

where $\boldsymbol{\rho}_0$ is the Casorati matrix formed by a gold standard data that is generated by a rank-8 truncation of the original high-resolution data (with truncation error less than 0.1 percent) and $\hat{\boldsymbol{\Phi}}$ is the temporal basis (with $L = 8$) estimated from $\mathcal{D}_1$ with various numbers of spatial encodings. Conceptually, this error metric evaluates how accurately the estimated temporal basis can represent the gold standard data and thus is an informative indicator for subspace estimation accuracy.

Secondly, we studied the dependence of spatial coefficient estimation accuracy on the number of spectral encodings for each k-space point in $\mathcal{D}_2$ (i.e., M_e). Accordingly, we simulated the trajectories shown in Fig. 3.1b and Fig. 3.5b to generate $\mathcal{D}_2$ with different numbers of echo shifts. Noise was added mimicking the SNR level of typical EPSI acquisitions (taking into account the higher bandwidth used). Spatial coefficients were then estimated from these noisy data using the true temporal basis estimated from the rank-8 gold standard. We evaluate the accuracy of estimated spatial coefficients using the relative ℓ_2 error defined as

$$\mathrm{RE}_{\mathbf{C}} = \frac{\left\| \hat{\mathbf{C}} - \mathbf{C}_0 \right\|_2}{\|\mathbf{C}_0\|_2} \tag{3.18}$$

where $\mathbf{C}_0$ contains the gold standard coefficients and $\hat{\mathbf{C}}$ its estimate.

Thirdly, we compare the performance of SPICE to two alternative acceleration methods commonly used in current MRSI studies: (i) low-resolution CSI and (ii) EPSI [24]. The effect of field inhomogeneity was included for all three schemes, which were set up to have the same acquisition time. Additional noise was added into the simulated EPSI data to account for the SNR difference due to different readout bandwidths. The field inhomogeneity corrected conjugate phase (CP) algorithm [107, 108] was used to obtain the CSI and EPSI reconstructions, which are compared with the corresponding SPICE reconstruction.

3.5.2 Results

Figure 3.7 shows the subspace estimation accuracy (err_p) when different numbers of spatial encodings (N_1) are included in $\mathcal{D}_1$, both with and without noise corruption but without B_0 field inhomogeneity. The subspace is estimated by directly applying SVD to the Casorati matrices formed from the data in $\mathcal{D}_1$ and choosing the L ($L = 8$) dominant right singular vectors. As shown by the results, in the noiseless case, as long as N_1 is greater than L, the projection error (err_p) becomes negligible, which implies that the data acquired have spanned the entire subspace (i.e., the condition in Eq. (3.9) is met). This is expected considering that for MRSI acquisitions $\mathcal{D}_1$ will typically include spatial encodings along all dimensions in k-space, avoiding the null space problem in dynamic imaging using PS model (if the navigator is not carefully designed [73]). In the case where data are contaminated by noise, err_p decreases as N_1 increases, but the difference also diminishes. Furthermore, it can be seen that an $N_1 \geq 50$ provides a reasonable cutoff for accurate subspace estimation in the presence of noise (in the absence of field inhomogeneity). However, as demonstrated by Fig. 3.8, as soon as field inhomogeneity effect is introduced into the data, the resulting spatiotemporal coupling prevents us from accurately recovering the subspace structure, even in the absence of noise, which implies the critical importance of field inhomogeneity correction. As shown by the image on the right of Fig. 3.8, which plots err_p against N_1 for the cases where only noise was added and both field inhomogeneity and noise were included, while increasing N_1 can significantly reduce the noise effects, it will not necessarily lead to more accurate subspace estimation unless the field inhomogeneity effect is removed. Nevertheless, the SVD-based

subspace estimation scheme using the central k-space data is reasonably robust to small field inhomogeneity, as illustrated in Fig. 3.9. Particularly, the difference in projection errors between the case where both small field inhomogeneity and noise are present and the case with noise only becomes negligible as N_1 increases, implying that the correction scheme used does not have to completely remove the field inhomogeneity effects for an accurate subspace estimation. In Chapter 5, details about the proposed field inhomogeneity correction methods will be provided with results demonstrating that the proposed methods are able to remove the field inhomogeneity effectively with only limited k-space data in $\mathcal{D}_1$.

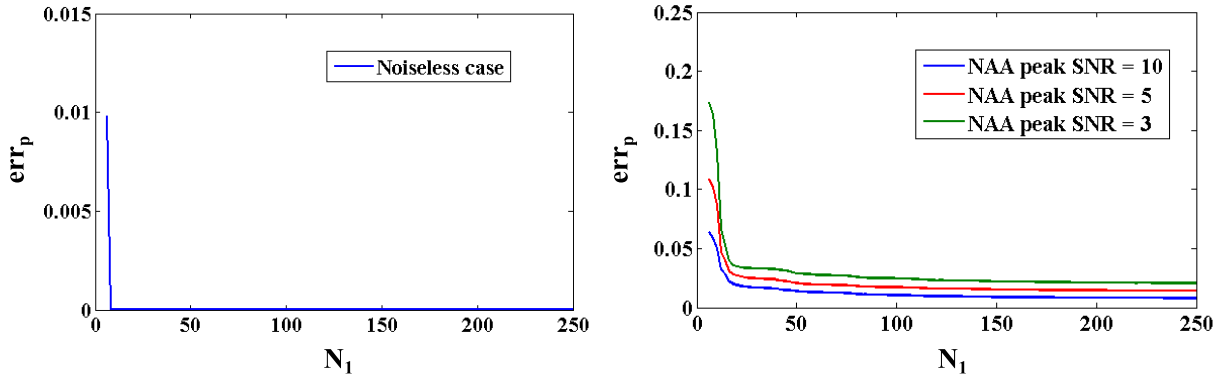

Figure 3.7: The normalized projection errors (err_p) for the estimated subspaces from $\mathcal{D}_1$ with different N_1: (a) results from using noiseless $\mathcal{D}_1$ and (b) results from using $\mathcal{D}_1$ contaminated by noise of different levels.

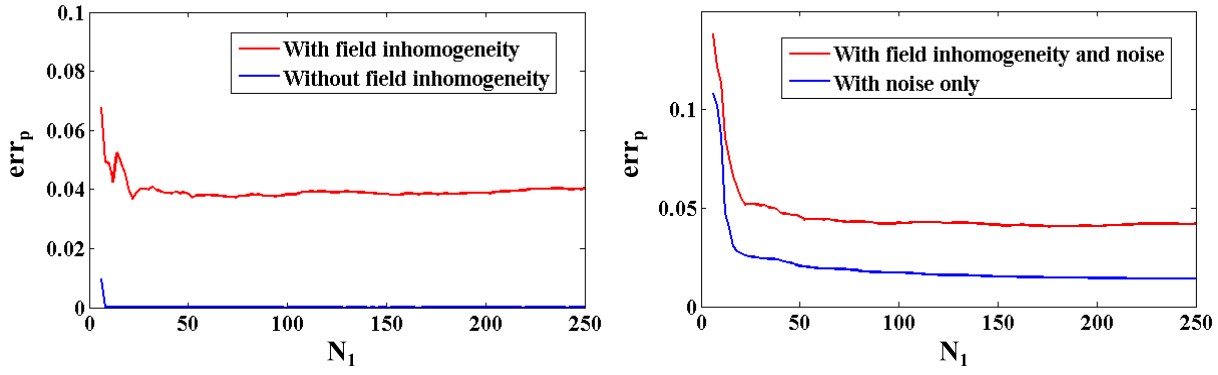

Figure 3.8: The normalized projection errors (err_p) for the estimated subspaces from $\mathcal{D}_1$ with different N_1: (a) results from using noiseless but B_0 field inhomogeneity corrupted $\mathcal{D}_1$ and (b) results from using $\mathcal{D}_1$ corrupted by both noise (with an NAA peak SNR of 5) and field inhomogeneity.

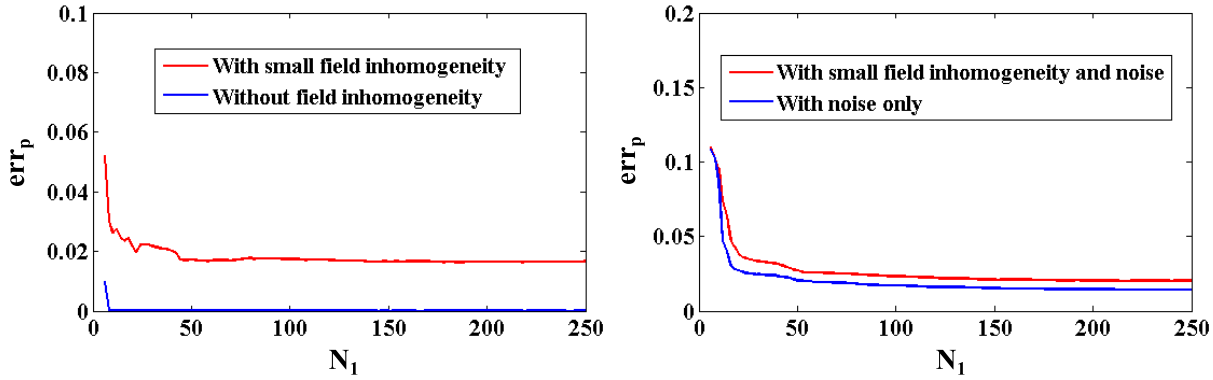

Figure 3.9: The normalized projection errors (err_p) for the estimated subspaces w.r.t. different N_1 in the presence of small field inhomogeneity (generated by scaling the B_0 map used for simulation by a factor of three): (a) noiseless $\mathcal{D}_1$ and (b) noisy $\mathcal{D}_1$ (with an NAA peak SNR of 5).

Figure 3.10 plots the changes in the relative ℓ_2 error for the spatial coefficient estimate $\hat{\mathbf{C}}$ against M_e/L. Two cases are compared here, one without any regularization ($\lambda = 0$) and the other with the regularization functional in Eq. (3.7). As shown by the plots, the trend in $\text{RE}_{\mathbf{C}}$ correlates very well with that from the theoretical analysis (in Fig. 3.4). Moreover, the differences between the two cases clearly demonstrate the importance of regularization in improving spatial coefficient estimation accuracy. Table 3.1 compares relative ℓ_2 errors ($\text{RE}_{\mathbf{C}}$) for spatial coefficients obtained from $\mathcal{D}_2$ generated by different sampling patterns. As can be seen, the estimation error comparison matches the theoretical analysis. The center-out pattern leads to significantly better reconstruction accuracy than the corner-up pattern (Fig. 3.5a). In addition, the pattern with random echo shifts results in slight improvement in the spatial coefficient estimation but the difference is not significant.

Figure 3.11 shows one set of representative simulation result from a SPICE acquisition with comparison to a CSI and an EPSI acquisitions. The SPICE reconstruction was obtained with $\mathcal{D}_1$ containing 8×8 CSI encodings each with 512 FID samples, $\mathcal{D}_2$ containing 48 echo shifts each with 128×128 spatial encodings (averaged four times) and $L = 8$. The total number of excitations is 256. Thus, the equivalent-time CSI acquisition had 16×16 spatial encodings while the EPSI acquisition had 128×128 spatial encodings (averaged twice) both with 512 FID samples. As can be seen, the CSI reconstruction shows significant blurring and ringing artifacts, which were reduced in the EPSI reconstruction but at the expense of a

significant loss of SNR, as expected. The SPICE reconstruction shows very good resolution with minimal loss in SNR compared to CSI and significantly better SNR compared to EPSI.

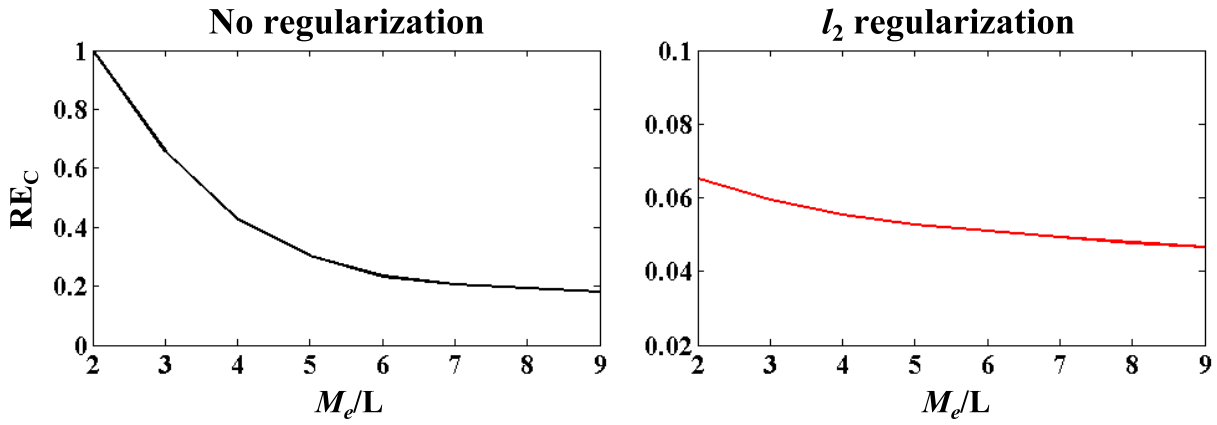

Figure 3.10: Changes of the relative error, $\text{RE}_{\mathbf{C}}$, for estimating $\mathbf{C}$ w.r.t. different values of M_e/L. The image on the left plots the errors for the case without regularization, while the image on the right plots the errors for the case with an ℓ_2 regularization.

Table 3.1: The relative ℓ_2 errors ($\text{RE}_{\mathbf{C}}$) for spatial coefficients obtained from $\mathcal{D}_2$ generated by different sampling patterns. Note that we fixed $M_e = 48$ and $\tau = 2$ for all three patterns and the same regularization parameter was used for reconstruction.

	Pattern in Fig. 3.5a	Pattern in Fig. 3.5b	Pattern in Fig. 3.5c
$\text{RE}_{\mathbf{C}}$	0.369	0.161	0.159

3.6 Summary

We have presented a new subspace imaging framework called SPICE for accelerated high-resolution MR spectroscopic imaging. SPICE exploits a unique property known as the partial separability (PS) of spectroscopic signals. This property indicates that high-dimensional spectroscopic signals reside in a very low-dimensional subspace, and enables the design of novel data acquisition strategies to sparsely sample (k, t)-space in two complementary data sets (one with limited k-space coverage but full spectral encoding and the other with

extended k-space coverage but limited spectral encoding) and a low-rank model based reconstruction framework to obtain high-resolution spatiospectral distributions with good SNR from the sparse data. Theoretical analysis and simulation studies have been performed to analyze the properties of SPICE and evaluate its potential for achieving fast, high-resolution spectroscopic imaging with high SNR.

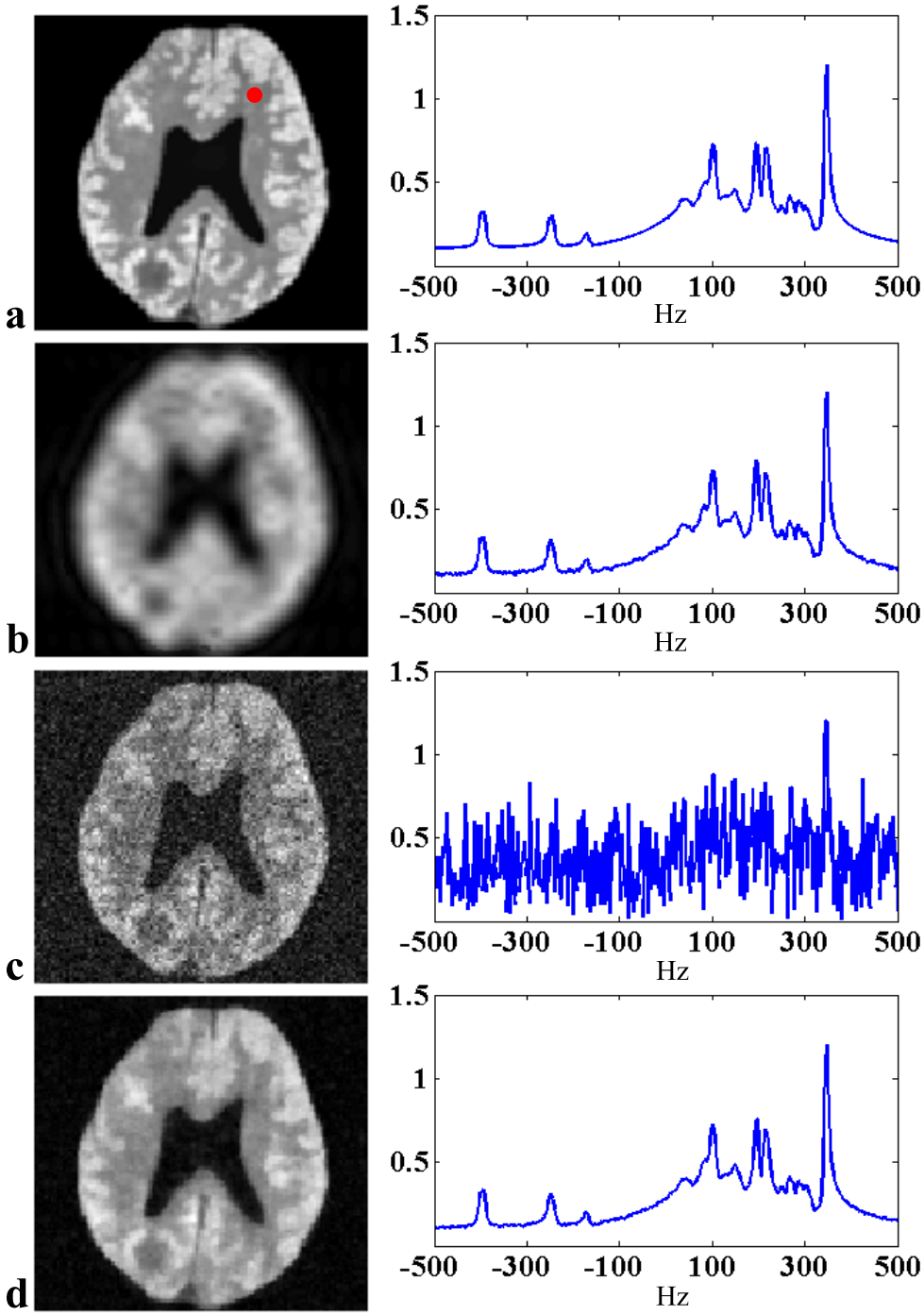

Figure 3.11: Simulation results: (a) the gold standard, (b) CSI reconstruction from 16×16 spatial encodings, (c) EPSI reconstruction from 128×128 spatial encodings averaged twice, and (d) SPICE reconstruction from 8×8 CSI encodings in $\mathcal{D}_1$, 48 echo-shifts in $\mathcal{D}_2$ averaged four times and $L = 8$. The left column shows the spatial distributions of a frequency component at 345 Hz and the right column shows the spectra corresponding to the voxel identified by the red dot for each case.

CHAPTER 4

DATA ACQUISITION FOR HIGH-RESOLUTION ^{1}H-MRSI USING SPICE

In this chapter, we present novel data acquisition methods that implement the SPICE hybrid sparse sampling strategy for accelerated spatiospectral encoding for two-dimensional (2D) and three-dimensional (3D) high-resolution ^{1}H-MRSI of the brain using SPICE.

4.1 A Hybrid CSI/EPSI Sequence for 2D MRSI

According to the SPICE hybrid sparse sampling strategy, two complementary data sets need to be acquired. The first one, denoted as $\mathcal{D}_1$, needs to have dense temporal sampling for subspace estimation, while the second one, $\mathcal{D}_2$, is required to cover an extended k-space for high-resolution spatiotemporal/spatiospectral reconstruction. The main challenge for implementing this strategy for in vivo ^{1}H-MRSI lies in covering an extended (k, t)-space in a short acquisition time while still maintaining sufficient SNR. To address this challenge, we developed a hybrid CSI/EPSI sequence for rapid 2D spatial plus spectral encoding. The proposed sequence (Fig. 4.1) comprises a CSI component to acquire $\mathcal{D}_1$ and an EPSI component to acquire $\mathcal{D}_2$. The CSI encoding has high SNR efficiency [15] and uses the entire FID period for spectral encoding, and thus is an ideal option to obtain $\mathcal{D}_1$. The EPSI component simultaneously encodes one spatial dimension (e.g., x) and the spectral dimension during an FID and thus can achieve an extended k-space coverage (for $\mathcal{D}_2$) in a short time. Note that the proposed EPSI encoding can have highly flexible temporal sampling design, i.e., it does not have to satisfy the spectral Nyquist criterion, completely bypassing the tradeoff between the achievable spectral bandwidth (BW) and the extend of k-space coverage in the conventional EPSI sequences due to gradient limitations [24, 51]. Additionally, this allows

for using lower BWs to reduce sample noise and the gradient strength.[1] This unique feature is enabled by the subspace model and the temporal basis estimated from $\mathcal{D}_1$.

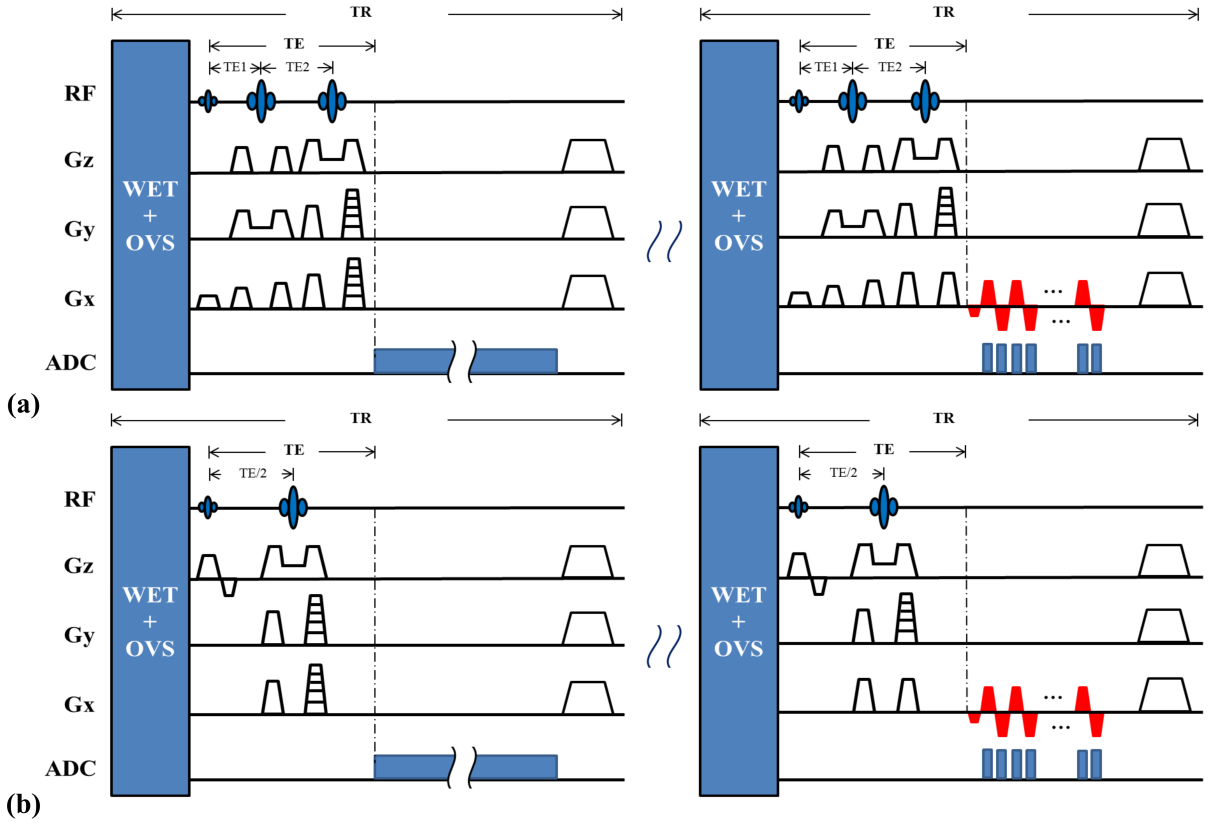

Figure 4.1: The proposed SPICE sequence for 2D ^{1}H-MRSI: (a) The CSI component (left) to acquire $\mathcal{D}_1$ and the EPSI-like component (right) to acquire $\mathcal{D}_2$, with PRESS excitation; (b) the same sequence but with spin-echo excitation. Note that for the EPSI encoding, the echoes acquired on the positive gradients are referred to as the odd echoes while those acquired on the negative gradients are referred to as the even echoes.

The corresponding (k, t)-space trajectories for the proposed hybrid CSI/EPSI sequence are shown in Fig. 4.2. As can be seen, only a limited portion of the central k-space is covered for $\mathcal{D}_1$ (due to SNR consideration) while $\mathcal{D}_2$ covers the entire k-space (for the desired spatial resolution) but with high speed and sparse temporal sampling. Therefore, the resulting trajectories represent a sparse sampling of the entire (k, t)-space and effectively combine the advantages of the slow CSI (i.e., high SNR and full spectral encoding) and the fast EPSI (i.e., speed and resolution).

[1]The ability to use lower gradient strengths also helps mitigate the eddy current effects and field drift (due to less gradient duties) [58].

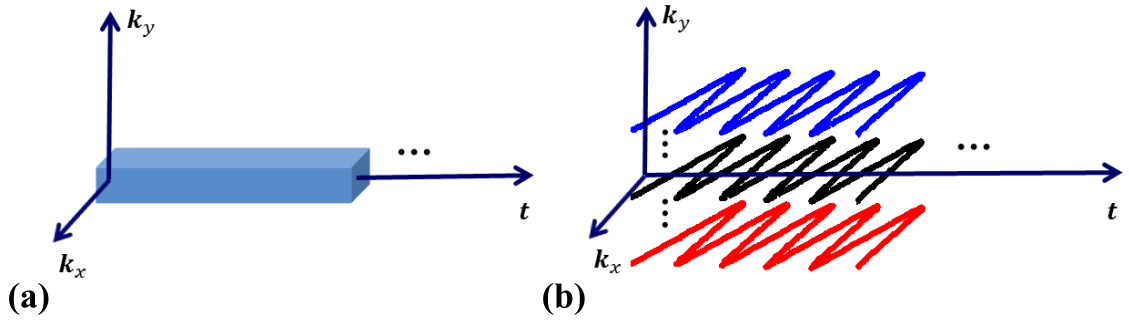

Figure 4.2: The sampling trajectories in (k,t)-space for $\mathcal{D}_1$ and $\mathcal{D}_2$ corresponding to the sequence in Fig. 4.1. As can be seen, only a limited portion of central k-space is covered in $\mathcal{D}_1$ while $\mathcal{D}_2$ covers the entire k-space for the desired spatial resolution. Note again that a key difference between the proposed encoding scheme and the conventional EPSI sequence in traversing (k_x,t) is that the proposed method is not constrained by the spectral Nyquist criterion.

Since ^{1}H-MRSI is considered in this thesis, the capability of WET water suppression [111] and outer volume suppression (OVS) are integrated into the proposed sequence for an initial water/fat suppression, while acquisitions without these suppression pulses can also be performed. Furthermore, the excitation module in the proposed sequence can use either the PRESS (Point Resolved Spectroscopy) [14] (Fig. 4.1a) or spin-echo (Fig. 4.1b) for excitation depending on whether a certain brain-only region needs to be localized.

4.2 A Dual-Density, Dual-Speed Sequence for 3D MRSI

While the proposed hybrid CSI/EPSI sequence can be readily extended to 3D by adding additional phase encodings along the third spatial dimension, it is too slow to provide the desired number of spatiospectral encodings for high-resolution 3D ^{1}H-MRSI. For example, acquiring a $\mathcal{D}_1$ with $10\times10\times10$ spatial encodings at TR=1000 ms would take more than 15 minutes of CSI. Furthermore, the EPSI component of the sequence in Fig. 4.1 requires a two-dimensional phase encoding scheme if extended to 3D, which would increase the acquisition time dramatically if high resolution is desired along all three spatial dimensions.

To address this problem, we propose a dual-density, dual-speed sequence to further accelerate the spatiospectral encoding for 3D MRSI using SPICE. The increased sensitivity in

3D encoding (due to larger excitation volumes) provides us with extra flexibility in making tradeoff between SNR and acquisition time. Accordingly, the proposed sequence (shown in Fig. 4.3) performs a hybrid of slow EPSI scans (to acquire $\mathcal{D}_1$) and rapid EPSI-like scans (to acquire $\mathcal{D}_2$). For the slow EPSI scans (Fig. 4.3, left column), we adopt the conventional EPSI acquisitions [24, 51] (with two spatial dimensions phase encoded and the echo spacing satisfying the spectral Nyquist), making the acquisition time for $\mathcal{D}_1$ equivalent to the CSI encoding in the 2D sequence. During the rapid EPSI scans (Fig. 4.3, right column), we simultaneously encode two spatial dimensions (e.g., x and y) to achieve the desired k-space coverage as well as the spectral dimension during each FID. The third spatial dimension (e.g., z) is phase encoded, and multiple echo shifts are used to obtain additional spectral encodings.

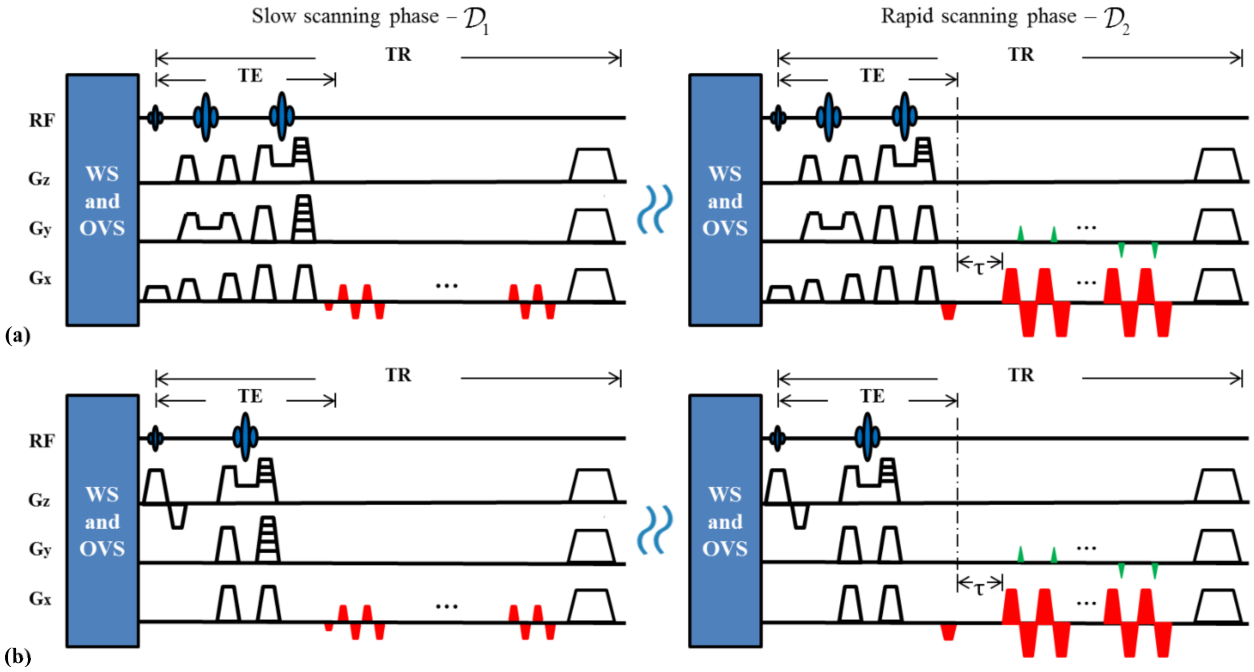

Figure 4.3: The proposed SPICE sequence for 3D ^{1}H-MRSI: (a) The slow EPSI scan (left) to acquire $\mathcal{D}_1$ and the rapid EPSI-like scan (right) to acquire $\mathcal{D}_2$, with PRESS excitation; (b) the same sequence but with spin-echo excitation. Note that the sampling bandwidth for the rapid EPSI scans is higher than that for the slow EPSI scans due to different resolution requirements for $\mathcal{D}_2$ and $\mathcal{D}_1$ and hence the stronger gradients used.

The resulting (k, t)-space trajectories for the proposed 3D sequence are shown in Fig. 4.4. As can be seen, we only cover a central portion of the k-space for $\mathcal{D}_1$ (thus it can be done

very quickly), and the entire (k_y, k_x) plane is traversed by each echo shift in $\mathcal{D}_2$. This special spatiospectral encoding scheme is again enabled by the subspace model and allows us to use the entire FID period to encode as much spatial information as possible, significantly shortening the time for obtaining the number of spatial encodings needed for high-resolution 3D MRSI. More specifically, compared to an EPSI scan with two-dimensional phase encoding (e.g., along k_y and k_z), the number of excitations needed for the proposed acquisition method changes from $N_{k_y} \times N_{k_z}$ to $N_{k_z} \times N_{es}$, where N_{k_y} and N_{k_z} denote the numbers of spatial encodings needed along k_y and k_z and N_{es} denotes the number of echo shifts. Given the low-dimensional subspace structure estimated from $\mathcal{D}_1$ (fully specifying the spectral dimension), only a limited N_{es} is needed for $\mathcal{D}_2$, i.e., $N_{es} < N_{k_y}$, which makes the reduction in data acquisition time possible.

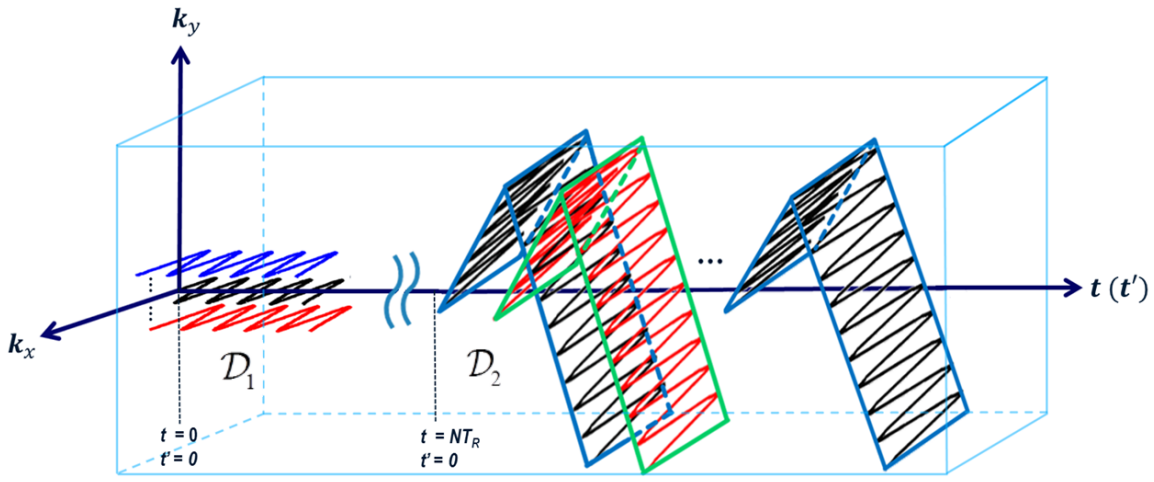

Figure 4.4: The sampling trajectories in (k, t)-space for $\mathcal{D}_1$ and $\mathcal{D}_2$ corresponding to the sequence in Fig. 4.3. The k_z axis is neglected here since the sampling trajectories are similar for each k_z. As illustrated in the figure, each echo train in $\mathcal{D}_2$ needs to be treated as "tilted" in the $k_y - t$ plane due to the chemical shift effect, and hence the overall sampling pattern is sparse in the entire (k, t)-space.

4.3 Implementation for Experimental Studies

4.3.1 Sampling Consideration

As discussed in Chapter 3, given a subspace with dimensionality L, the number of spatial encodings in $\mathcal{D}_1$ (i.e., N_1) theoretically has at least to be greater than L (Fig. 3.7). This is easy to satisfy since L is typically a small number with the field inhomogeneity effects removed [49, 50]. In practice, however, a sufficiently large N_1 is needed for effective field inhomogeneity correction and nuisance signal removal. Based on our experience in simulation and experimental studies, an N_1 greater than 12×12 for 2D and $12 \times 12 \times 12$ for 3D usually provides a good tradeoff between acquisition time and the performance of field inhomogeneity correction and nuisance signal removal [105, 108]. For the acquisition of $\mathcal{D}_2$, based on the theoretical analysis in Chapter 3 and empirical results from experimental studies, the number of echoes (or echo shifts) for $\mathcal{D}_2$ typically ranges from $4L$ to $6L$ in order to provide reasonable conditioning for the spatial coefficient fitting problem.

4.3.2 Auxiliary Data

Besides the spectroscopic data (i.e., $\mathcal{D}_1$ and $\mathcal{D}_2$), the overall imaging protocol for 2D ^{1}H-MRSI (on the brain) using SPICE will also include the following auxiliary data: (i) a 3D MPRAGE image for localizing the MRSI slice and extracting anatomical information for data processing (e.g., segmented water and fat images for nuisance signal removal [105] and edge structures for reconstruction [37]); (ii) a ΔB_0 map for field inhomogeneity modeling and correction, which is acquired using a double gradient-echo (GRE) sequence available on the scanner; (iii) a couple of additional anatomical images (with different T_1 and T_2 contrasts) for extracting better edge information [37]. For physical phantom experiments, a conventional GRE image is acquired as the reference image instead of the MPRAGE. Both the structural images and ΔB_0 map are coregistered to the spectroscopic data and have matched field of view (FOV) and volume of excitation (VOX).

For 3D acquisitions, the MRSI volume is localized using the 3D MPRAGE scan (similar to 2D). A multi-slice ΔB_0 map is acquired for 3D field inhomogeneity modeling and correction.

Both the MPRAGE and the field maps are again in co-registration with the spectroscopic data.

4.3.3 Echo Inconsistency Correction

For improved encoding efficiency, we have incorporated the capability of acquiring data on both polarities of the gradients into the EPSI encoding components of the proposed sequences. To make use of all the data, the inconsistency between echoes acquired on positive and negative gradients (referred to as odd and even echoes) needs to be corrected [32]. To this end, two navigator echo trains with reversed x-gradients (without phase encoding and water suppression) are acquired preceding the actual EPSI encoding. The sequence component that generates these navigators is shown in Fig. 4.5. Utilizing these data, we propose a scheme to correct the echo inconsistency. Specifically, the k-space center misalignments (Δk) are first estimated from each pair of positive and negative gradients (with the positive one from the first navigator echo train and the negative one from the reversed echo train), and the averaged Δk is then used to correct the misalignment between odd and even echoes in the actual EPSI encodings. Afterwards, a zeroth-order phase is estimated from the aligned echoes of the navigators and applied to the even echoes in the EPSI encodings. The advantages of using such navigators for echo correction are: First, since no water suppression is applied, the estimated correction parameters will have high fidelity due to the high SNR of the water signals; second, the phase difference estimated from the time-matched gradients from the navigators does not include chemical-shift-induced phase differences thus only reflects the effects of the gradients. This simple but efficient correction scheme significantly reduces the echo inconsistency in the data, as demonstrated by Fig. 4.6, which compares the magnitude of the FID signals from the k-space center before and after correction.

4.4 Summary

Special data acquisition methods are proposed to implement the SPICE hybrid sparse sampling strategy for 2D and 3D high-resolution ^{1}H-MRSI. For 2D MRSI using SPICE, a novel

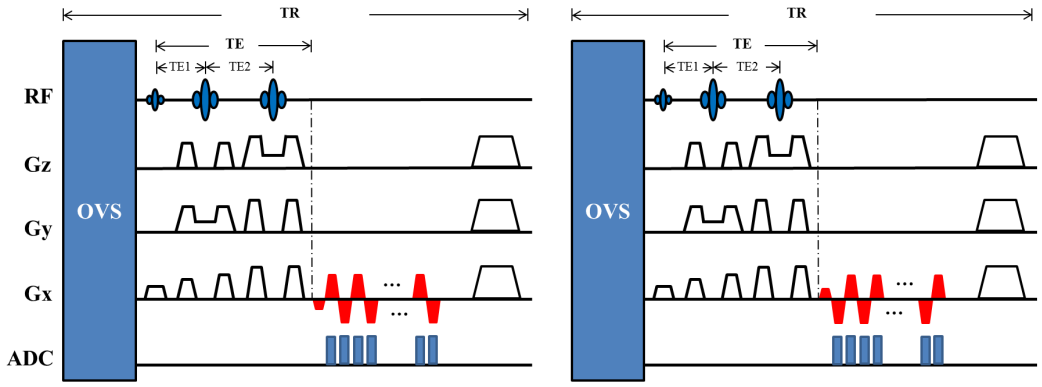

Figure 4.5: The proposed two navigator echo trains for echo inconsistency correction. The echo train in the left sequence diagram has reversed readout gradients compared to that on the right, and note that no phase encoding is applied (as opposed to the EPSI encodings in Fig. 4.1).

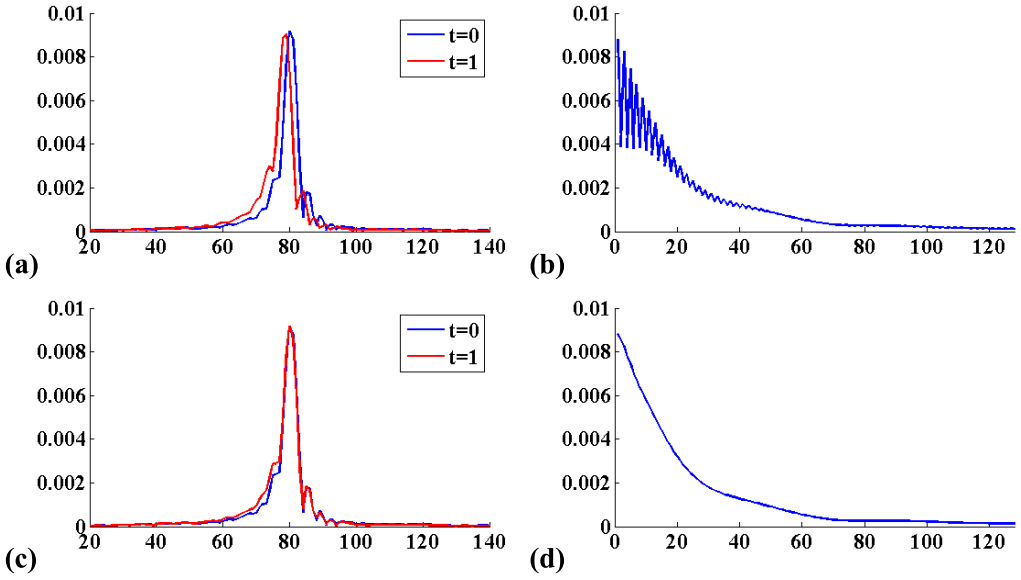

Figure 4.6: Comparison of the first and second echoes (corresponding to different gradient polarities) (a,c) and the magnitude of the signal evolutions from the k-space center (b,d). The figures on the first row (a-b) correspond to data before echo correction and those on the second row (c-d) correspond to data after echo correction. These results are generated from a phantom experiment.

hybrid CSI/EPSI sequence that enables rapid 2D spatial plus spectral encoding with an extended (k, t)-space coverage is presented. For 3D MRSI using SPICE, a dual-density dual-speed sequence that performs a hybrid of slow EPSI and rapid EPSI scans is proposed to further accelerate the data acquisition. These proposed hybrid sampling schemes, enabled

by the subspace model of SPICE, effectively combine the advantages of slow scans (i.e., high SNR and full spectral encoding) and rapid scans (i.e., high resolution) for accelerated high-resolution MRSI through sparse sampling.

CHAPTER 5

IMAGE RECONSTRUCTION FOR HIGH-RESOLUTION ^{1}H-MRSI USING SPICE

In this chapter, we present special image reconstruction methods for obtaining high-resolution spatiospectral/spatiotemporal functions of interest from the sparsely sampled data generated by the pulse sequences described in Chapter 4, in the context of high-resolution ^{1}H-MRSI using SPICE. The signal model, reconstruction formulations, and efficient numerical algorithms for solving the associated optimization problems will be discussed. A complete data processing pipeline for ^{1}H-MRSI data acquired from the brain using the SPICE sequences will be described.

5.1 Signal Model

To reconstruct the underlying spatiotemporal function (i.e., $\rho(\mathbf{r},t)$) from $\mathcal{D}_1$ (expressed as $\mathcal{D}_1 = \{s_{1,c}(\mathbf{k}_n, t_q)\}_{n,q,c=1}^{N_1,Q_1,C}$) and $\mathcal{D}_2$ (expressed as $\mathcal{D}_2 = \{s_{2,c}(\hat{\mathbf{k}}_n, \hat{t}_q)\}_{n,q,c=1}^{N_2,Q_2,C}$, $N_2 > N_1$ and $t_{Q_1} > t_{Q_2}$),[1] with c the coil index and C the number of coils used for acquisition, we model the measured (k,t)-space data for a ^{1}H-MRSI experiment as (by further generalizing Eq. (2.13))

$$s_c(\mathbf{k},t) = \int_V \left(\rho(\mathbf{r},t) + \rho_{ns}(\mathbf{r},t)\right) M_c(\mathbf{r})\, e^{-i\gamma\Delta B(\mathbf{r})t} e^{-i2\pi\mathbf{k}\mathbf{r}} d\mathbf{r} + \xi(\mathbf{k},t), \tag{5.1}$$

where V is the excited volume, γ the gyromagnetic ratio, $M_c(\mathbf{r})$ the sensitivity profile of the cth coil, $\Delta B(\mathbf{r})$ the B_0 field inhomogeneity map and $\xi(\mathbf{k},t)$ contains the measurement noise. $\rho_{ns}(\mathbf{r},t)$ represents the undesired nuisance signal components, i.e., the water and subcutaneous fat signals for ^{1}H-MRSI. Assuming the contribution of the nuisance signals can

[1] For detailed explanation on $\mathcal{D}_1$ and $\mathcal{D}_1$, refer to Chapters 3 and 4.

be effectively removed from the data (for detailed explanations on estimating and removing the nuisance water and fat signals from both $\mathcal{D}_1$ and $\mathcal{D}_2$ please refer to [105]), a discretized signal model can be obtained from Eq. (5.1) as (using the delta basis function for $\rho(\mathbf{r},t)$ and the box-car basis function for $\Delta B(\mathbf{r})$)

$$\mathbf{s}_c \;=\; \Omega\{\mathbf{FB}\odot\boldsymbol{\rho}_c\}+\boldsymbol{\xi}, \tag{5.2}$$

where $\mathbf{s}_c$ is a vector containing the data for the cth coil, Ω a (k,t)-space sampling operator, $\mathbf{F}$ a Fourier transform matrix, $\mathbf{B}$ a phase term modeling the field inhomogeneity effects as described in Eq. (5.1) (with $\mathbf{B}_{nq}=e^{-i\gamma\Delta B(\mathbf{r}_n)t_q}$), $\odot$ denotes entry-wise multiplication, $\boldsymbol{\rho}_c$ an $N_2\times Q_1$ matrix representation of $\rho\left(\mathbf{r},t\right)M_c\left(\mathbf{r}\right)$, and $\boldsymbol{\xi}$ the noise vector. Based on the PS model in Eq. (3.1), $\boldsymbol{\rho}_c$ has a low-rank representation as

$$\boldsymbol{\rho} \;=\; \mathbf{C}_c\boldsymbol{\Phi}, \tag{5.3}$$

where $\mathbf{C}_c\in\mathbb{C}^{N_2\times L}$ and $\boldsymbol{\Phi}\in\mathbb{C}^{L\times Q_1}$ are two rank-L matrices ($L<\min\left\{N_2,Q_1\right\}$). With this explicit low-rank model, we define the image reconstruction problem in SPICE as determining $\boldsymbol{\Phi}$ from the high SNR $\mathcal{D}_1$ and $\{\mathbf{C}_c\}_{c=1}^{C}$ from the high-resolution $\mathcal{D}_2$.

5.2 Subspace Estimation

According to Eqs. (5.2) and (5.3), in the absence of field inhomogeneity, estimating $\boldsymbol{\Phi}$ from $\mathcal{D}_1$ is straightforward, e.g., it can be done through an SVD on the Casorati matrix formed from the data [47,50]. In the presence of non-negligible field inhomogeneity, mostly the case for in vivo experiments, its effects need to be removed. The challenge to this problem lies in the limited data available in $\mathcal{D}_1$ [108], because the model in Eq. (5.2) is only accurate on high-resolution grids making the problem of reconstructing a field-inhomogeneity-free $\boldsymbol{\rho}_c$ ill-posed. To solve this problem, we perform the following regularized reconstruction from a coil-combined $\mathcal{D}_1$, denoted by a vector $\mathbf{s}_1\in\mathbb{C}^{N_1Q_1\times 1}$, to obtain a field inhomogeneity

corrected $\hat{\boldsymbol{\rho}}_1$[2]

$$\hat{\boldsymbol{\rho}}_1 \quad = \quad \arg\min_{\boldsymbol{\rho}} \|\mathbf{s}_1 - \Omega_T \{\mathbf{FB} \odot \boldsymbol{\rho}\}\|_2^2 + \lambda_f R(\boldsymbol{\rho}), \tag{5.4}$$

where $\hat{\boldsymbol{\rho}}_1$ has a size of $\hat{N}_1 \times Q_1$ (with $\hat{N}_1 > N_1$ to ensure accurate field inhomogeneity modeling [108]), Ω_T is a sampling operator (only sampling the central k-space as described for $\mathcal{D}_1$), and $\mathbf{F}$ and $\mathbf{B}$ the same as described in Eq. (5.2). $R(\boldsymbol{\rho})$ is a regularization term and λ_f is the regularization parameter. Different choices for $R(\boldsymbol{\rho})$ can be used, e.g., the weighted-ℓ_2 regularization shown in Chapter 3 or the nuclear-norm penalty $\|\boldsymbol{\rho}\|_*$ which is defined as the sum of the absolute value of the singular values of $\boldsymbol{\rho}$ [112]. The weighted-ℓ_2 penalty allows us to incorporate anatomical information into the reconstruction, while the low-rankness encouraging nuclear-norm penalty is well motivated by the low-dimensional subspace model for the underlying $\boldsymbol{\rho}$. After $\hat{\boldsymbol{\rho}}_1$ is obtained by solving the optimization problem in Eq. (5.4), it is rearranged into a Casorati matrix to which an SVD can be applied. The first L right singular vectors are then chosen to form the matrix $\boldsymbol{\Phi}$. The model order L is selected based on examining the singular value decay of the Casorati matrix. Afterwards, a spline-based interpolation is applied to the temporal basis functions (rows of $\boldsymbol{\Phi}$) to match the temporal sampling grids of the data in $\mathcal{D}_2$. The interpolated basis set is denoted as $\hat{\boldsymbol{\Phi}}$ and used for the spatial coefficient estimation, which is to be described next.

5.3 Spatial Coefficient Estimation

Integrating the estimated $\hat{\boldsymbol{\Phi}}$ and the low-rank model in Eq. (5.3) into the signal model in Eq. (5.2) leads to [47, 48, 113]

$$\mathbf{s}_{2,c} = \Omega_S\{\mathbf{FB} \odot \mathbf{C}_c\hat{\boldsymbol{\Phi}}\} + \boldsymbol{\xi}_2, \tag{5.5}$$

where $\mathbf{s}_{2,c} \in \mathbb{C}^{N_2Q_2 \times 1}$ denotes the vector containing data from $\mathcal{D}_2$ (for the cth coil), Ω_S the sparse sampling operator, and $\boldsymbol{\xi}_2$ the noise vector. Accordingly, $\mathbf{C}_c$ can be determined by

[2] See Section 5.5 for more details on coil combination and multi-coil processing.

solving the following regularized least-squares formulation

$$\hat{\mathbf{C}}_c \;=\; \arg\min_{\mathbf{C}_c} \left\| \mathbf{s}_{2,c} - \Omega_S\{\mathbf{FB} \odot \mathbf{C}_c\hat{\mathbf{\Phi}}\} \right\|_2^2 + \lambda_c \Psi\left(\mathbf{C}_c, \hat{\mathbf{\Phi}}\right), \tag{5.6}$$

where $\|\cdot\|_2^2$ measures the data consistency and $\Psi(\cdot)$ represents the regularization functional with regularization parameter λ_c. Many choices can be made for $\Psi(\cdot)$ to incorporate prior information about $\rho(\mathbf{r}, t)$ or $\tilde{\rho}(\mathbf{r}, f)$. Here we consider two alternative choices. The first one is the weighted-ℓ_2 regularization term as

$$\Psi\left(\mathbf{C}_c, \hat{\mathbf{\Phi}}\right) = \left\| \mathbf{WDC}_c\hat{\mathbf{\Phi}} \right\|_2^2, \tag{5.7}$$

and the other is the following total-variation based regularization term

$$\Psi\left(\mathbf{C}_c, \hat{\mathbf{\Phi}}\right) = \left\| \mathbf{WDC}_c\hat{\mathbf{\Phi}}\mathbf{\Psi} \right\|_1, \tag{5.8}$$

where $\mathbf{D}$ is a finite difference operator, $\mathbf{W}$ contains edge weights derived from high-resolution anatomical images [37] and $\mathbf{\Psi}$ denotes a temporal sparsifying transform (e.g., the Fourier transform for MRSI [45]).[3] The two regularization functionals have their own advantages. While the ℓ_2 penalty is advantageous in terms of computational efficiency and easier performance characterization, the ℓ_1 penalty (motivated by recent developments in sparse signal recovery) has demonstrated superior performance over quadratic penalties in various applications, including both sparse sampling and denoising. It is worth noting that similar forms of Eq. (5.8) can also be found in the context of dynamic imaging [72, 74, 81, 114] and super-resolution MRSI [41, 43].

[3] We define $\|\mathbf{A}\|_1$ for a $N_1 \times N_2$ matrix $\mathbf{A}$ as $\|\mathbf{A}\|_1 = \sum_{n_1,n_2=1}^{N_1,N_2} |A_{n_1,n_2}|$.

5.4 Numerical Algorithms

5.4.1 Field-Inhomogeneity Corrected Reconstruction

Solving the problem in Eq. (5.4) with ℓ_2 regularization is equivalent to solving a system of linear equations which can be done easily using the linear CG method. For the nuclear-norm regularized reconstruction, we propose to use a variable splitting and alternating direction method of multipliers (ADMM) based algorithm. Specifically, we rewrite the original problem into the following equivalent problem

$$\begin{aligned} \hat{\boldsymbol{\rho}}_1, \hat{\mathbf{U}} &= \arg\min_{\boldsymbol{\rho},\mathbf{U}} \|\mathbf{s}_1 - \Omega_T \{\mathbf{FB} \odot \boldsymbol{\rho}\}\|_2^2 + \lambda_f \|\mathbf{U}\|_* \\ &s.t. \quad \mathbf{U} = \boldsymbol{\rho}, \end{aligned} \tag{5.9}$$

where $\mathbf{U}$ is an auxiliary variable that separates the computations associated with $\boldsymbol{\rho}$ in the least-squares and nuclear-norm terms. Accordingly, we apply the ADMM algorithm that iteratively minimizes the following augmented Lagrangian function:

$$\mathcal{L}(\boldsymbol{\rho}, \mathbf{U}, \mathbf{Y}) = \|\mathbf{s}_1 - \Omega_T \{\mathbf{FB} \odot \boldsymbol{\rho}\}\|_2^2 + \lambda_f \|\mathbf{U}\|_* + \frac{\mu}{2} \|\mathbf{U} - \boldsymbol{\rho}\|_F^2 + \langle \mathbf{Y}, \mathbf{U} - \boldsymbol{\rho} \rangle \tag{5.10}$$

w.r.t. $\boldsymbol{\rho}$ and $\mathbf{U}$ and updates the Lagrangian multiplier $\mathbf{Y}$ to solve Eq. (5.9), where μ is a preselected penalty parameter and $\langle \mathbf{X}_1, \mathbf{X}_2 \rangle$ denotes the inner product between $\mathbf{X}_1$ and $\mathbf{X}_2$. To minimize the function in Eq. (5.10), two subproblems are solved in each iteration, i.e.:

1. For fixed $\mathbf{U}^{(i)}$, solve

$$\begin{aligned} \boldsymbol{\rho}^{(i+1)} &= \arg\min_{\boldsymbol{\rho}} \|\mathbf{s}_1 - \Omega_T \{\mathbf{FB} \odot \boldsymbol{\rho}\}\|_2^2 + \frac{\mu}{2} \|\mathbf{U}^{(i)} - \boldsymbol{\rho}\|_F^2 + \left\langle \mathbf{Y}, \mathbf{U}^{(i)} - \boldsymbol{\rho} \right\rangle \\ &= \arg\min_{\boldsymbol{\rho}} \|\mathbf{s}_1 - \Omega_T \{\mathbf{FB} \odot \boldsymbol{\rho}\}\|_2^2 + \frac{\mu}{2} \left\| \boldsymbol{\rho} - \mathbf{U}^{(i)} - \frac{\mathbf{Y}}{\mu} \right\|_F^2. \end{aligned} \tag{5.11}$$

2. For fixed $\boldsymbol{\rho}^{(i+1)}$, solve

$$\begin{aligned}\mathbf{U}^{(i+1)} &= \arg\min_{\mathbf{U}} \lambda_f \|\mathbf{U}\|_* + \frac{\mu}{2}\left\|\mathbf{U}-\boldsymbol{\rho}^{(i+1)}\right\|_F^2 + \left\langle \mathbf{Y}, \mathbf{U}-\boldsymbol{\rho}^{(i+1)}\right\rangle \\ &= \arg\min_{\mathbf{U}} \lambda_f \|\mathbf{U}\|_* + \frac{\mu}{2}\left\|\mathbf{U}-\boldsymbol{\rho}^{(i+1)}+\frac{\mathbf{Y}}{\mu}\right\|_F^2. \end{aligned} \tag{5.12}$$

Note that the original ADMM algorithm alternates between problems in Eqs. (5.11) and (5.12) until a certain convergence criterion is met and then updates $\mathbf{Y}$. The penalty parameter can also be updated for faster convergence. In order to further accelerate the algorithm, we use an iterative procedure that solves Eqs. (5.11) and (5.12) once followed by updating $\mathbf{Y}$ and μ in each iteration. A detailed description of the proposed algorithm is in Algorithm 1.

5.4.2 Spatial Coefficient Estimation

Integrating the regularization functional in Eq. (5.7) with Eq. (5.6) results in a regularized linear least-squares problem that can be easily solved by a linear CG method. However, the non-smooth convex optimization problem resulting from integrating the regularization term in Eq. (5.8) with Eq. (5.6) is more challenging. A number of efficient algorithms have been proposed to solve this type of problems (e.g., those in [116–119]). Based on the existing work, we propose here a variable splitting and ADMM based algorithm [118, 120] to solve the optimization problem associated with our spatial coefficient estimation formulation.

First of all, we reformulate the ℓ_1 regularization problem as[4]

$$\begin{aligned}\hat{\mathbf{C}}, \hat{\mathbf{S}} &= \arg\min_{\mathbf{C},\mathbf{S}} \left\|\mathbf{s}_2 - \Omega_S\{\mathbf{FB}\odot\mathbf{C}\hat{\boldsymbol{\Phi}}\}\right\|_2^2 + \lambda_c \|\mathbf{S}\|_1 \\ &s.t. \quad \mathbf{S} = \mathbf{D}_w\mathbf{C}\hat{\boldsymbol{\Phi}}\boldsymbol{\Psi}, \end{aligned} \tag{5.13}$$

with auxiliary variable $\mathbf{S}$ and $\mathbf{D}_w = \mathbf{WD}$. The corresponding augmented Lagrangian func-

[4]The coil index c is dropped for notational convenience when describing the detailed algorithm.

Algorithm 1 The algorithm for solving Eq. (5.9).

1. For fixed $\mathbf{Y}^{(i)}$ and $\mathbf{U}^{(i)}$, update $\boldsymbol{\rho}$ by solving Eq. (5.11), which is equivalent to solving the following system of linear equations

$$\mathcal{A}\{\boldsymbol{\rho}\} + \frac{\mu^{(i)}}{2}\boldsymbol{\rho} = \mathbf{B}^H \odot \mathbf{F}^H \Omega_T^H \{\mathbf{s}_1\} + \frac{\mu^{(i)}}{2}\left(\mathbf{U}^{(i)} + \frac{\mathbf{Y}^{(i)}}{\mu}\right)$$

   where $\mathcal{A}\{\boldsymbol{\rho}\} = \mathbf{B}^H \odot \mathbf{F}^H \Omega_T^H \{\Omega_T \{\mathbf{FB} \odot \boldsymbol{\rho}\}\}$. This can be done using the linear CG algorithm.

2. With updated $\boldsymbol{\rho}^{(i+1)}$ and $\mathbf{Y}^{(i)}$, update $\mathbf{U}$ by solving Eq. (5.12), which has a closed-form solution [115] as

$$\mathbf{U}^{(i+1)} = \mathbf{P}\ \mathrm{diag}\,(s_r)\ \mathbf{Q}$$

   where $s_r = \mathrm{sign}(\sigma_r)\max\left\{|\sigma_r| - \frac{\lambda_f}{\mu^{(i)}}, 0\right\}$ and $\boldsymbol{\rho}^{(i+1)} - \frac{\mathbf{Y}^{(i)}}{\mu^{(i)}} = \mathbf{P}\ \mathrm{diag}\,(\sigma_r)\ \mathbf{Q}$ with $\{\sigma_r\}$ being the singular values.

3. With fixed $\boldsymbol{\rho}^{(i+1)}$ and $\mathbf{U}^{(i+1)}$, update the Lagrange multiplier according to

$$\mathbf{Y}^{(i+1)} = \mathbf{Y}^{(i)} + \mu^{(i)}\left(\mathbf{U}^{(i+1)} - \boldsymbol{\rho}^{(i+1)}\right)$$

   and update the penalty parameter according to

$$\mu^{(i+1)} = \alpha\mu^{(i)}$$

   where $\alpha > 1$ is a predetermined coefficient.

4. Repeat steps 1-3 until the convergence criterion

$$\frac{\left\|\boldsymbol{\rho}^{(i+1)} - \boldsymbol{\rho}^{(i)}\right\|_2}{\left\|\boldsymbol{\rho}^{(i)}\right\|_2} < \epsilon, \qquad \text{for } \epsilon > 0$$

   is met, or until a maximum number of iterations is reached.

tion for Eq. (5.13) can then be written as

$$\begin{aligned}\mathcal{L}(\mathbf{C},\mathbf{S},\mathbf{Y},\mu) &= \left\|\mathbf{s}_2 - \Omega_S\{\mathbf{FB}\odot\mathbf{C}\hat{\mathbf{\Phi}}\}\right\|_2^2 + \lambda_c\left\|\mathbf{S}\right\|_1 + \\ &\frac{\mu}{2}\left\|\mathbf{S}-\mathbf{D}_w\mathbf{C}\hat{\mathbf{\Phi}}\mathbf{\Psi}\right\|_F^2 + \left\langle\mathbf{Y},\mathbf{S}-\mathbf{D}_w\mathbf{C}\hat{\mathbf{\Phi}}\mathbf{\Psi}\right\rangle,\end{aligned} \tag{5.14}$$

where $\mathbf{Y}$ is the Lagrangian multiplier and μ is the penalty parameter. The ADMM algorithm then alternatively performs the following steps:

1. For fixed $\mathbf{C}^{(i)}$ and $\mathbf{Y}^{(i)}$, solve the subproblem

$$\mathbf{S}^{(i+1)} = \arg\min_{\mathbf{S}}\mathcal{L}\left(\mathbf{C}^{(i)},\mathbf{S},\mathbf{Y}^{(i)},\mu\right). \tag{5.15}$$

2. For fixed $\mathbf{S}^{(i+1)}$ and $\mathbf{Y}^{(i)}$, solve the subproblem

$$\mathbf{C}^{(i+1)} = \arg\min_{\mathbf{C}}\mathcal{L}\left(\mathbf{C},\mathbf{S}^{(i+1)},\mathbf{Y}^{(i)},\mu\right). \tag{5.16}$$

3. Update the Lagrangian multiplier as

$$\mathbf{Y}^{(i+1)} = \mathbf{Y}^{(i)} + \mu\left(\mathbf{S}^{(i+1)} - \mathbf{D}_w\mathbf{C}^{(i+1)}\hat{\mathbf{\Phi}}\mathbf{\Psi}\right). \tag{5.17}$$

The overall algorithm is summarized in Algorithm 2. This type of ADMM algorithms has recently been shown very effective for various MR image reconstruction problems [84,119,121, 122] by achieving state-of-the-art tradeoff between computational efficiency and accuracy.

For 3D-SPICE, the increased problem size due to the additional third spatial dimension imposes additional computational challenges. To address this problem, we further develop a new variable splitting based algorithm to solve the resulting optimization problem with ℓ_1 regularization. Specifically, we introduce an additional auxiliary variable $\mathbf{P}$ and use the

Algorithm 2 The algorithm for solving Eq. (5.13).

1. For fixed $\mathbf{C}^{(i)}, \mathbf{Y}^{(i)}$, update $\mathbf{S}$ by solving

$$\begin{aligned}\mathbf{S}^{(i+1)} &= \arg\min_{\mathbf{S}} \lambda_c \|\mathbf{S}\|_1 + \frac{\mu}{2}\left\|\mathbf{S} - \mathbf{D}_w\mathbf{C}^{(i)}\hat{\mathbf{\Phi}}\mathbf{\Psi}\right\|_F^2 + \left\langle \mathbf{Y}^{(i)}, \mathbf{S} - \mathbf{D}_w\mathbf{C}^{(i)}\hat{\mathbf{\Phi}}\mathbf{\Psi}\right\rangle \\ &= \arg\min_{\mathbf{S}} \lambda_c \|\mathbf{S}\|_1 + \frac{\mu}{2}\left\|\mathbf{S} - \mathbf{D}_w\mathbf{C}^{(i)}\hat{\mathbf{\Phi}}\mathbf{\Psi} + \frac{\mathbf{Y}^{(i)}}{\mu}\right\|_F^2,\end{aligned}$$

   which can be done by an element-wise soft-thresholding operation [123].

2. For fixed $\mathbf{S}^{(i+1)}, \mathbf{Y}^{(i)}$, update $\mathbf{C}$ by solving

$$\begin{aligned}\mathbf{C}^{(i+1)} &= \arg\min_{\mathbf{C}} \left\|\mathbf{s}_2 - \Omega_S\{\mathbf{FB}\odot\mathbf{C}\hat{\mathbf{\Phi}}\}\right\|_2^2 + \frac{\mu}{2}\left\|\mathbf{S}^{(i+1)} - \mathbf{D}_w\mathbf{C}\hat{\mathbf{\Phi}}\mathbf{\Psi}\right\|_F^2 \\ &\quad + \left\langle \mathbf{Y}^{(i)}, \mathbf{S}^{(i+1)} - \mathbf{D}_w\mathbf{C}\hat{\mathbf{\Phi}}\mathbf{\Psi}\right\rangle \\ &= \arg\min_{\mathbf{C}} \left\|\mathbf{s}_2 - \Omega_S\{\mathbf{FB}\odot\mathbf{C}\hat{\mathbf{\Phi}}\}\right\|_2^2 + \frac{\mu}{2}\left\|\mathbf{D}_w\mathbf{C}\hat{\mathbf{\Phi}}\mathbf{\Psi} - \left(\mathbf{S}^{(i+1)} + \frac{\mathbf{Y}^{(i)}}{\mu}\right)\right\|_F^2,\end{aligned}$$

   which is equivalent to solving the following system of linear equations

$$\mathcal{A}\{\mathbf{C}\} + \frac{\mu}{2}\mathcal{B}\{\mathbf{C}\} = \left(\mathbf{B}^H \odot \left(\mathbf{F}^H{\Omega_S}^H\{\mathbf{s}_2\}\right)\right)\hat{\mathbf{\Phi}}^H + \frac{\mu}{2}\mathbf{D}_w^H\left(\mathbf{S}^{(i+1)} + \frac{\mathbf{Y}^{(i)}}{\mu}\right)\mathbf{\Psi}^H\hat{\mathbf{\Phi}}^H,$$

   where the linear operators $\mathcal{A}$ and $\mathcal{B}$ are defined as

$$\mathcal{A}\{\mathbf{C}\} = \left(\mathbf{B}^H \odot \mathbf{F}^H\Omega_S^H\{\Omega_S\{\mathbf{FB}\odot\mathbf{C}\hat{\mathbf{\Phi}}\}\}\right)\hat{\mathbf{\Phi}}^H \text{ and } \mathcal{B}\{\mathbf{C}\} = \mathbf{D}_w^H\mathbf{D}_w\mathbf{C}\hat{\mathbf{\Phi}}\mathbf{\Psi}\mathbf{\Psi}^H\hat{\mathbf{\Phi}}^H.$$

   The linear CG algorithm is used to solve this subproblem.

3. Update $\mathbf{Y}^{(i)}$ as

$$\mathbf{Y}^{(i+1)} = \mathbf{Y}^{(i)} + \mu\left(\mathbf{S}^{(i+1)} - \mathbf{D}_w\mathbf{C}^{(i+1)}\hat{\mathbf{\Phi}}\mathbf{\Psi}\right).$$

4. Repeat 1-4 until the relative change in $\mathbf{C}$ satisfies $\left\|\mathbf{C}^{(i+1)} - \mathbf{C}^{(i)}\right\|_2 / \left\|\mathbf{C}^{(i)}\right\|_2 < 10^{-4}$ or a maximum number of iterations is reached.

following variable splitting reformulation:

$$\begin{aligned}\hat{\mathbf{C}},\hat{\mathbf{P}},\hat{\mathbf{S}} &= \arg\min_{\mathbf{C},\mathbf{P},\mathbf{S}} \|\mathbf{s}_2 - \Omega_S\{\mathbf{FP}\}\|_2^2 + \lambda_c \|\mathbf{S}\|_1 \\ &s.t. \quad \mathbf{P} = \mathbf{B} \odot \mathbf{C}\hat{\mathbf{\Phi}} \\ &\quad\ \mathbf{S} = \mathbf{D}_w\mathbf{C}\hat{\mathbf{\Phi}}\mathbf{\Psi}. \end{aligned} \tag{5.18}$$

Note that by introducing $\mathbf{P}$, we separated the Fourier encoding operator and the field inhomogeneity operator, which significantly simplified the computations associated with both of them. An ADMM-based algorithm is then applied to solve the problem in Eq. (5.18). As will be shown in the detailed iterative procedure, the reformulation in Eq. (5.18) offers additional benefits in further accelerating the reconstruction process.

Similar to the case in Eq. (5.14), the corresponding augmented Lagrangian function for Eq. (5.18) can be written as

$$\begin{aligned} f(\mathbf{C},\mathbf{P},\mathbf{S},\mathbf{Y},\mathbf{Z}) &= \|\mathbf{s}_2 - \Omega_S\{\mathbf{FP}\}\|_2^2 + \lambda_c \|\mathbf{S}\|_1 + \frac{\mu_1}{2}\left\|\mathbf{P} - \mathbf{B}\odot\mathbf{C}\hat{\mathbf{\Phi}}\right\|_F^2 + \left\langle \mathbf{Y}, \mathbf{P} - \mathbf{B}\odot\mathbf{C}\hat{\mathbf{\Phi}}\right\rangle \\ &\quad + \frac{\mu_2}{2}\left\|\mathbf{S} - \mathbf{D}_w\mathbf{C}\hat{\mathbf{\Phi}}\mathbf{\Psi}\right\|_F^2 + \left\langle \mathbf{Z}, \mathbf{S} - \mathbf{D}_w\mathbf{C}\hat{\mathbf{\Phi}}\mathbf{\Psi}\right\rangle, \end{aligned}$$

where $\mathbf{Y}$ and $\mathbf{Z}$ are the Lagrangian multipliers and μ_1 and μ_2 are penalty parameters. The proposed algorithm that alternatively minimizes $f(\cdot)$ and updates $\mathbf{Y}$ and $\mathbf{Z}$ is then described in Algorithm 3. As shown in [117], the linear system of equations in the first step can be solved in closed-form with only two Fourier transforms, which significantly accelerates the reconstruction (avoiding the repeated Fourier transforms in each iteration for CG).

5.5 Data Processing Pipeline for ^{1}H-MRSI of the Brain

For ^{1}H-MRSI of the brain, the strong nuisance water and subcutaneous fat signals need to be removed for the SPICE reconstruction (even with suppression pulses, the residual water and fat signals can still be overwhelming). Accordingly, a recently proposed subspace-based nuisance signal removal method is included in the data processing [105]. To this end, the

Algorithm 3 The algorithm for solving Eq. (5.18).

1. For fixed $\mathbf{C}^{(i)}, \mathbf{S}^{(i)}, \mathbf{Y}^{(i)}, \mathbf{Z}^{(i)}$, update $\mathbf{P}$ by solving

$$\begin{aligned}\mathbf{P}^{(i+1)} &= \arg\min_{\mathbf{P}} \|\mathbf{s}_2 - \Omega_S\{\mathbf{FP}\}\|_2^2 + \frac{\mu_1}{2}\left\|\mathbf{P} - \mathbf{B}\odot\mathbf{C}^{(i)}\hat{\mathbf{\Phi}}\right\|_F^2 + \left\langle \mathbf{Y}^{(i)}, \mathbf{P} - \mathbf{B}\odot\mathbf{C}^{(i)}\hat{\mathbf{\Phi}}\right\rangle \\ &= \arg\min_{\mathbf{P}} \|\mathbf{s}_2 - \Omega_S\{\mathbf{FP}\}\|_2^2 + \frac{\mu_1}{2}\left\|\mathbf{P} - \mathbf{B}\odot\mathbf{C}^{(i)}\hat{\mathbf{\Phi}} + \frac{\mathbf{Y}^{(i)}}{\mu_1}\right\|_F^2,\end{aligned}$$

   which is equivalent to solving a system of linear equations but without the field inhomogeneity modeling term in Algorithm 2.

2. For fixed $\mathbf{P}^{(i+1)}, \mathbf{S}^{(i)}, \mathbf{Y}^{(i)}, \mathbf{Z}^{(i)}$, update $\mathbf{C}$ by solving

$$\begin{aligned}\mathbf{C}^{(i+1)} &= \arg\min_{\mathbf{C}} \frac{\mu_1}{2}\left\|\mathbf{P}^{(i+1)} - \mathbf{B}\odot\mathbf{C}\hat{\mathbf{\Phi}}\right\|_F^2 + \left\langle \mathbf{Y}^{(i)}, \mathbf{P}^{(i+1)} - \mathbf{B}\odot\mathbf{C}\hat{\mathbf{\Phi}}\right\rangle \\ &\quad + \frac{\mu_2}{2}\left\|\mathbf{S}^{(i)} - \mathbf{D}_w\mathbf{C}\hat{\mathbf{\Phi}}\mathbf{\Psi}\right\|_F^2 + \left\langle \mathbf{Z}^{(i)}, \mathbf{S}^{(i)} - \mathbf{D}_w\mathbf{C}\hat{\mathbf{\Phi}}\mathbf{\Psi}\right\rangle \\ &= \arg\min_{\mathbf{C}} \left\|\mathbf{B}\odot\mathbf{C}\hat{\mathbf{\Phi}} - \left(\mathbf{P}^{(i+1)} + \frac{\mathbf{Y}^{(i)}}{\mu_1}\right)\right\|_F^2 + \frac{\mu_2}{\mu_1}\left\|\mathbf{D}_w\mathbf{C}\hat{\mathbf{\Phi}}\mathbf{\Psi} - \left(\mathbf{S}^{(i)} + \frac{\mathbf{Z}^{(i)}}{\mu_2}\right)\right\|_F^2,\end{aligned}$$

   which is equivalent to solving

$$\mathbf{C}\hat{\mathbf{\Phi}}\hat{\mathbf{\Phi}}^H + \frac{\mu_2}{\mu_1}\mathbf{D}_w^H\mathbf{D}_w\mathbf{C}\hat{\mathbf{\Phi}}\mathbf{\Psi}\mathbf{\Psi}^H\hat{\mathbf{\Phi}}^H = \mathbf{B}^H\odot\left(\mathbf{P}^{(i+1)} + \frac{\mathbf{Y}^{(i)}}{\mu_1}\right)\hat{\mathbf{\Phi}}^H + \frac{\mu_2}{\mu_1}\mathbf{D}_w^H\left(\mathbf{S}^{(i)} + \frac{\mathbf{Z}^{(i)}}{\mu_2}\right)\mathbf{\Psi}^H\hat{\mathbf{\Phi}}^H,$$

   where $\mathbf{B}$ and $\mathbf{B}^H$ cancel each other and $\mathbf{\Psi}\mathbf{\Psi}^H = \mathbf{I}$ if $\mathbf{\Psi}$ is an orthogonal transform.

3. For fixed $\mathbf{P}^{(i+1)}, \mathbf{C}^{(i+1)}, \mathbf{Y}^{(i)}, \mathbf{Z}^{(i)}$, update $\mathbf{S}$ by solving

$$\begin{aligned}\mathbf{S}^{(i+1)} &= \arg\min_{\mathbf{S}} \lambda_c\|\mathbf{S}\|_1 + \frac{\mu_2}{2}\left\|\mathbf{S} - \mathbf{D}_w\mathbf{C}^{(i+1)}\hat{\mathbf{\Phi}}\mathbf{\Psi}\right\|_F^2 + \left\langle \mathbf{Z}^{(i)}, \mathbf{S} - \mathbf{D}_w\mathbf{C}^{(i+1)}\hat{\mathbf{\Phi}}\mathbf{\Psi}\right\rangle \\ &= \arg\min_{\mathbf{S}} \lambda_c\|\mathbf{S}\|_1 + \frac{\mu_2}{2}\left\|\mathbf{S} - \mathbf{D}_w\mathbf{C}^{(i+1)}\hat{\mathbf{\Phi}}\mathbf{\Psi} + \frac{\mathbf{Z}^{(i)}}{\mu_2}\right\|_F^2.\end{aligned}$$

4. Update $\mathbf{Y}$ and $\mathbf{Z}$ as

$$\begin{aligned}\mathbf{Y}^{(i+1)} &= \mathbf{Y}^{(i)} + \mu_1\left(\mathbf{P}^{(i+1)} - \mathbf{B}\odot\mathbf{C}^{(i+1)}\hat{\mathbf{\Phi}}\right) \\ \mathbf{Z}^{(i+1)} &= \mathbf{Z}^{(i)} + \mu_2\left(\mathbf{S}^{(i+1)} - \mathbf{D}_w\mathbf{C}^{(i+1)}\hat{\mathbf{\Phi}}\mathbf{\Psi}\right)\end{aligned}$$

5. Repeat 1-4 until the same convergence criterion as in Algorithm 2 is met.

MPRAGE image will be interpolated and registered to the grids of the spectroscopic data. Spatial supports for water and subcutaneous fat layers are obtained from the interpolated image through segmentation and used for water/fat removal. Since multiple coils are used for acquisition in practical imaging experiments, the removal is applied coil by coil to both $\mathcal{D}_1$ and $\mathcal{D}_2$. Afterwards, the nuisance signal removed $\mathcal{D}_1$ data are combined using an SVD-based scheme [124] for subsequent field inhomogeneity correction and subspace estimation. The estimated subspace ($\hat{\mathbf{\Phi}}$) is then used for spatial coefficient estimation, which is also performed in a coil-by-coil fashion followed by an SVD-based combination to form the final spatiotemporal reconstruction. Figure 5.1 explains the entire data processing pipeline for ^{1}H-MRSI of the brain using SPICE.

5.6 Numerical Results

In this section, some representative simulation results will be shown to illustrate the properties of the proposed reconstruction methods. To this end, we use the numerical phantom described in Chapter 3. The plots in Fig. 5.2b show the projection errors for subspaces estimated from field inhomogeneity corrupted and field corrected $\mathcal{D}_1$ with various k-space coverages. As can be seen, the proposed regularized reconstruction methods can effectively reduce the effects of field inhomogeneity with only a limited number of spatial encodings (e.g., 12×12). Compared to the projection errors in Fig. 5.2a which were generated from $\mathcal{D}_1$ corrupted only by noise (matching the SNR of the data used to generate Fig. 5.2b), the residual projection error is dominated by noise effects. This again indicates the effectiveness of field inhomogeneity correction. Furthermore, the difference between before and after field inhomogeneity correction becomes more distinct if we have stronger field inhomogeneity, as shown by Fig. 5.2c, the results in which were generated from data corrupted by twice stronger field inhomogeneity.

Figure 5.3 compares SPICE reconstructions using different regularization terms. The subspace was estimated from a field corrected $\mathcal{D}_1$ with 12×12 spatial encodings. For a

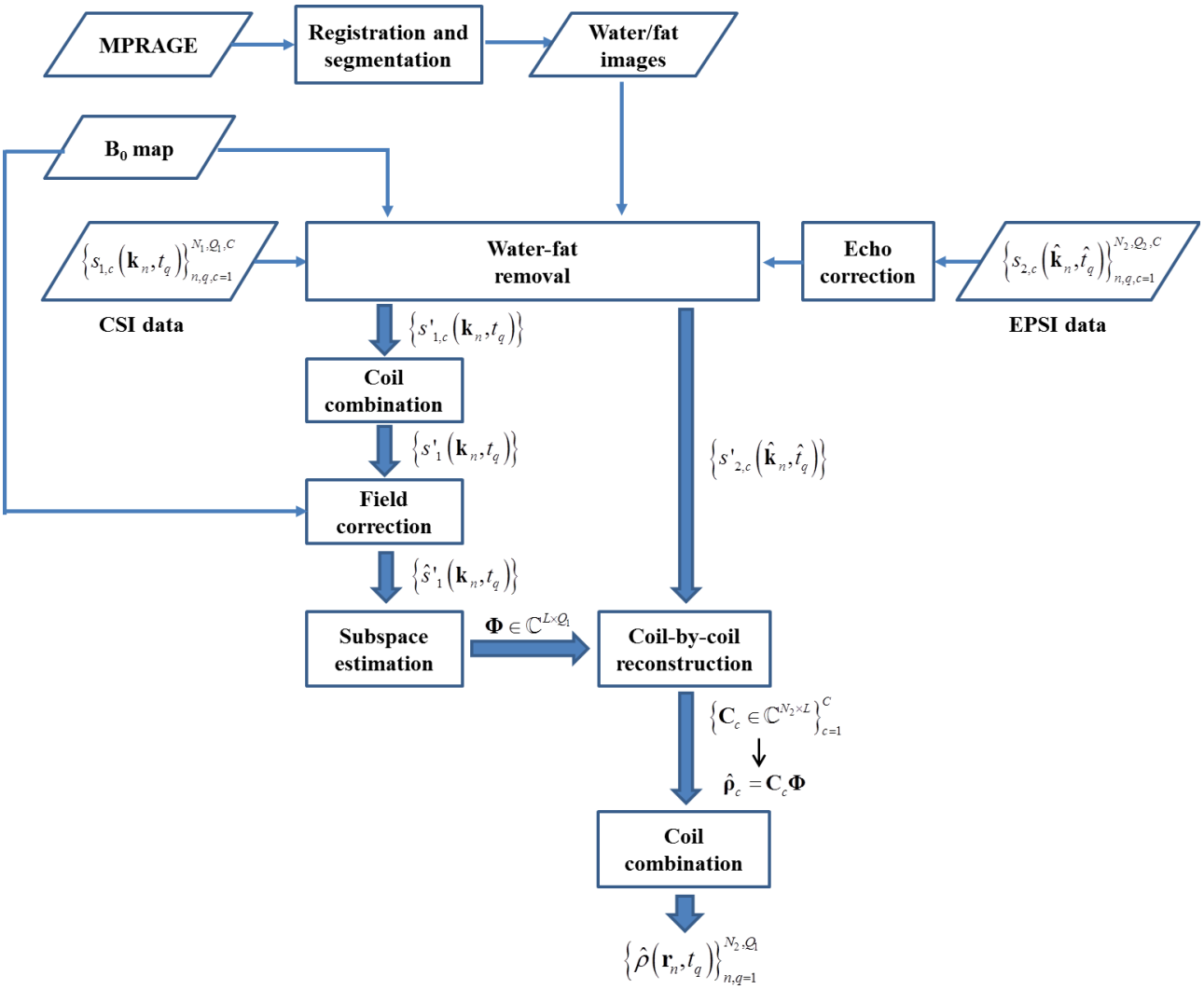

Figure 5.1: The data processing and reconstruction pipeline of SPICE for ^{1}H-MRSI data acquired from the brain. Please refer to the text in Section 5.5 for explanation of each step.

quantitative comparison of the reconstructions, we computed the following error:

$$\mathrm{RE}_{\boldsymbol{\rho}} = \frac{\|\boldsymbol{\rho}_0 - \hat{\boldsymbol{\rho}}\|_F}{\|\boldsymbol{\rho}_0\|_F}, \tag{5.19}$$

where $\boldsymbol{\rho}_0$ is the gold standard and $\hat{\boldsymbol{\rho}}$ is the reconstruction. A CSI reconstruction corresponding to an equivalent-time acquisition is also shown for comparison. As can be seen, SPICE reconstructions achieve significant improvement over the CSI reconstruction, with the ℓ_1 regularization (Eq. (5.8)) providing a further reduced error.

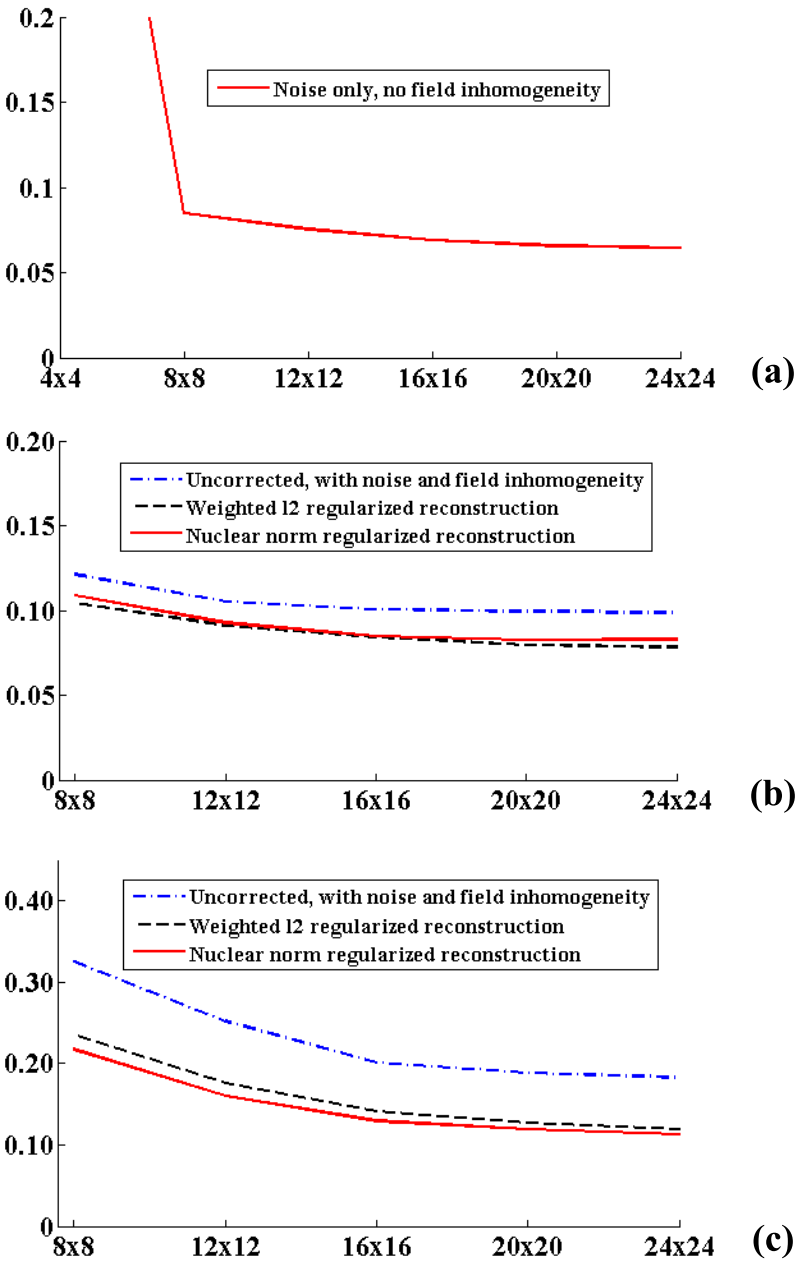

Figure 5.2: Projection errors for subspaces estimated from $\mathcal{D}_1$ with various sizes. (a) shows the projection errors due to random measurement noise corruption alone; (b) compares the projection errors before and after field inhomogeneity correction with the SNR matching the data for (a); (c) compares the projection errors before and after field inhomogeneity correction for $\mathcal{D}_1$ corrupted by twice stronger field inhomogeneity. The x-axis denotes the number of spatial encodings in $\mathcal{D}_1$ and the y-axis denotes the projection error.

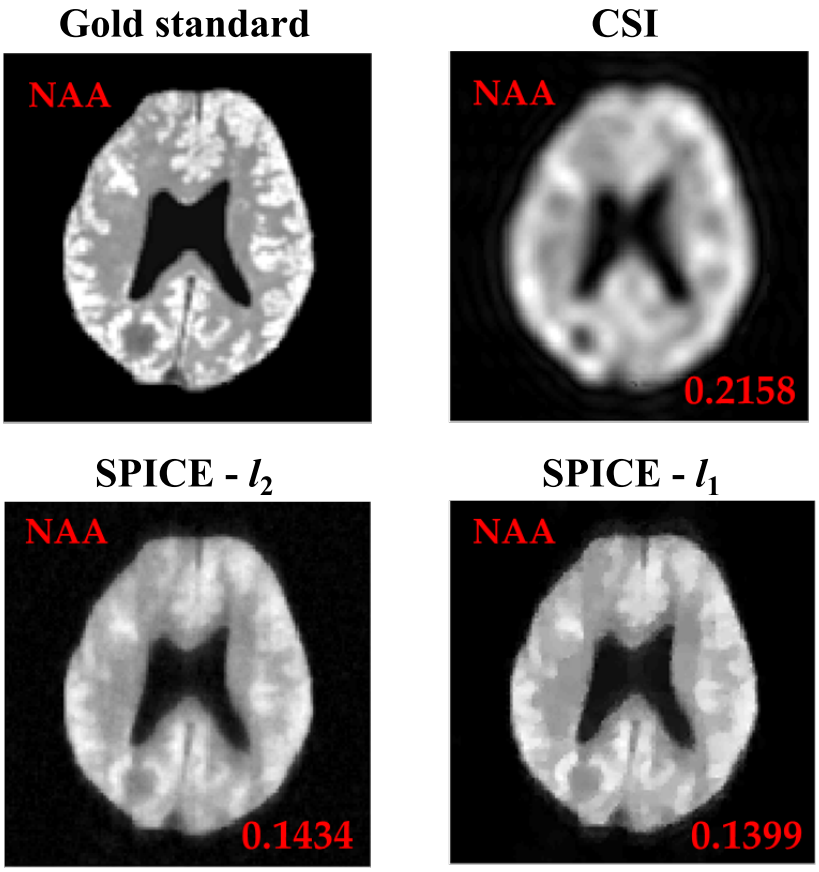

Figure 5.3: Comparison of the NAA maps from the gold standard, the CSI reconstruction, the SPICE reconstructions with weighted-ℓ_2 regularization (SPICE-ℓ_2) and ℓ_1 regularization (SPICE-ℓ_1). The CSI and SPICE reconstructions were obtained from data with the same number of excitations. The red letters in the bottom right corners show the reconstruction error defined in Eq. (5.19).

5.7 Summary

Special reconstruction methods for accurate subspace estimation from $\mathcal{D}_1$ with limited k-space coverage and high-resolution spatial coefficient estimation from noisy $\mathcal{D}_2$ with limited spectral encoding have been developed for SPICE reconstruction. With the subspace determined from $\mathcal{D}_1$, the spatiotemporal reconstruction problem can be translated into the estimation of a set of spatial coefficients, which have a significantly reduced number of degrees-of-freedom compared to the high-dimensional spatiotemporal function of interest (rendering high SNR reconstruction from the very noisy and sparse data possible). This problem is then formulated into a regularized linear least-squares estimation (optimal in

the sense of penalized maximum likelihood) that incorporates an explicit low-rank model with the capability to incorporate field inhomogeneity correction and edge-preserving regularization. Efficient numerical algorithms have been developed to address the computational challenges associated with the proposed reconstruction methods. Finally, a complete SPICE processing pipeline for brain ^{1}H-MRSI data is constructed.

CHAPTER 6

EXPERIMENTAL RESULTS

Phantom and in vivo experiments have been conducted to evaluate the performance of the proposed methods for 2D and 3D high-resolution ^{1}H-MRSI using SPICE. All the phantom and in vivo experiments are performed on a 3T Siemens Trio scanner (Siemens Healthcare USA) equipped with a 12-channel receiver headcoil.

6.1 Phantom Experiments

Two physical phantoms were constructed for experimental studies. Both phantoms are cylindrical jars (made with polymethylpentene) containing NaCl-doped water and vials of different sizes. The first one has five vials (Fig. 6.1a), which are filled with metabolite solutions with various concentrations. Specifically, vial 1 contains 20 mmol/L NAA, 15 mmol/L Cr and 10 mmol/L Cho (choline-chloride); vial 2 contains 20 mmol/L NAA, 10 mmol/L Cr and 5 mmol/L Cho; vial 3 contains NAA, Cr, Cho and mI all at 10 mmol/L; vial 4 contains 15 mmol/L NAA, 8 mmol/L Cr and 5 mmol/L Cho; and vial 5 contains the same solution as vial 3. The second phantom has three rows of vials with different diameters (for the purpose of demonstrating the resolution capability of SPICE, Fig. 6.2a). Again, the vials contain solutions of NAA, Cr, Cho, and mI with physiologically relevant concentrations [14]. As illustrated in Fig. 6.2a, the top row (vials with the smallest diameter) contains 15 mmol/L NAA, 10 mmol/L Cr, 5 mmol/L Cho and 10 mmol/L mI. The middle row contains 10 mmol/L NAA, 10 mmol/L Cr, 5 mmol/L Cho and 10 mmol/L mI. The bottom row (vials with the largest diameter) contains 20 mmol/L NAA, 15 mmol/L Cr, 5 mmol/L Cho and 10 mmol/L mI.

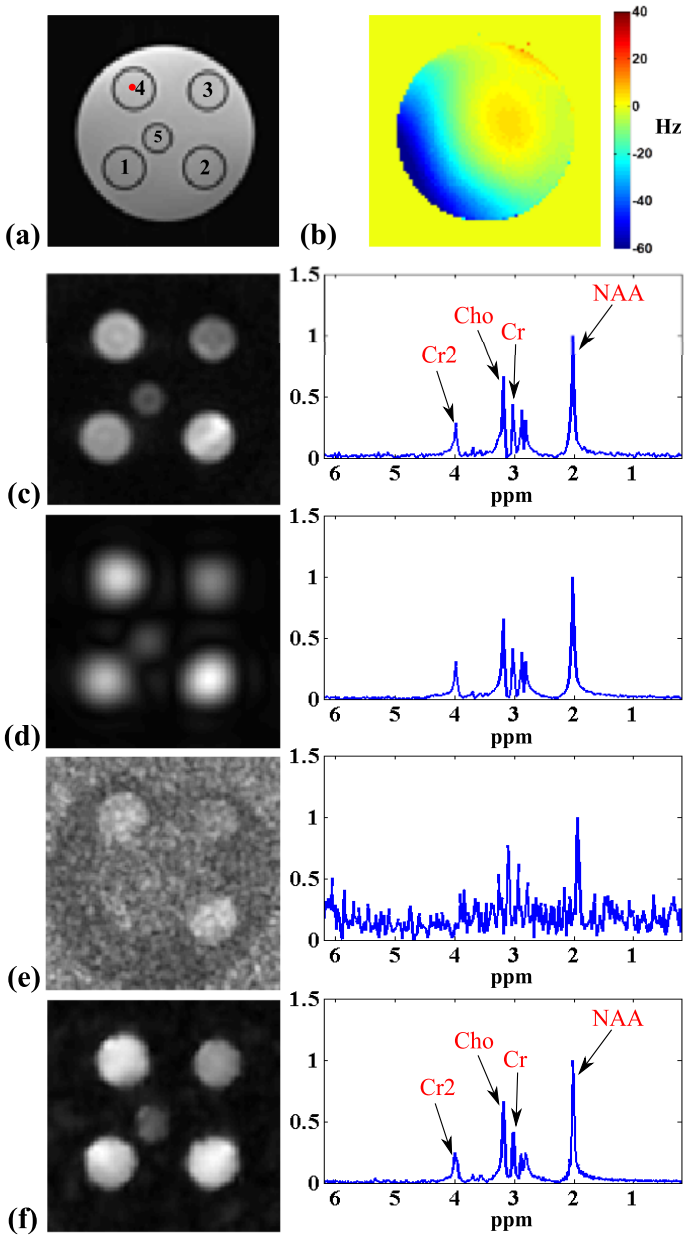

Figure 6.1: Experimental results from the first metabolite phantom shown in (a) with spectroscopic imaging data acquired in the presence of B_0 inhomogeneity shown in (b): (c) CSI reconstruction from 60×60 spatial encodings, (d) CSI reconstruction from 19×19 spatial encodings, (e) EPSI reconstruction from 100×100 spatial encodings with two averages, and (f) SPICE reconstruction with 12×12 CSI encodings in $\mathcal{D}_1$, 45 echo shifts in $\mathcal{D}_2$ with five averages, and $L = 10$. The left column shows the spatial distributions of NAA and the right column shows the spectra from the voxel identified by the red dot in (a). The results in (d)-(f) correspond to a factor of 10 reduction in data acquisition time (6 min) compared to the high-resolution CSI acquisition in (c).

6.1.1 2D SPICE

One data set was acquired from the first phantom to evaluate the performance of SPICE in a retrospective undersampling setting with comparison to two alternative accelerated MRSI methods (i.e., a low-resolution CSI scan and a conventional EPSI scan). Accordingly, a water-suppressed high-resolution CSI data set was acquired with the following imaging parameters: TR/TE = 1000/30 ms, FOV = 250×250 mm^2, slice thickness = 10 mm, VOX = $160 \times 160 \times 10$ mm^3, matrix size = 60×60, number of samples for FID = 512, and spectral BW = 2000 Hz. The duration of this acquisition was one hour. In addition, a spatiospectrally fully sampled water-suppressed EPSI data set was acquired using a customized EPSI sequence with the same parameters except: matrix size = 100×100, number of echoes = 256, readout BW = 167 kHz and echo spacing = 830 us (the time interval between k-space centers of two echoes acquired at different gradient polarities). Two temporal interleaves and five signal averages were used resulting in an acquisition time of 16.7 minutes. For both the CSI and EPSI data, the water suppression BW was 80 Hz [111]. The HSVD algorithm [125] was then used to further remove any residual water signal from both data sets.[1] A GRE reference image (Fig. 6.1a) for extracting edge information (i.e., defining $\mathbf{W}$) and a ΔB_0 map were acquired with matched slice location, FOV and slice thickness. In addition, to ensure a reasonable initial ΔB_0 distribution, manual shimming was performed before data acquisition, using up to second-order shimming gradients available on the scanner (which was done for all our MRSI experiments).

A field inhomogeneity corrected reconstruction was first obtained from the 60×60 CSI data using the conjugate phase (CP) method [107] to create a reference for comparing three acceleration methods: (i) SPICE, (ii) low-resolution CSI, and (iii) EPSI, with the same data acquisition time (6 minutes). The corresponding SPICE data set contained $\mathcal{D}_1$ with 12×12 spatial encodings and $\mathcal{D}_2$ with 45 echo shifts each having 100×100 spatial encodings averaged five times. The $\mathcal{D}_2$ here was retrospectively sampled from the full EPSI data following the trajectories shown in Fig. 3.1 and only the data acquired on the positive gradients were used (bypassing the echo inconsistency correction step). With the same acquisition time (6

[1] HSVD can be used directly in this case because both data sets are spatiospectrally fully sampled.

minutes), the low-resolution CSI scan generated 19×19 spatial encodings while the high-resolution EPSI scan generated 100×100 spatial encodings averaged twice. The SPICE reconstruction was performed using the water-removed data following the procedures shown in Fig. 5.1, with $L = 10$ and λ_f and λ_c chosen using the discrepancy principle [126]. Field corrected CP reconstructions were obtained from the equivalent-time CSI and EPSI scans for comparison.

Figure 6.1 shows a set of results from the above described data. The spatial distributions of NAA were obtained by the following spectral integration method:

$$\mathbf{I}_n^{(NAA)} = \frac{\sqrt{\sum_{q\in\omega_{NAA}} |\hat{\boldsymbol{\rho}}(\mathbf{r}_n, f_q)|^2}}{|\omega_{NAA}|}, \tag{6.1}$$

where $\mathbf{I}_n^{(NAA)}$ denotes the NAA intensity at the nth voxel, $\hat{\boldsymbol{\rho}}(\mathbf{r}, f)$ the reconstructed spatiospectral function and ω_{NAA} the index set for the NAA frequency range with $|\omega_{NAA}|$ being its cardinality. As can be seen, the low-resolution CSI reconstruction has high SNR but suffers from serious blurring and ringing artifacts (due to the truncation in k-space) in the NAA map. The EPSI reconstruction has high spatial resolution but very low SNR due to the small voxel size and the high readout BW, as expected. Meanwhile, SPICE achieves both high spatial resolution (significantly better than the CSI reconstruction) and high SNR (significantly better than the EPSI reconstruction) with the same acquisition time. Note also that the SPICE reconstruction has SNR comparable to that of the high-resolution CSI reconstruction (see the spectra in the right column of Fig. 6.1), but with a factor of 10 acceleration in data acquisition.

Another data set was acquired from the second metabolite phantom using the proposed 2D SPICE sequence (Fig. 4.1) to evaluate the performance of SPICE in an actual prospective sparse sampling setting. The SPICE data includes 12×12 CSI encodings in $\mathcal{D}_1$, each having 512 temporal samples, and 80×80 spatial encodings in $\mathcal{D}_2$, each having 128 echoes. Six averages were acquired for $\mathcal{D}_2$ (with a factor of 9/10 partial Fourier sampling), making the total acquisition time about 10 minutes. An equivalent-time CSI acquisition with 24×24 spatial encodings was performed. The other relevant imaging parameters were (for both CSI

and SPICE): FOV = 220 × 220 mm^2, VOX = 160 × 160 × 10 mm^3, TR/TE=1000/30 ms, water suppression BW=80 Hz, and delta frequency (for PRESS excitation)=-2.4 ppm (water at 0 ppm). The sampling BWs for the CSI and EPSI acquisitions were 2 kHz and 100 kHz, respectively. The echo spacing for $\mathcal{D}_2$ was 1030 μs.

Some representative results from this phantom experiment are shown in Fig. 6.2 to Fig. 6.5. For SPICE reconstruction, the field corrected reconstruction (Eq. (5.4)) for $\mathcal{D}_1$ was performed on 64×64 grids. A subspace with a model order of $L = 6$ was then estimated from the field corrected $\mathcal{D}_1$ and used for the spatial coefficient estimation. λ_f and λ_c were selected such that the residual from the data consistency term was slightly lower than a pre-estimated total noise variance [126]. The reconstruction from the 24×24 CSI data was obtained by a field inhomogeneity corrected CP reconstruction on 80×80 grids. All reconstructions were zero-filled to 100×100 for comparison.

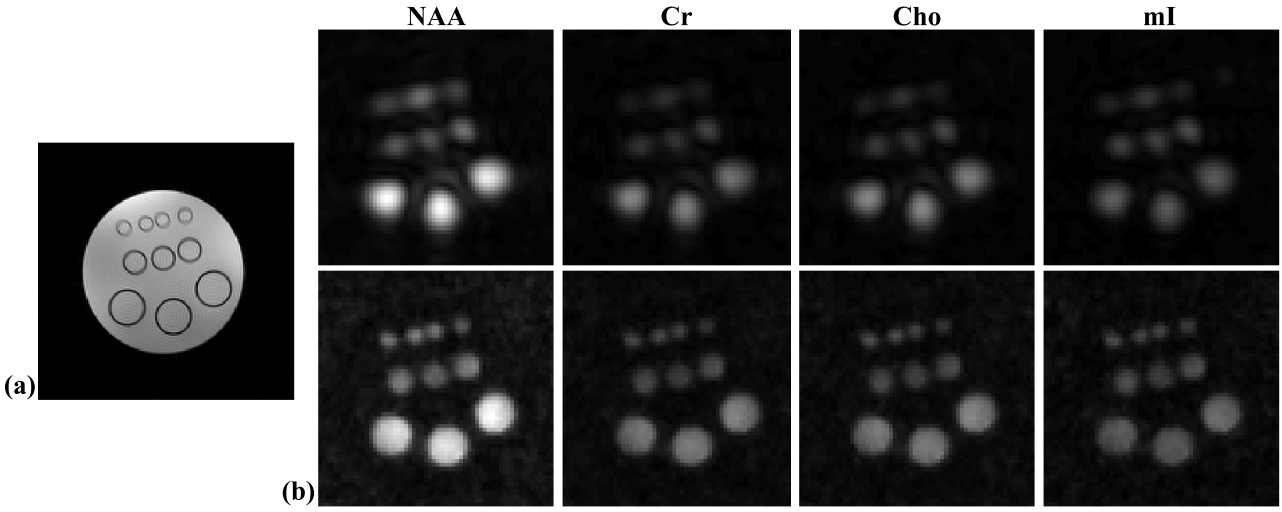

Figure 6.2: Experimental results from the second metabolite phantom. The GRE image in (a) shows the structural arrangement of this phantom. The images in (b) compare the spatial maps (obtained by peak integral) of NAA, Cr, Cho and mI for CSI (top row) reconstruction and SPICE (bottom row) reconstruction ($L = 6$). The CSI and SPICE have the same data acquisition time. The NAA maps were normalized such that the maximum intensity is 1 (for both CSI and SPICE), while the other metabolite maps were normalized to the NAA maps.

Figure 6.2 compares the spatial distributions of NAA, Cr, Cho and mI from the 10 min CSI and SPICE. The spatial distributions were obtained by integrating around the strongest

peaks for each metabolite using Eq. (6.1). As expected, the CSI reconstruction has high SNR but very low resolution. With the same data acquisition time, SPICE achieves high spatial resolution while maintaining very high SNR. In particular, the vials at the first and second rows (with the smallest and medium diameters) are severely blurred in the CSI reconstruction while even the smallest vials can be clearly distinguished in the SPICE reconstruction (e.g., the center two which are merged together in the CSI reconstruction), which demonstrates the better detection of smaller features offered by SPICE. This resolution capability of SPICE is further demonstrated by the line plots shown in Fig. 6.3. Figure 6.4 compares the spectra from the CSI and SPICE reconstructions. As can be seen, the SPICE reconstruction maintains very high spectral quality (e.g., nice lineshapes and peak ratios). Furthermore, the comparison of NAA peak SNR for CSI and SPICE shown in Fig. 6.5 quantitatively demonstrates the capability of SPICE in achieving high spectral SNR, which is also important for subsequent metabolite quantification.

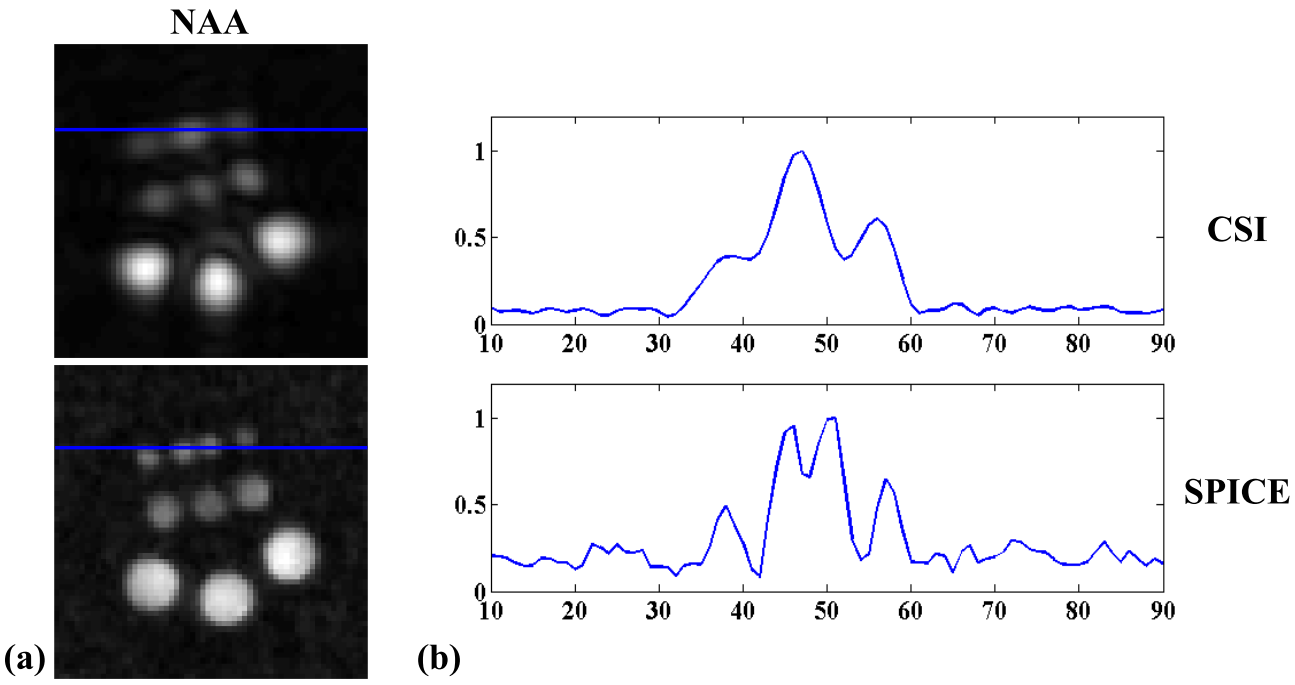

Figure 6.3: Illustration of the resolution capability of SPICE: (a) The NAA maps for CSI and SPICE as shown in Fig. 6.2; (b) 1D plots corresponding to the blue lines in (a). As can be seen, the two small vials in the center completely merge together in the lower resolution CSI while being clearly resolved by SPICE with the same data acquisition time.

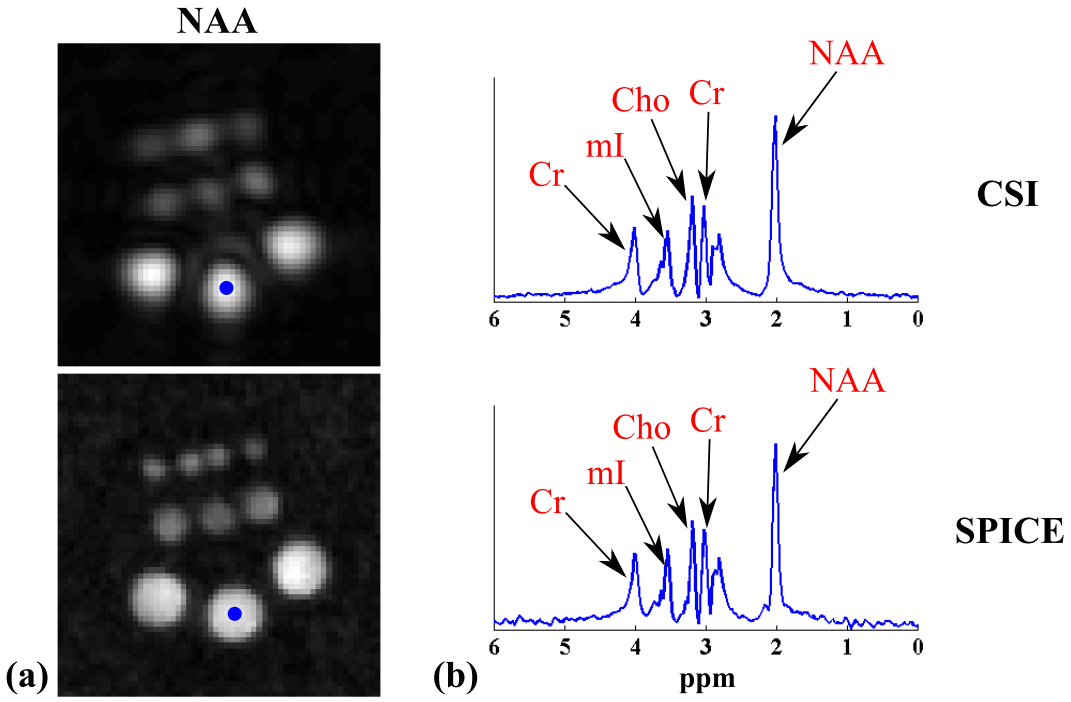

Figure 6.4: Comparison of spectra from CSI and SPICE with equivalent data acquisition time: (a) The NAA maps for CSI and SPICE as shown in Fig. 6.2; (b) representative spectra from the voxels identified by the blue dots in (a).

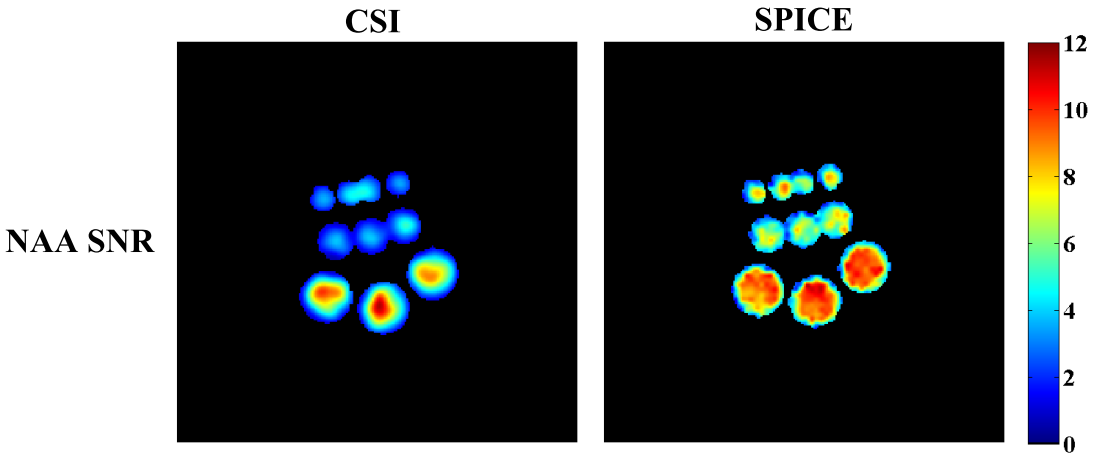

Figure 6.5: The NAA peak SNR maps for CSI (left) and SPICE (right) reconstructions. The SNR was only computed for the voxels within the supports of the vials obtained from the GRE image (since only the vials contain metabolite solution). As can be seen, SPICE achieves a similar level of SNR to the low-resolution CSI but with a more homogeneous SNR distribution within the vials, which is a result from the combination of higher spatial resolution (less partial volume effect) and spatial regularization.

6.1.2 3D SPICE

Several sets of 3D data were collected from the second phantom using the 3D SPICE sequence (Fig. 4.3). $\mathcal{D}_1$ (acquired by the slow EPSI scans) contained $12 \times 12 \times 12$ ($k_x - k_y - k_z$) spatial encodings each with 512 echoes. The spectral BW was about 1700 Hz. $\mathcal{D}_2$ (acquired by the rapid EPSI scans) contained 48 echo shifts (uniformly spaced by 1.57 ms) each with $72 \times 72 \times 20$ spatial encodings. Other related imaging parameters were: FOV=$220 \times 220 \times 72$ mm^3, VOX=$160 \times 160 \times 56$ mm^3, TR/TE=1000/30ms, and water suppression BW=80 Hz. The sampling BWs for the slow and rapid EPSI scans were 60 and 100 kHz, respectively. The total acquisition time was about 19 minutes. As described in Chapter 4, a multi-slice high-resolution GRE scan (36 slices) was performed. The field map scan had a matrix size of $110 \times 110 \times 36$ (isotropic 2 mm resolution) and TR/TE1/TE2=700/9.8/12.3 ms. Both scans were coregistered to the spectroscopic data.

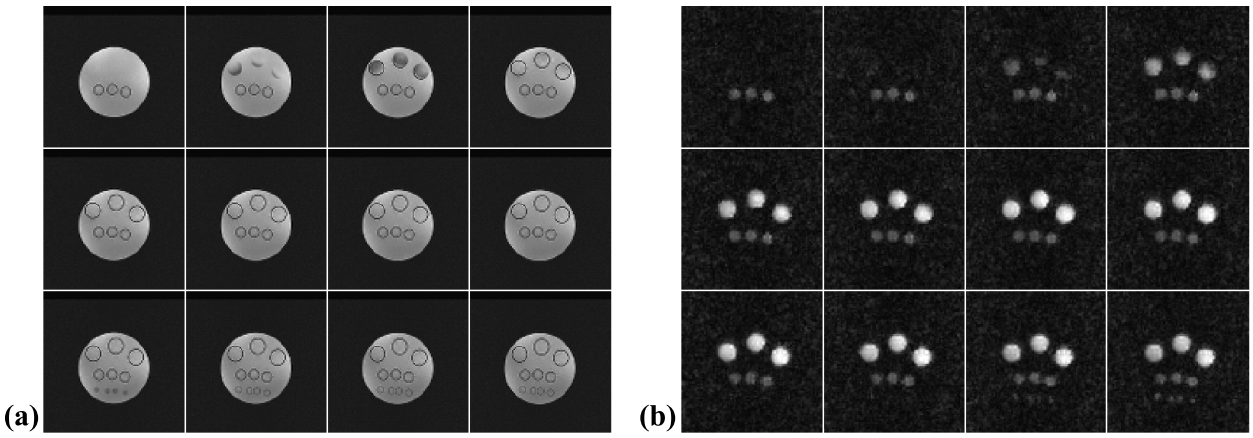

Figure 6.6: Phantom results obtained by 3D SPICE: (a) the center 12 slices from the GRE image of the phantom; (b) the NAA maps for the corresponding slices.

A set of representative results from the above described data is shown in Fig. 6.6. The field corrected reconstruction for $\mathcal{D}_1$ was done on $64 \times 64 \times 24$ grids. The high-resolution field maps were resampled to the reconstruction grid size for the field correction. A temporal subspace with $L = 8$ was estimated from the field corrected $\mathcal{D}_1$ and used for spatial coefficient estimation. The reconstructions were zero-filled to a matrix size of $100 \times 100 \times 24$ for visualization. As shown by the NAA spatial distributions in Fig. 6.6b, SPICE achieved very high spatial resolution with very high SNR, clearly resolving the smallest vials and cross-slice

variations in the 3D NAA distribution.

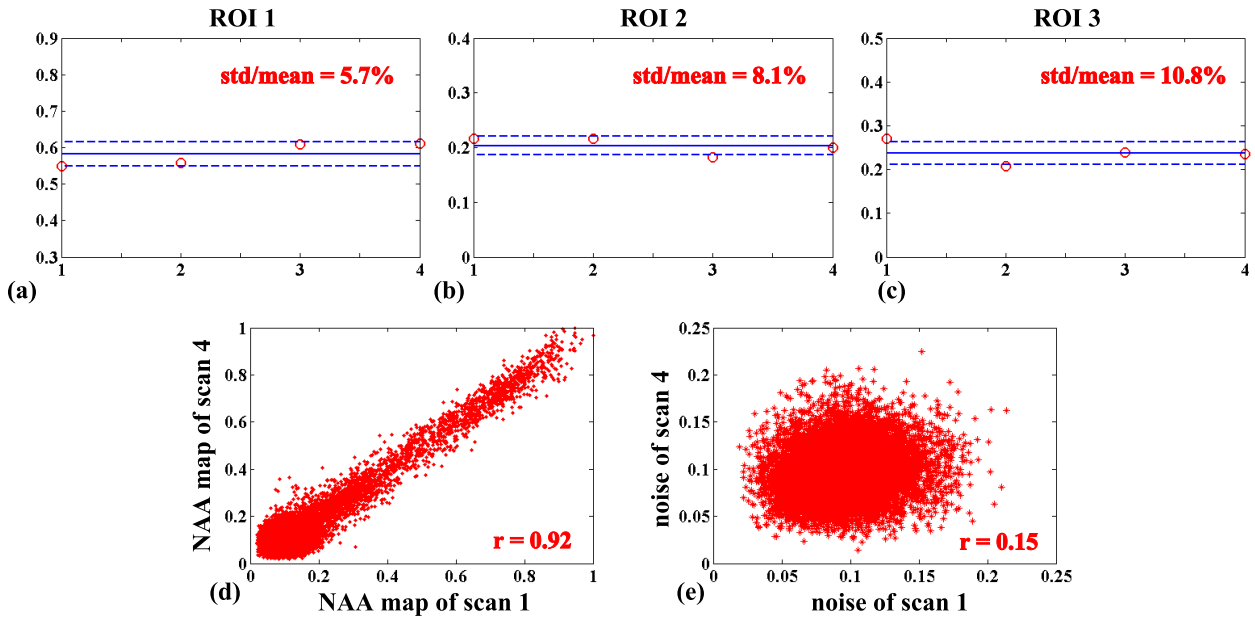

Figure 6.7: Reproducibility results (phantom) for SPICE: (a)-(c) show the mean intensities of NAA from three regions of interest (ROIs) for the four repeated scans; (d) plots the NAA intensities for scan 1 versus those for scan 4; and (e) plots the noise samples from the background for scan 1 versus those for scan 4. The solid lines in (a)-(c) stand for the mean of the four scans and the dash lines represent the standard deviation (std).

Figure 6.7 shows a set of results demonstrating the reproducibility of SPICE. In this experiment, four 3D SPICE data sets were acquired with the same imaging parameters. The GRE image was acquired only once while the field mapping scan was repeated for each 3D acquisition (to account for the B_0 field changes during this long scan). SPICE reconstructions were generated from each data with the same reconstruction parameters. As shown by the mean intensities of NAA in three regions of interest (selected from one vial in each row) and the plot of NAA intensities obtained from scan 1 versus those from scan 4 (in Fig. 6.7), SPICE achieves very high repeatability (less than 10% variance) even at this high spatial resolution. In particular, the NAA maps from different scans are highly correlated (e.g., the correlation coefficient is 0.92 for scans 1 and 4, Fig. 6.7d) while the noise samples from the background region show negligible correlation (Fig. 6.7e), which means the strong correlation in the estimated metabolite distributions does not come from a strong bias

introduced by the model or the regularized reconstruction.

6.2 In Vivo Experiments

In vivo brain ^{1}H-MRSI data were acquired from healthy volunteers with the approval from the Institutional Review Board at the University of Illinois and written consent from the participants. Several different data sets were obtained for a more comprehensive assessment of the performance of the proposed methods for 2D and 3D in vivo MRSI.

6.2.1 2D SPICE

An in vivo 2D SPICE data set that contains $\mathcal{D}_1$ with 12×12 CSI encodings each having 512 temporal samples and $\mathcal{D}_2$ with 80×80 spatial encodings each having 120 echoes was acquired. Eight signal averages were used for $\mathcal{D}_2$. The total data acquisition time was about 20 minutes. The rest of the imaging parameters were: FOV = 220×220 mm^2, VOX = $145 \times 150 \times 10$ mm^3, TR/TE=1600/30 ms and water suppression BW=80 Hz. Eight OVS slabs with 30 mm thickness were included for lipid suppression. The sampling BWs for the CSI and EPSI components were 2 kHz and 100 kHz, respectively. The auxiliary data, including an MPRAGE scan and a ΔB_0 mapping scan were obtained as described in Section 4.3. In addition, an equivalent-time (20 min) CSI acquisition with 27×27 spatial encodings was also performed for comparison.

Figure 6.8 compares the spatial distributions of NAA, Cr, Cho and Glx (glutamine+glutamate) from the 20 min CSI and SPICE described above along with representative spectra from one voxel. The CSI reconstruction and the field inhomogeneity correction for $\mathcal{D}_1$ in SPICE were performed on 64×64 grids. A temporal subspace with dimensionality $L = 8$ was then estimated from the corrected $\mathcal{D}_1$ and used for spatial coefficient estimation. All reconstructions were zero-filled to a 128×128 matrix size for visualization purpose. As can be seen, SPICE yields SNR similar to CSI, but resolution significantly higher (e.g., better defined ventricle structure) than CSI, which suffers from severe k-space truncation artifacts. In addition, the spectrum from the SPICE reconstruction seems to provide better lineshapes than that from

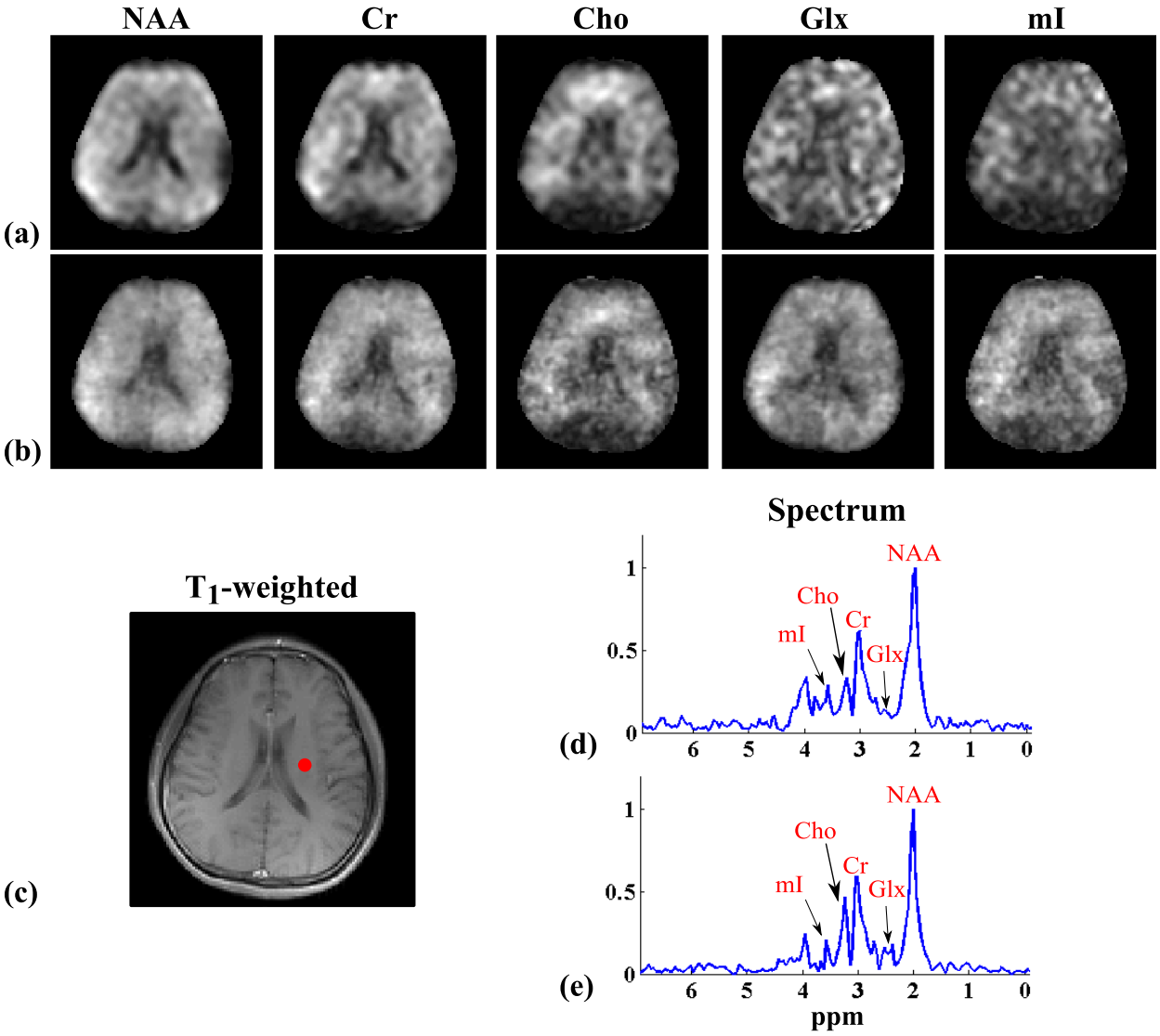

Figure 6.8: Brain ^{1}H-MRSI results from the 27×27 CSI (a) and the 80×80 SPICE (b) with equivalent data acquisition times. In particular, the spatial distributions of NAA (first column), Cr (second column), Cho (third column), Glx (fourth column, glutamine+glutamate) and mI (fifth column) are shown, as well as representative spectra from CSI (d) and SPICE (e) corresponding to the voxel identified by the red dot in the T_1-weighted image in (c). The spatial maps were normalized for each metabolite individually.

CSI, which we suspect is due to less partial volume and voxel interference that result from higher spatial resolution. Figure 6.9 shows an array of spectra from different voxels in the CSI and SPICE reconstructions. It can be clearly observed that SPICE produced spectra with very high quality while revealing more spatial heterogeneity.

Figure 6.10 compares metabolite maps from a data set acquired at a different slice location

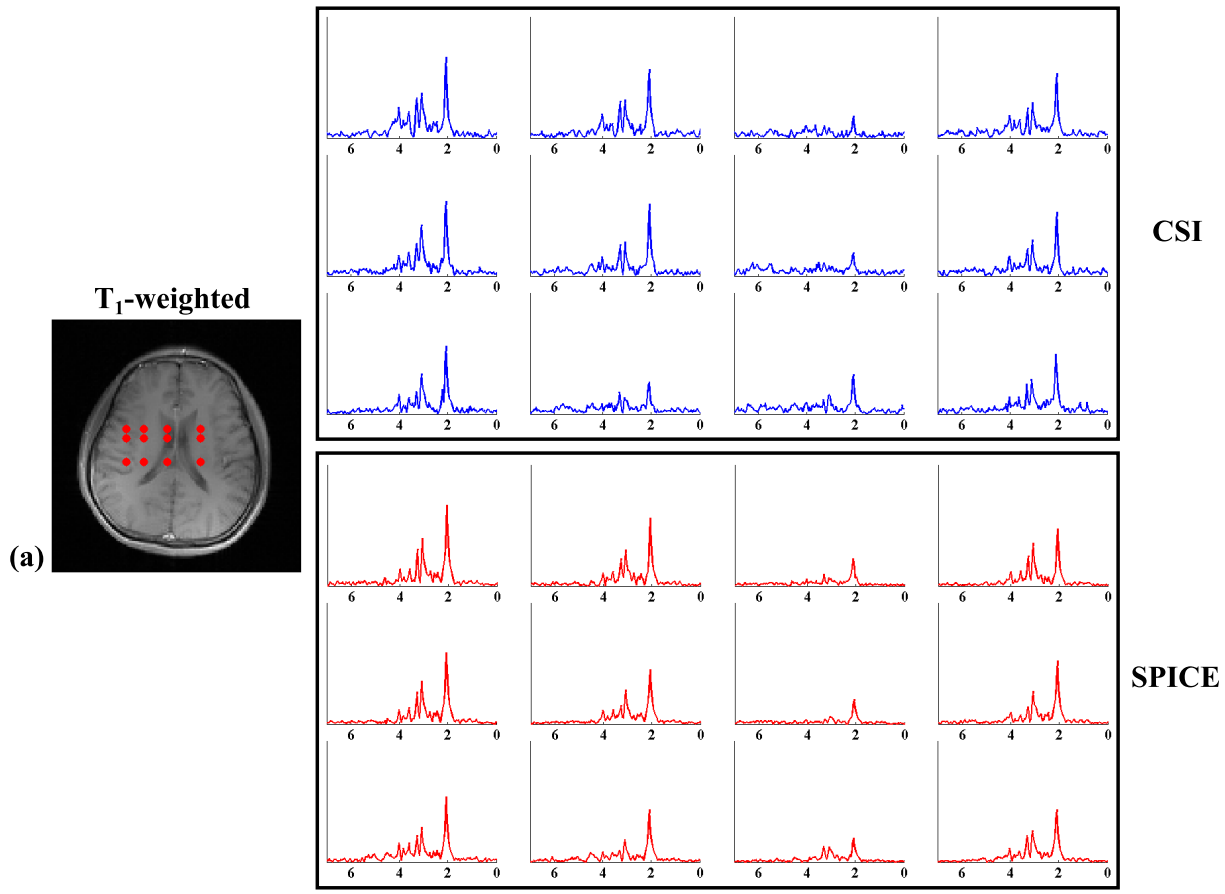

Figure 6.9: Comparison of spectra from different voxels for the CSI and SPICE results shown in Fig. 6.8. The spectra from CSI are shown in blue while the spectra from SPICE are shown in red. The corresponding locations of the voxels are indicated by the red dots in the T_1-weighted image in (a).

from the same subject. The corresponding acquisition parameters were the same as the first data set. As can be seen, SPICE again achieves high spatial resolution as well as very good SNR. Particularly, note that the longitudinal fissure (supposed to have negligible brain metabolite contents) is clearly visible in the SPICE reconstruction while not so in the CSI reconstruction due to lower resolution. Figure 6.11 compares the spectra from a given spatial location in the CSI and SPICE reconstructions shown in Fig. 6.10. Similar spectrum quality is observed.

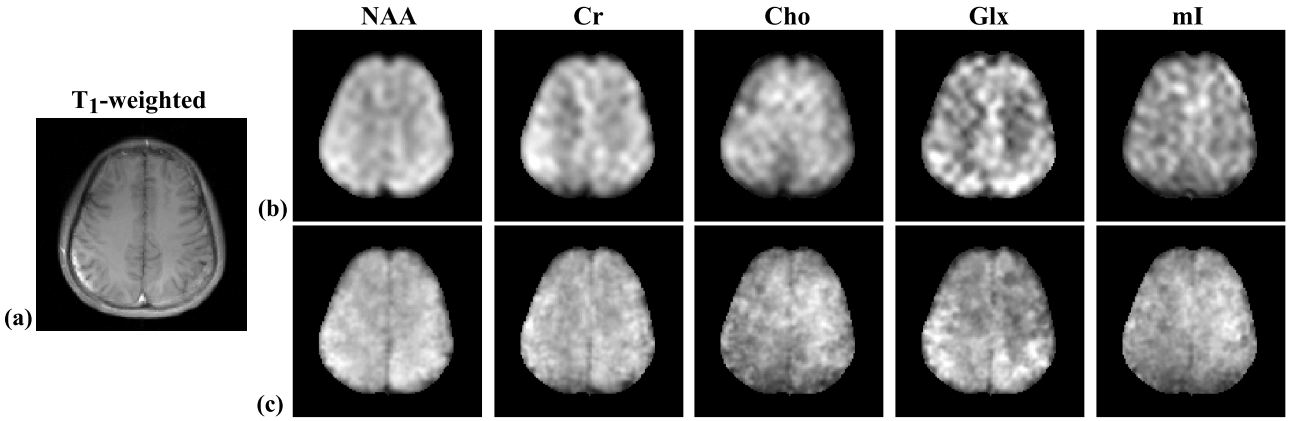

Figure 6.10: Brain ^{1}H-MRSI results from a different axial slice. The spatial distributions of NAA, Cr, Cho, Glx and mI are shown for the 27×27 CSI (row b) and 80×80 SPICE (row c, with equivalent data acquisition time). The T_1-weighted image for the corresponding slice is shown in (a). The spatial maps were normalized for each metabolite.

To further evaluate the capability of SPICE for 2D high-resolution ^{1}H-MRSI of the brain, eight different data sets were acquired. These data contained different numbers of spatiospectral encodings in both $\mathcal{D}_1$ and $\mathcal{D}_2$ acquired in different imaging times, i.e., 5 minutes, 10 minutes and 15 minutes, with the same FOV and VOX. A detailed description of the imaging parameters for these data is shown in Table 6.1.

Figure 6.12 shows the NAA maps from the SPICE acquisitions described in Table 6.1, with different rows referring to different imaging times and different columns referring to different resolutions. As can be seen, SPICE can produce high quality metabolite distributions with a 64×64 matrix size ($\sim$3.4 mm in-plane resolution) in 5 minutes, an 80×80 matrix size ($\sim$2.75 mm in-plane resolution) in 10 minutes, and a 100×100 matrix size ($\sim$2.2 mm in-plane resolution) in 15 minutes. The gradual degradation in the image quality for the NAA

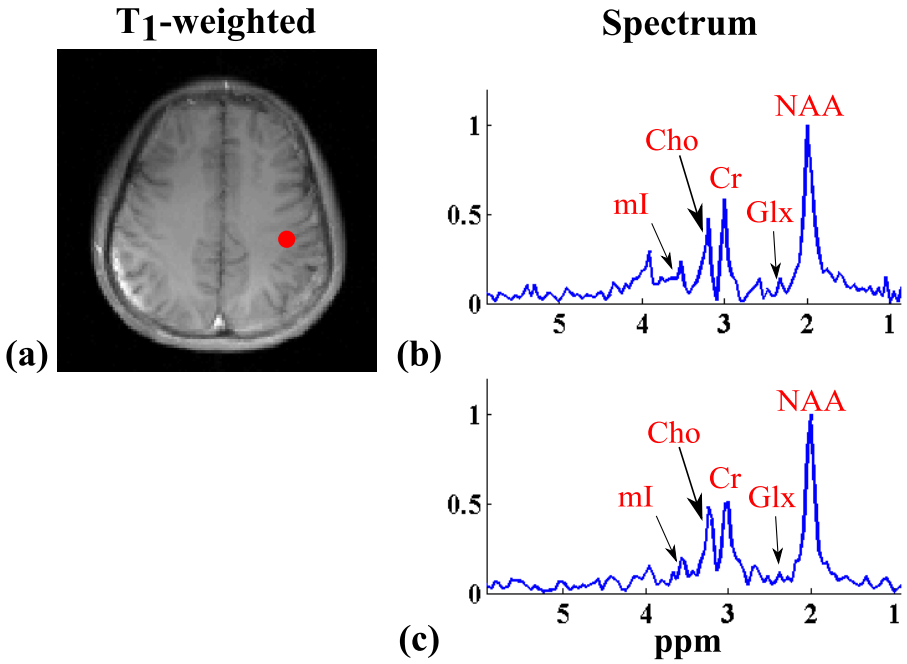

Figure 6.11: Comparison of representative voxel spectra from the CSI (b) and SPICE (c) results shown in Fig. 6.10. The corresponding location for the voxel is indicated by the red dot in the T_1-weighted image in (a).

maps resulting from pushing to higher resolution in a shorter acquisition time (as shown in the upper right triangle of the 3-by-3 matrix in Fig. 6.12) indicates that there is still considerable room for improvement (e.g., using shorter echo acquisitions, better reconstruction algorithms, and/or more accurate quantification methods etc.).

Figure 6.13 compares the results from equivalent time 10 min CSI, 10 min EPSI and 10 min 80×80 SPICE (with the same imaging parameters as the 10 min 80×80 SPICE acquisition described in Table 6.1 but acquired in a different session). The 10 min CSI acquisition generated 22×22 spatial encodings (resulting in an approximately 1 cc voxel size) and the 10 min EPSI acquisition generated 80×80 spatial encodings with three averages and one additional temporal interleave (to satisfy spectral Nyquist). Both the CSI and EPSI reconstructions were obtained by the CP field correction method. As can be seen from the NAA maps and representative voxel spectra, SPICE achieves significantly higher resolution than CSI and significantly better SNR than EPSI (buried under noise) with the same data acquisition time, demonstrating again the unique combination of speed, resolution and SNR it offers. The high SNR of SPICE is further quantitatively supported by the NAA peak SNR

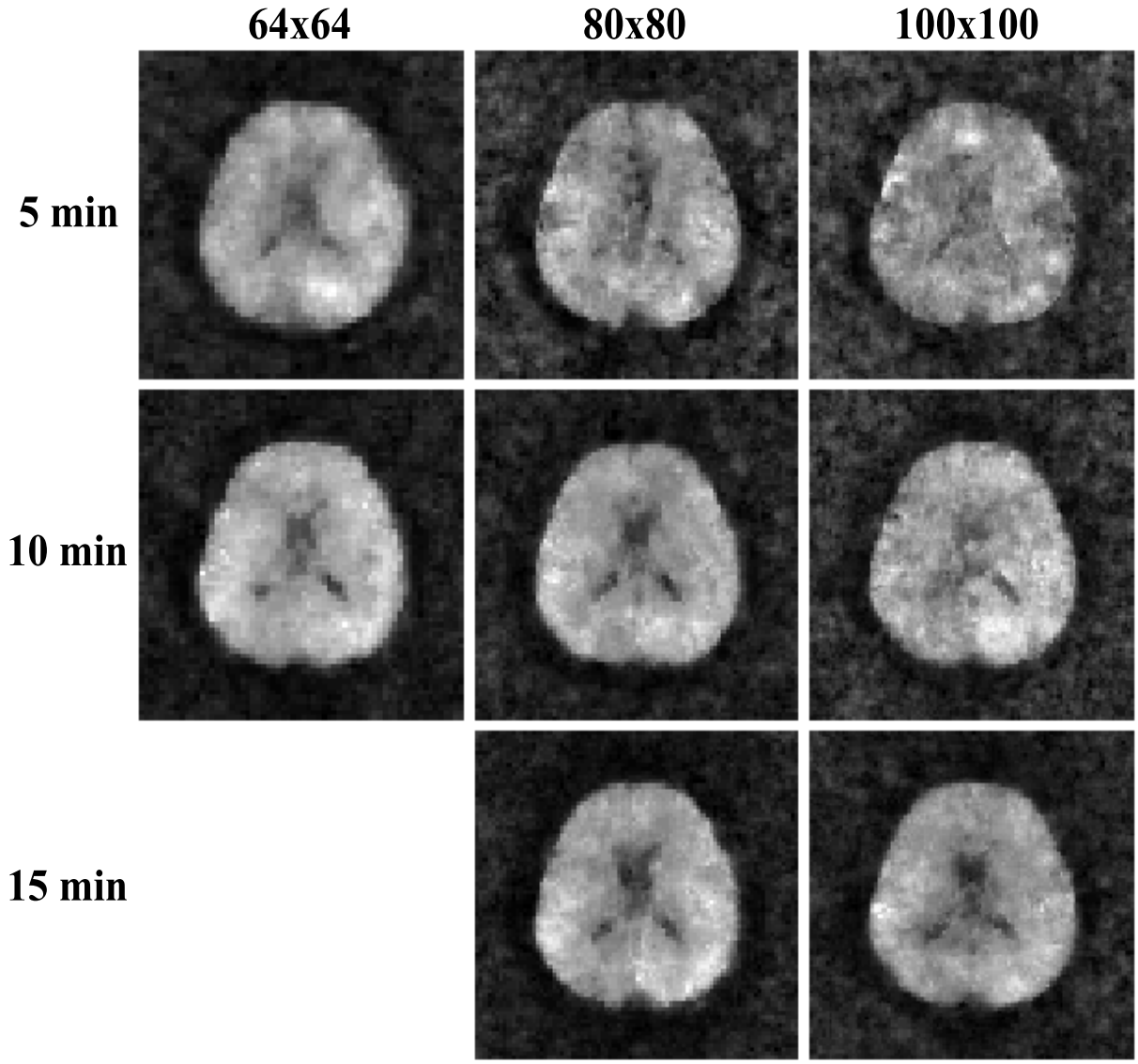

Figure 6.12: NAA maps from the 5 min (first row), 10 min (second row) and 15 min (third row) SPICE acquisitions with different matrix sizes for $\mathcal{D}_2$: 64×64 (first column); 80×80 (second column); and (c) $\mathbf{1}00 \times 100$ (third column). The SPICE reconstructions were obtained using $L = 8$ and regularization parameters selected for each acquisition such that the residuals from the data consistency term were closed to but slightly lower than the estimated total noise variances.

Table 6.1: Detailed acquisition parameters for eight 2D in vivo data sets for demonstrating the resolution and SNR capability of SPICE for high-resolution ^{1}H-MRSI of the brain.

	64×64	80×80	100×100
5 min	12×12 $\mathcal{D}_1$ 64×64 $\mathcal{D}_2$ 2 averages TR/TE = 1300/30 ms	12×12 $\mathcal{D}_1$ 80×80 $\mathcal{D}_2$ 1 average TR/TE = 1400/30 ms	12×12 $\mathcal{D}_1$ 100×100 $\mathcal{D}_2$ 1 average TR/TE = 1300/30 ms
10 min	14×14 $\mathcal{D}_1$ 64×64 $\mathcal{D}_2$ 4 averages TR/TE = 1300/30 ms	14×14 $\mathcal{D}_1$ 80×80 $\mathcal{D}_2$ 3 averages TR/TE = 1400/30 ms	14×14 $\mathcal{D}_1$ 100×100 $\mathcal{D}_2$ 3 averages TR/TE = 1200/30 ms
15 min		14×14 $\mathcal{D}_1$ 80×80 $\mathcal{D}_2$ 6 averages TR/TE = 1300/30 ms	14×14 $\mathcal{D}_1$ 100×100 $\mathcal{D}_2$ 5 averages TR/TE = 1300/30 ms

maps shown in Fig. 6.14.

6.2.2 3D SPICE

For 3D ^{1}H-MRSI experiments on the brain, a data set containing $12\times12\times12$ spatial encodings in $\mathcal{D}_1$, each having 256 echoes, and 50 echo shifts (uniformly spaced at 1.49 ms) in $\mathcal{D}_2$, each having $80 \times 80 \times 20$ spatial encodings, was acquired. The other relevant imaging parameters were: FOV=$240 \times 240 \times 72$ mm^3, VOX=$130 \times 170 \times 56$ mm^3, TR/TE=1400/30ms, and water suppression BW=80 Hz. The sampling BWs for the slow and rapid EPSI scans were 60 and 125 kHz, respectively. The total acquisition time was about 26.7 minutes. The setup for this experiment is illustrated in Fig. 6.15a. As described in Chapter 4, a coregistered multi-slice ΔB_0 map was acquired (matched FOV, matrix size = $120 \times 120 \times 36$, i.e., 2 mm isotropic resolution). An MPRAGE image was acquired (FOV = $240 \times 240 \times 192$mm^3, matrix size = $256 \times 256 \times 192$) and interpolated to the field map grids for obtaining structural information needed for processing and reconstruction. The field corrected reconstruction for $\mathcal{D}_1$ was done on $64 \times 64 \times 36$ grids using field maps resampled to the reconstruction grid size. A temporal subspace with $L = 12$ was estimated from the field corrected $\mathcal{D}_1$ and used for spatial coefficient estimation.

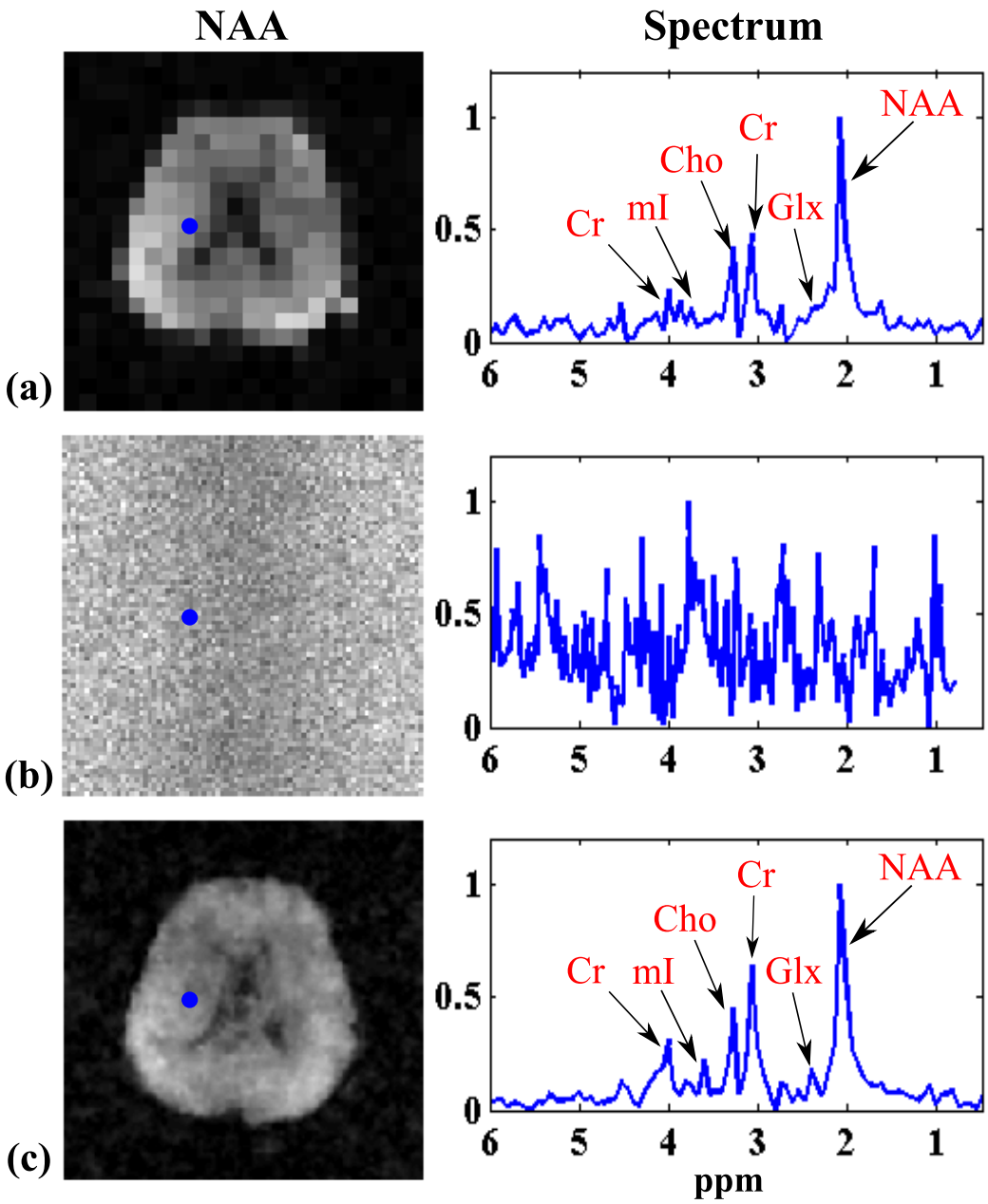

Figure 6.13: Brain ^{1}H-MRSI results from three alternative equivalent-time scans: (a) a low-resolution CSI acquisition with 22×22 spatial encodings; (b) an EPSI acquisition with 80×80 spatial encodings; and (c) a SPICE acquisition with 14×14 spatial encodings in $\mathcal{D}_1$ and 80×80 spatial encodings in $\mathcal{D}_2$. The images on the left column are NAA maps from the three acquisitions and the images on the right column are representative spectra from the voxels indicated by the blue dots in the corresponding NAA maps.

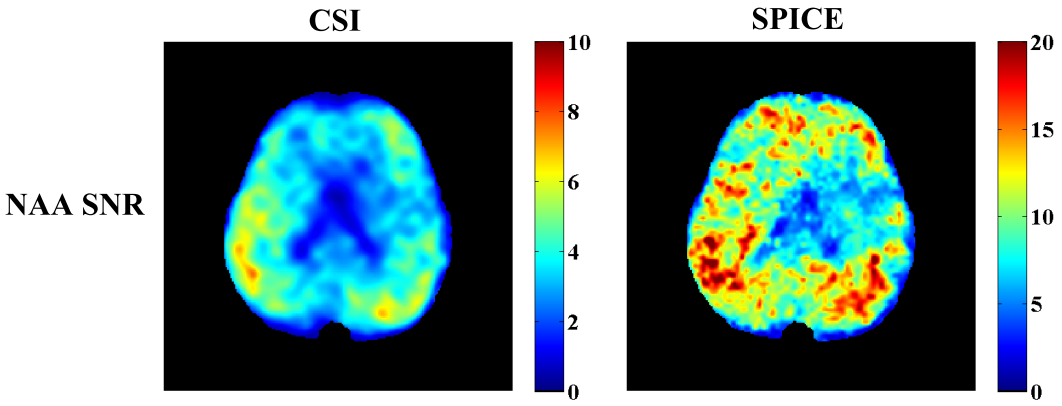

Figure 6.14: The NAA peak SNR maps for CSI (left) and SPICE (right) reconstructions from the 10 min acquisitions. The SNR was only computed for the voxels within the brain region obtained from the structural image. As can be seen, SPICE achieves a very high spectral SNR (even slightly better than the lower resolution CSI), enabled by the low-dimensional subspace structure determined from a high SNR $\mathcal{D}_1$.

Figure 6.15 displays a set of representative results from the 3D SPICE acquisition. The spatial distributions of NAA across different slices and a representative spectrum are shown. As can be seen, the SPICE reconstructions show excellent resolution and SNR, demonstrating clearly resolved cross-slice differences in metabolite distributions. To our knowledge, these are the highest resolution ^{1}H metabolite maps ever obtained from the brain on a 3T scanner.

6.3 Summary

Phantom and in vivo studies have been performed to evaluate the performance of the proposed methods for 2D and 3D high-resolution ^{1}H-MRSI using SPICE. Results from these experiments demonstrate the capability of the proposed methods in achieving unprecedented combinations of spatial resolution, SNR and imaging speed for ^{1}H-MRSI of the brain.

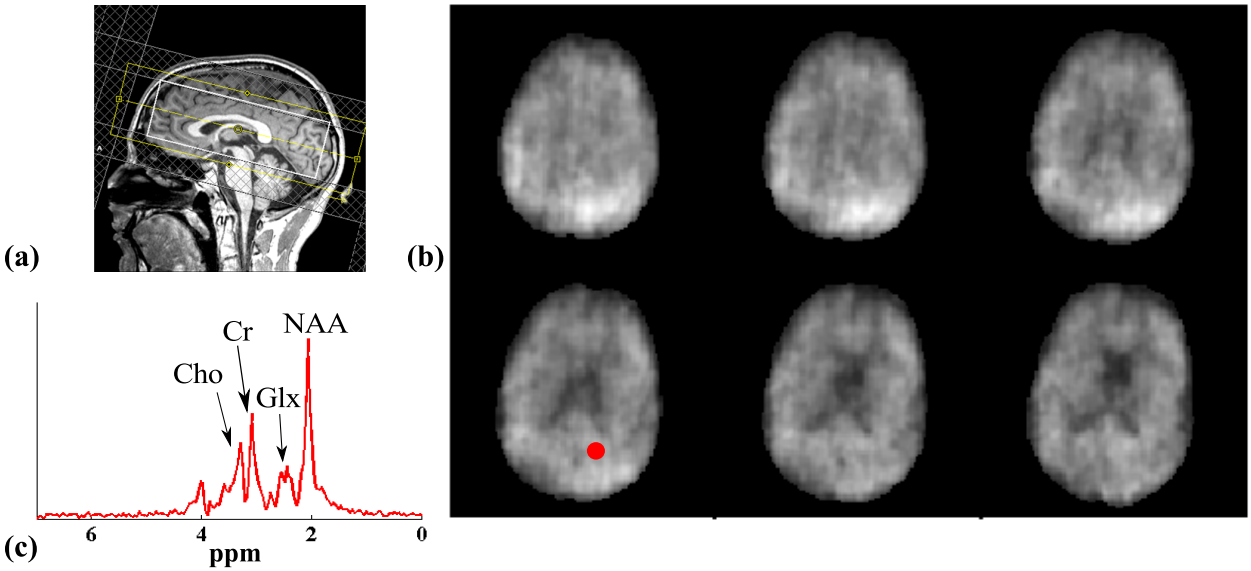

Figure 6.15: Results from a 3D SPICE acquisition with the experimental setup illustrated in (a). Spatial maps of NAA for six different slices are shown in (b). The spectrum corresponding to the voxel at the red dot is shown in (c).

CHAPTER 7

CONCLUSION AND FUTURE WORK

A novel subspace imaging approach, named SPICE, has been proposed to enable accelerated high-resolution MRSI with high SNR. SPICE is characterized by using a low-dimensional subspace model of the high-dimensional spatiospectral function of interest (derived from the partially separable function theory) to devise both special hybrid sparse sampling strategies to cover an extended (k, t)-space (through the acquisition of two data sets $\mathcal{D}_1$ and $\mathcal{D}_2$) and special low-rank model based reconstruction strategies for image reconstruction from sparse data. Special data acquisition and image reconstruction methods have been developed to implement the SPICE framework to achieve high-resolution ^{1}H-MRSI of the brain. For data acquisition, a hybrid CSI/EPSI sequence is proposed for fast 2D high-resolution ^{1}H-MRSI using SPICE and a dual-density, dual-speed EPSI-like sequence is proposed to further accelerate the spatiospectral encoding for high-resolution 3D ^{1}H-MRSI using SPICE. For image reconstruction, an explicit low-rank representation derived from the subspace model is introduced. This representation allows us to define the reconstruction problem as separately determining the subspace structure and the corresponding spatial coefficients (to construct the spatiotemporal/spatiospectral distribution), which can then be formulated as regularized least-squares estimation problems that can be solved by efficient numerical algorithms.

Theoretical analysis and numerical simulations have been performed to evaluate the properties of the SPICE framework and to optimize the data acquisition design. Phantom and in vivo brain ^{1}H-MRSI data were acquired to evaluate and validate the performance of the proposed methods in practical experiments. In particular, for 2D in vivo experiments, SPICE is able to produce high-SNR ^{1}H metabolite maps from the human brain with an approximately 2 mm nominal in-plane resolution in 15 minutes. For 3D in vivo experiments, SPICE is able to produce metabolite maps with an approximately 3 mm in-plane and 4 mm

through-plane resolution in about 26 minutes. To the best of our knowledge, these are the highest resolution ^{1}H metabolite maps ever obtained from human brain on a 3T system. We expect SPICE to provide a powerful tool for in vivo metabolic studies with many exciting applications.

The SPICE framework also offers new opportunities for future technical developments including optimizations in signal generation, signal encoding, data processing and image reconstruction to advance the research and clinical applications of high-resolution in vivo MRSI. For example, incorporating recent developments in advanced pulse design, e.g., LASER/semi-LASER type of techniques, into the subspace-based data acquisition schemes can improve spatial localization and detection of J-coupled metabolites [14, 31, 127]. Using FID excitation (instead of spin-echo excitation) can help achieve shorter echo times and repetition times, providing better SNR and additional flexibility for making the trade-off between SNR and acquisition time [15, 128] for high-resolution acquisitions. Moreover, with progress in advanced nuisance signal removal methods, it is possible to perform ^{1}H-MRSI experiments without water and lipid suppression pulses, which not only allows us to further reduce repetition time but also provides water reference data that are useful for inhomogeneity correction and metabolite quantification.

There is also tremendous opportunity in future research for the optimization of (k, t)-space trajectories, especially for 3D high-resolution MRSI using SPICE. For instance, we can further accelerate the acquisition of $\mathcal{D}_2$ by integrating compressed sensing-based sparse sampling and parallel imaging, making it more adaptive to time constraints in various practical applications. It is also possible to integrate non-Cartesian sampling trajectories (as those in [27, 31, 129]) into the SPICE acquisition framework to offer better spatiospectral encoding efficiency. Furthermore, we can optimize the key acquisition parameters for both $\mathcal{D}_1$ and $\mathcal{D}_2$ (e.g., sampled k-space locations and the intervals between echo shifts), through both theoretical analysis [130] and simulation studies. Building on these optimizations, one can also improve the reconstruction by exploiting stronger spatiospectral prior information. In addition, more effective ways to combine data from both $\mathcal{D}_1$ and $\mathcal{D}_2$ for improved spatial coefficient estimation are worth investigating.

While this thesis focuses on ^{1}H-MRSI, the developed techniques can also be used for high-

resolution spectroscopic imaging of other nuclei, such as phosphorus-31 (^{31}P), carbon-13 (^{13}C) or fluorine-19 (^{19}F). Tailoring the current methods for these modalities would require special hardware (e.g., double-tuned coils) and optimization of data acquisition schemes (e.g., taking into account the very short T_2 of ^{31}-P metabolites). Success in these developments will potentially be useful for a wide range of applications, such as studying brain and cardiac energetics [131, 132], understanding in vivo carbohydrate metabolism [133], and identifying biomarkers for various metabolic diseases [14, 134].

Another exciting direction for future research is extending the current SPICE framework to spatially-resolved multi-dimensional spectroscopy (e.g., J-resolved MRSI) or dynamic high-resolution MRSI. To this end, more sophisticated hybrid sparse sampling strategies need to be developed for acquiring data with complementary properties for subspace estimation and image reconstruction. More advanced mathematical tools, such as low-rank tensor models and related algorithms, are needed to solve the resulting reconstruction problems [78, 135]. Addressing these problems may open up many more opportunities for developing new technologies and applications of in vivo MRSI.

REFERENCES

[1] P. C. Lauterbur, D. M. Kramer, W. V. House, and C.-N. Chen, "Zeugmatographic high resolution nuclear magnetic resonance spectroscopy: Images of chemical inhomogeneity within macroscopic objects," *J. Amer. Chem. Soc.*, vol. 97, pp. 6866 – 6868, 1975. 1, 11, 12

[2] T. R. Brown, B. M. Kincaid, and K. Ugurbil, "NMR chemical shift imaging in three dimensions," *Proc. Natl. Acad. Sci.*, vol. 79, pp. 3523 – 3526, 1982. 1, 12, 13, 15

[3] P. C. Lauterbur, D. N. Levin, and R. B. Marr, "Theory and simulation of NMR spectroscopic imaging and field plotting by projection reconstruction involving an intrinsic frequency dimension," *J. Magn. Reson.*, vol. 59, pp. 536 – 541, 1984. 1

[4] A. A. Maudsley, S. K. Hilal, W. H. Perman, and H. E. Simon, "Spatially resolved high resolution spectroscopy by "four-dimensional" NMR," *J. Magn. Reson.*, vol. 51, pp. 147 – 152, 1983. 1

[5] J. Kurhanewicz, D. B. Vigneron, and S. J. Nelson, "Three-dimensional magnetic resonance spectroscopic imaging of brain and prostate cancer," *Neoplasia*, vol. 2, pp. 166 – 189, 2000. 1, 2

[6] S. J. Nelson, "Assessment of therapeutic response and treatment planning for brain tumors using metabolic and physiological MRI," *NMR Biomed.*, vol. 24, pp. 734 – 749, 2011. 1

[7] B. Hamans, A. C. Navis, A. Wright, P. Wesseling, A. Heerschap, and W. Leenders, "Multivoxel 1H MR spectroscopy is superior to contrast-enhanced MRI for response assessment after anti-angiogenic treatment of orthotopic human glioma xenografts and provides handles for metabolic targeting," *Neuro-Oncology*, vol. 15, pp. 1615 – 1624, 2013. 1

[8] J. W. Hugg, K. D. Laxer, G. B. Matson, A. A. Maudsley, and M. W. Weiner, "Neuron loss localizes human temporal lobe epilepsy by in vivo proton magnetic resonance spectroscopic imaging," *Annals of Neurology*, vol. 34, pp. 788 – 794, 1993. 1

[9] E. P. Pioro, J. P. Antel, N. R. Cashman, and D. L. Arnold, "Detection of cortical neuron loss in motor neuron disease by proton magnetic resonance spectroscopic imaging in vivo," *Neurology*, vol. 44, no. 10, p. 1933, 1994. 1

[10] E. Hattingen, J. Magerkurth, U. Pilatus, A. Mozer, C. Seifried, H. Steinmetz, F. Zanella, and R. Hilker, "Phosphorus and proton magnetic resonance spectroscopy demonstrates mitochondrial dysfunction in early and advanced Parkinson's disease," *Brain*, vol. 132, pp. 3285 – 3297, 2009. 1

[11] S. C. Licata and P. F. Renshaw, "Neurochemistry of drug action: Insights from proton magnetic resonance spectroscopic imaging and their relevance to addiction," *Annals of the New York Academy of Sciences*, vol. 1187, pp. 148 – 171, 2010. 1

[12] S. Posse, R. Otazo, S. R. Dager, and J. Alger, "MR spectroscopic imaging: Principles and recent advances," *J. Magn. Reson. Imag.*, vol. 37, pp. 1301 – 1325, 2013. 1, 2, 5

[13] B. E. Levin, H. L. Katzen, A. Maudsley, J. Post, C. Myerson, V. Govind, F. Nahab, B. Scanlon, and A. Mittel, "Whole-brain proton MR spectroscopic imaging in Parkinson's disease," *J. Neuroimaging*, vol. 24, pp. 39 – 44, 2014. 1

[14] R. A. de Graaf, *In Vivo NMR Spectroscopy: Principles and Techniques*. Hoboken, NJ: John Wiley & Sons, 2007. 1, 12, 13, 14, 48, 71, 91, 92

[15] R. Pohmann, M. von Kienlin, and A. Haase, "Theoretical evaluation and comparison of fast chemical shift imaging methods," *J. Magn. Reson.*, vol. 129, pp. 145 – 160, 1997. 1, 2, 15, 28, 46, 91

[16] R. Mekle, V. Mlynarik, G. Gambarota, M. Hergt, G. Krueger, and R. Gruetter, "MR spectroscopy of the human brain with enhanced signal intensity at ultrashort echo times on a clinical platform at 3T and 7T," *Magn. Reson. Med.*, vol. 61, pp. 1279 – 1285, 2009. 2

[17] U. Dydak, M. Weiger, K. P. Pruessmann, D. Meier, and P. Boesiger, "Sensitivity-encoded spectroscopic imaging," *Magn Reson Med*, vol. 46, pp. 713 – 722, 2001. 2

[18] U. Dydak, K. P. Pruessmann, M. Weiger, J. Tsao, D. Meier, and P. Boesiger, "Parallel spectroscopic imaging with spin-echo trains," *Magn. Reson. Med.*, vol. 50, pp. 196 – 200, 2003. 2

[19] F.-H. Lin, S.-Y. Tsai, R. Otazo, A. Caprihan, L. L. Wald, J. W. Belliveau, and S. Posse, "Sensitivity-encoded (SENSE) proton echo-planar spectroscopic imaging (PEPSI) in the human brain," *Magn. Reson. Med.*, vol. 57, pp. 249 – 257, 2007. 2

[20] S.-Y. Tsai, R. Otazo, S. Posse, Y.-R. Lin, H.-W. Chung, L. L. Wald, G. C. Wiggins, and F.-H. Lin, "Accelerated proton echo planar spectroscopic imaging (PEPSI) using GRAPPA with a 32-channel phased-array coil," *Magn. Reson. Med.*, vol. 59, pp. 989 – 998, 2008. 2

[21] X. Zhu, A. Ebel, J. X. Ji, and N. Schuff, "Spectral phase-corrected GRAPPA reconstruction of three-dimensional echo-planar spectroscopic imaging (3D-EPSI)," *Magn. Reson. Med.*, vol. 57, pp. 815 – 820, 2007. 2

[22] S. Posse, R. Otazo, S.-Y. Tsai, A. E. Yoshimoto, and F.-H. Lin, "Single-shot magnetic resonance spectroscopic imaging with partial parallel imaging," *Magn. Reson. Med.*, vol. 61, pp. 541 – 547, 2009. 2

[23] P. Mansfield, "Spatial mapping of the chemical shift in NMR," *Magn. Reson. Med.*, vol. 1, pp. 370 – 386, 1984. 2, 12, 15

[24] S. Posse, G. Tedeschi, R. Risinger, R. Ogg, and D. L. Bihan, "High speed 1H spectroscopic imaging in human brain by echo planar spatial-spectral encoding," *Magn. Reson. Med.*, vol. 33, pp. 34 – 40, 1995. 2, 15, 26, 28, 40, 46, 49

[25] R. V. Mulkern and L. P. Panych, "Echo planar spectroscopic imaging," *Concepts Magn. Reson.*, vol. 13, pp. 213 – 237, 2001. 2

[26] S. Posse, R. Otazo, A. Caprihan, J. Bustillo, H. Chen, P.-G. Henry, M. Marjanska, C. Gasparovic, C. Zuo, V. Magnotta, B. Mueller, P. Mullins, P. Renshaw, K. Ugurbil, K. O. Lim, and J. R. Alger, "Proton echo-planar spectroscopic imaging of J-coupled resonances in human brain at 3 and 4 Tesla," *Magn. Reson. Med.*, vol. 58, pp. 236 – 244, 2007. 2, 15

[27] E. Adalsteinsson, P. Irarrazabal, S. Topp, C. Meyer, A. Macovski, and D. M. Spielman, "Volumetric spectroscopic imaging with spiral-based k-space trajectories," *Magn. Reson. Med.*, vol. 39, pp. 889 – 898, 1998. 2, 15, 28, 91

[28] A. R. Guimaraes, J. R. Baker, B. G. Jenkins, P. L. Lee, R. M. Weisskoff, B. R. Rosen, and R. G. Gonzalez, "Echoplanar chemical shift imaging," *Magn. Reson. Med.*, vol. 41, pp. 877 – 882, 1999. 2, 28

[29] A. Ebel, A. A. Maudsley, M. W. Weiner, and N. Schuff, "Achieving sufficient spectral bandwidth for volumetric 1H echo-planar spectroscopic imaging at 4 Tesla," *Magn. Reson. Med.*, vol. 54, pp. 697 – 701, 2005. 2, 15

[30] C. V. Schirda, C. Tanase, and F. E. Boada, "Rosette spectroscopic imaging: Optimal parameters for alias-free, high sensitivity spectroscopic imaging," *J. Magn. Reson. Imag.*, vol. 29, pp. 1375 – 1385, 2009. 2

[31] O. C. Andronesi, B. A. Gagoski, and A. G. Sorensen, "Neurologic 3D MR spectroscopic imaging with low-power adiabatic pulses and fast spiral acquisition," *Radiology*, vol. 262, pp. 647 – 661, 2012. 2, 91

[32] C. Labadie, S. Hetzer, J. Schulz, T. Mildner, M. Aubert-Frecon, and H. E. Moller, "Center-out echo-planar spectroscopic imaging with correction of gradient-echo phase and time shifts," *Magn. Reson. Med.*, vol. 70, pp. 16 – 24, 2013. 2, 15, 52

[33] M. S. Ramirez, J. Lee, C. M. Walker, V. C. Sandulache, F. Hennel, S. Y. Lai, and J. A. Bankson, "Radial spectroscopic MRI of hyperpolarized [1-13C] pyruvate at 7 tesla," *Magn. Reson. Med.*, vol. 72, pp. 986 – 995, 2013. 2, 15

[34] X. Hu, D. N. Levin, P. C. Lauterbur, and T. Spraggins, "SLIM: Spectral localization by imaging," *Magn. Reson. Med.*, vol. 8, pp. 314 – 322, 1988. 2, 17

[35] Z.-P. Liang and P. C. Lauterbur, "A generalized series approach to MR spectroscopic imaging," *IEEE Trans. Med. Imag.*, vol. 10, pp. 132 – 137, 1991. 2, 17

[36] M. Jacob, X. Zhu, A. Ebel, N. Schuff, and Z.-P. Liang, "Improved model-based magnetic resonance spectroscopic imaging," *IEEE Trans. Med. Imag.*, vol. 26, pp. 1305 – 1318, 2007. 2, 17

[37] J. P. Haldar, D. Hernando, S. K. Song, and Z.-P. Liang, "Anatomically constrained reconstruction from noisy data," *Magn. Reson. Med.*, vol. 59, pp. 810 – 818, 2008. 2, 17, 30, 51, 58

[38] J. Kornak, K. Young, B. J. Soher, and A. A. Maudsley, "Bayesian k-space-time reconstruction of MR spectroscopic imaging for enhanced resolution," *IEEE Trans. Med. Imag.*, vol. 29, pp. 1333 – 1350, 2010. 2, 17, 30

[39] Y. Zhang, R. E. Gabr, M. Schar, R. G. Weiss, and P. A. Bottomley, "Magnetic resonance spectroscopy with linear algebraic modeling (SLAM) for higher speed and sensitivity," *J. Magn. Reson.*, vol. 218, pp. 66 – 76, 2012. 2, 17

[40] S. Hu, M. Lustig, A. P. Chen, J. Crane, A. Kerr, D. A. C. Kelley, R. Hurd, J. Kurhanewicz, S. J. Nelson, J. M. Pauly, and D. B. Vigneron, "Compressed sensing for resolution enhancement of hyperpolarized 13C flyback 3D-MRSI," *J. Magn. Reson.*, vol. 192, pp. 258 – 264, 2008. 2, 17, 18

[41] R. Eslami and M. Jacob, "Robust reconstruction of MRSI data using a sparse spectral model and high resolution MRI priors," *IEEE Trans. Med. Imag.*, vol. 29, pp. 1297 – 1309, 2010. 2, 17, 30, 58

[42] P. E. Z. Larson, S. Hu, M. Lustig, A. B. Kerr, S. J. Nelson, J. Kurhanewicz, J. M. Pauly, and D. B. Vigneron, "Fast dynamic 3D MR spectroscopic imaging with compressed sensing and multiband excitation pulses for hyperpolarized 13C studies," *Magn. Reson. Med.*, vol. 65, pp. 610 – 619, 2011. 2, 17, 18

[43] J. Kasten, F. Lazeyras, and D. Van De Ville, "Data-driven MRSI spectral localization via low-rank component analysis," *IEEE Trans. Med. Imag.*, vol. 32, pp. 1853 – 1863, 2013. 2, 17, 20, 30, 58

[44] P. Cao and E. X. Wu, "Accelerating phase-encoded proton MR spectroscopic imaging by compressed sensing," *J. Magn. Reson. Imag.*, p. 10.1002/jmri.24553, 2014. 2, 17

[45] I. Chatnuntawech, B. Gagoski, B. Bilgic, S. F. Cauley, K. Setsompop, and E. Adalsteinsson, "Accelerated 1H MRSI using randomly undersampled spiral-based k-space trajectories," *Magn. Reson. Med.*, 2014, doi: 10.1002/mrm.25394. 2, 17, 58

[46] I. Chatnuntawech, B. Bilgic, and E. Adalsteinsson, "Undersampled spectroscopic imaging with model-based reconstruction," in *Proc. Intl. Symp. Magn. Reson. Med.*, Salt Lake City, UT, USA, 2013, p. 3960. 2, 17

[47] Z.-P. Liang, "Spatiotemporal imaging with partially separable functions," in *Proc. IEEE Int. Symp. Biomed. Imag.*, Arlington, VA, USA, 2007, pp. 988 – 991. 3, 18, 19, 20, 24, 56, 57

[48] J. P. Haldar and Z.-P. Liang, "Spatiotemporal imaging with partially separable functions: A matrix recovery approach," in *Proc. IEEE Int. Symp. Biomed. Imag.*, Rotterdam, Netherlands, 2010, pp. 716 – 719. 3, 19, 57

[49] H. M. Nguyen, X. Peng, M. N. Do, and Z.-P. Liang, "Denoising MR spectroscopic imaging data with low-rank approximations," *IEEE Trans. Biomed. Eng.*, vol. 60, pp. 78 – 89, 2013. 3, 20, 24, 31, 38, 51

[50] F. Lam and Z.-P. Liang, "A subspace approach to high–resolution spectroscopic imaging," *Magn. Reson. Med.*, vol. 71, pp. 1349 – 1357, 2014. 3, 19, 24, 31, 51, 56

[51] A. A. Maudsley, C. Domenig, V. Govind, A. Darkazanli, C. Studholme, K. Arheart, and C. Bloomer, "Mapping of brain metabolite distributions by volumetric proton MR spectroscopic imaging (MRSI)," *Magn. Reson. Med.*, vol. 61, pp. 548 – 559, 2009. 5, 15, 46, 49

[52] Z.-P. Liang and P. C. Lauterbur, *Principles of Magnetic Resonance Imaging: A Signal Processing Perspective*. New York: IEEE Press, 2000. 6, 7, 8, 9, 12, 13, 36

[53] E. M. Haacke, R. W. Brown, M. R. Thompson, and R. Venkatesan, *Magnetic Resonance Imaging: Physical Principles and Sequence Design*. New York, Chicester, Weinheim: J. Wiley & Sons, 1999. 8

[54] K. Wuthrich, *NMR of Proteins and Nucleic Acids*. Hoboken, NJ: John Wiley & Sons, 1986. 12

[55] B. P. Sutton, D. C. Noll, and J. A. Fessler, "Fast, iterative image reconstruction for MRI in the presence of field inhomogeneities," *IEEE Trans. Med. Imag.*, vol. 22, pp. 178 – 188, 2003. 16

[56] J. A. Fessler, S. Lee, V. T. Olafsson, H. R. Shi, and D. C. Noll, "Toeplitz-based iterative image reconstruction for MRI with correction for magnetic field inhomogeneity," *IEEE Trans. Sig. Proc.*, vol. 53, pp. 3393 – 3402, 2005. 16

[57] S. S. Stone, J. P. Haldar, S. C. Tsao, W. m. W. Hwu, B. P. Sutton, and Z.-P. Liang, "Accelerating advanced MRI reconstructions on GPUs," *J. Parallel Distr. Com.*, vol. 68, pp. 1307 – 1318, 2008. 16

[58] A. Ebel and A. A. Maudsley, "Detection and correction of frequency instabilities for volumetric 1H echo-planar spectroscopic imaging," *Magn. Reson. Med.*, vol. 53, pp. 465 – 469, 2005. 17, 47

[59] A. Tal and O. Gonen, "Localization errors in MR spectroscopic imaging due to the drift of the main magnetic field and their correction," *Magn. Reson. Med.*, vol. 70, pp. 895 – 904, 2013. 17

[60] I. Khalidov, D. Van De Ville, M. Jacob, F. Lazeyras, and M. Unser, "BSLIM: Spectral localization by imaging with explicit B_0 field inhomogeneity compensation," *IEEE Trans. Med. Imag.*, vol. 26, pp. 990 – 1000, 2007. 17

[61] Z. P. Liang and P. C. Lauterbur, "A theoretical analysis of the SLIM technique," *J. Magn. Reson.*, vol. 102, pp. 54 – 60, 1993. 17

[62] D. L. Donoho, "Compressed sensing," *IEEE Trans. Inf. Theory*, vol. 52, pp. 1289 – 1306, 2006. 17

[63] E. Candès, J. Romberg, and T. Tao, "Robust uncertainty principles: Exact signal reconstruction from highly incomplete frequency information," *IEEE Trans. Inf. Theory*, vol. 52, pp. 489 – 509, 2006. 17

[64] M. Elad, *Sparse and Redundant Representations: From Theory to Applications in Signal and Image Processing.* New York: Springer-Verlag, 2010. 17

[65] D. L. Donoho, A. Maleki, and A. Montanari, "Message-passing algorithms for compressed sensing," *Proc. Natl. Acad. Sci.*, vol. 106, pp. 18 914 – 18 919, 2009. 17

[66] M. Lustig, D. L. Donoho, and J. M. Pauly, "Sparse MRI: The application of compressed sensing for rapid MR imaging," *Magn. Reson. Med.*, no. 58, pp. 1182 – 1195, 2007. 17

[67] H. Jung, K. Sung, K. S. Nayak, E. Y. Kim, and J. C. Ye, "k-t FOCUSS: A general compressed sensing framework for high resolution dynamic MRI," *Magn. Reson. Med.*, vol. 61, pp. 103 – 116, 2009. 17

[68] D. Liang, B. Liu, J. Wang, and L. Ying, "Accelerating SENSE using compressed sensing," *Magn. Reson. Med.*, vol. 62, pp. 1574 – 1584, 2009. 17

[69] J. P. Haldar, D. Hernando, and Z.-P. Liang, "Compressed-sensing MRI with random encoding," *IEEE Trans. Med. Imag.*, vol. 30, pp. 893 – 903, 2011. 17

[70] W. A. Light and E. W. Cheney, *Approximation Theory in Tensor Product Spaces.* Berlin Heidelberg: Springer-Verlag, 1985. 18

[71] M. Reed and B. Simon, *Methods of Modern Mathematical Physics I: Functional Analysis.* Waltham, MA: Academic Press, 1980. 19

[72] B. Zhao, J. P. Haldar, A. G. Christodoulou, and Z.-P. Liang, "Image reconstruction from highly undersampled (k, t)-space data with joint partial separability and sparsity constraints," *IEEE Trans. Med. Imag.*, vol. 31, pp. 1809 – 1820, 2012. 19, 20, 58

[73] A. G. Christodoulou, T. K. Hitchens, Y. L. Wu, C. Ho, and Z.-P. Liang, "Improved subspace estimation for low-rank model-based accelerated cardiac imaging," *IEEE Trans. Biomed. Eng.*, vol. 61, pp. 2451 – 2457, 2014. 19, 40

[74] M. Fu, B. Zhao, C. Carignan, R. K. Shosted, J. L. Perry, D. P. Kuehn, Z.-P. Liang, and B. P. Sutton, "High-resolution dynamic speech imaging with joint low-rank and sparsity constraints," *Magn. Reson. Med.*, 2014, doi: 10.1002/mrm.25302. 19, 20, 58

[75] A. Cichocki, R. Zdunek, and S.-I. Amari, "Nonnegative matrix and tensor factorization [lecture notes]," *IEEE Signal Process. Mag.*, vol. 25, pp. 142 – 145, 2008. 19

[76] E. J. Candès, X. Li, Y. Ma, and J. Wright, "Robust principal component analysis?" *J. ACM*, vol. 58, pp. 11:1 – 11:37, 2011. 19

[77] J. Wright, A. Ganesh, K. Min, and Y. Ma, "Compressive principal component pursuit," in *Proceedings of 2012 IEEE International Symposium on Information Theory*, Cambridge, MA, 2012, pp. 1276 – 1280. 19

[78] T. G. Kolda and B. W. Bader, "Tensor decompositions and applications," *SIAM REVIEW*, vol. 51, pp. 455 – 500, 2009. 19, 92

[79] B. Jiang, S. Ma, and S. Zhang, "Tensor principal component analysis via convex optimization," *Mathematical Programming*, pp. 1 – 35, 2014. 19

[80] C. Brinegar, S. S. Schmitter, N. N. Mistry, G. A. Johnson, and Z.-P. Liang, "Improving temporal resolution of pulmonary perfusion imaging in rats using the partially separable functions model," *Magn. Reson. Med.*, vol. 64, pp. 1162 – 1170, 2010. 20

[81] A. G. Christodoulou, H. Zhang, B. Zhao, T. K. Hitchens, C. Ho, and Z.-P. Liang, "High-resolution cardiovascular MRI by integrating parallel imaging with low-rank and sparse modeling," *IEEE Trans. Biomed. Eng.*, vol. 60, pp. 3083 – 3092, 2013. 20, 58

[82] S. Lingala, Y. Hu, E. DiBella, and M. Jacob, "Accelerated dynamic MRI exploiting sparsity and low-rank structure: k-t SLR," *IEEE Trans. Med. Imag.*, vol. 30, pp. 1042 – 1054, 2011. 20

[83] B. Zhao, A. Sun, K. Ma, R. Li, A. G. Christodoulou, C. Yuan, and Z.-P. Liang, "Real-time phase contrast flow imaging with joint low-rank and sparsity constraints," in *Proc. Intl. Symp. Magn. Reson. Med.*, Milan, Italy, 2014, p. 743. 20

[84] B. Zhao, W. Lu, T. K. Hitchens, F. Lam, C. Ho, and Z.-P. Liang, "Accelerated MR parameter mapping with low-rank and sparsity constraints," *Magn. Reson. Med.*, 2014, doi: 10.1002/mrm.25421. 20, 62

[85] F. Lam, B. Zhao, Y. Liu, Z.-P. Liang, M. Weiner, and N. Schuff, "Accelerated fMRI using low-rank model and sparsity constraints," in *Proc. Intl. Symp. Magn. Reson. Med.*, Salt Lake City, 2013, p. 2620. 20

[86] M. Chiew, S. M. Smith, P. J. Koopmans, N. N. Graedel, T. Blumensath, and K. L. Miller, "k-t FASTER: Acceleration of functional MRI data acquisition using low rank constraints," *Magn. Reson. Med.*, 2014, doi: 10.1002/mrm.25395. 20

[87] C. L. Johnson, J. L. Holtrop, A. G. Christodoulou, M. D. J. McGarry, J. B. Weaver, K. D. Paulsen, Z.-P. Liang, J. G. Georgiadis, and B. P. Sutton, "Accelerating MR elastography with sparse sampling and low-rank reconstruction," in *Proc. Intl. Symp. Magn. Reson. Med.*, Milan, Italy, 2014, p. 325. 20

[88] F. Lam, S. D. Babacan, J. P. Haldar, M. W. Weiner, N. Schuff, and Z.-P. Liang, "Denoising diffusion-weighted magnitude MR images using rank and edge constraints," *Magn. Reson. Med.*, vol. 71, pp. 1272 – 1284, 2014. 20

[89] H. Gao, L. Li, K. Zhang, W. Zhou, and X. Hu, "PCLR: Phase-constrained low-rank model for compressive diffusion-weighted MRI," *Magn. Reson. Med.*, vol. 72, pp. 1522 – 2594, 2013. 20

[90] H. Cramér, *Mathematical Methods of Statistics*. Princeton, NJ: Princeton Univ. Press., 1946. 21

[91] B. C. Levy, *Principles of Signal Detection and Parameter Estimation*. New York: Springer, 2008. 21, 22

[92] J. D. Gorman and A. O. Hero, "Lower bounds for parametric estimation with constraints," *IEEE Trans. Inf. Theory*, vol. 36, pp. 1285 – 1301, 1990. 22

[93] Z. Ben-Haim and Y. C. Eldar, "The Cramer-Rao bound for estimating a sparse parameter vector," *IEEE Trans. Sig. Proc.*, vol. 58, pp. 3384 – 3389, 2010. 22

[94] S. Kay and Y. C. Eldar, "Rethinking biased estimation [Lecture Notes]," *IEEE Sig. Proc. Mag.*, vol. 25, pp. 133 – 136, 2008. 22

[95] J. A. Fessler, "Mean and variance of implicitly defined biased estimators (such as penalized maximum likelihood): Applications to tomography," *IEEE Trans. Imag. Process.*, vol. 5, pp. 493 – 506, 1996. 22

[96] F. Lam, C. Ma, and Z.-P. Liang, "Performance analysis of denoising with low-rank and sparsity constraints," in *Biomedical Imaging: From Nano to Macro, 2013 IEEE International Symposium on*, San Francisco, CA, April 2013, pp. 1223 – 1226. 22

[97] T. J. Kragh and A. O. Hero, "Image resolution-variance tradeoffs using the uniform Cramer-Rao bound," in *In Proc. Euro. Sig. Proc. Conf. (EUSIPCO*, 1987, pp. 20 330 – 5000. 22

[98] D. Hernando, Z.-P. Liang, and P. Kellman, "Chemical shift$v$based water/fat separation: A comparison of signal models," *Magn. Reson. Med.*, vol. 64, pp. 811 – 822, 2010. 22

[99] J. P. Haldar, D. Hernando, and Z.-P. Liang, "Super-resolution reconstruction of MR image sequences with contrast modeling," in *Biomedical Imaging: From Nano to Macro, 2009 IEEE International Symposium on*, Boston, MA, June 2009, pp. 266 – 269. 22

[100] B. Zhao, F. Lam, and Z.-P. Liang, "Model-based MR parameter mapping with sparsity constraints: Parameter estimation and performance bounds," *IEEE Trans. Med. Imag.*, vol. 33, pp. 1832 – 1844, 2014. 22

[101] D. H. J. Poot, A. J. den Dekker, E. Achten, M. Verhoye, and J. Sijbers, "Optimal experimental design for diffusion kurtosis imaging," *IEEE Trans. Med. Imag.*, vol. 29, pp. 819 – 829, 2010. 22

[102] A. R. Pineda, S. B. Reeder, Z. Wen, and N. J. Pelc, "Cramer-Rao bounds for three-point decomposition of water and fat," *Magn. Reson. Med.*, vol. 54, pp. 625 – 635, 2005. 22

[103] C. S. Bolliger, C. Boesch, and R. Kreis, "On the use of Cramer-Rao minimum variance bounds for the design of magnetic resonance spectroscopy experiments," *NeuroImage*, vol. 83, pp. 1031 – 1040, 2013. 22

[104] H. M. Nguyen, Z. J. Gahvari, J. P. Haldar, M. N. Do, and Z.-P. Liang, "Cramer-Rao bound analysis of echo time selection for ^{1}H-MR spectroscopy," in *Annual International Conference of the IEEE Engineering in Medicine and Biology Society*, Minneapolis, MN, Sept 2009, pp. 2692 – 2695. 22

[105] C. Ma, F. Lam, C. L. Johnson, and Z.-P. Liang, "Removal of nuisance signals from limited and sparse ^{1}H MRSI data using a union-of-subspaces model," *Magn. Reson. Med.*, 2015, doi: 10.1002/mrm.25635. 24, 26, 51, 56, 64

[106] D. Spielman, P. Webb, and A. Macovski, "Water referencing for spectroscopic imaging," *Magn. Reson. Med.*, vol. 12, pp. 38 – 49, 1989. 29

[107] D. C. Noll, J. A. Fessler, and B. P. Sutton, "Conjugate phase MRI reconstruction with spatially variant sample density correction," *IEEE Trans. Med. Imag.*, vol. 24, pp. 325 – 336, 2005. 29, 40, 73

[108] X. Peng, H. Nguyen, J. P. Haldar, D. Hernando, X.-P. Wang, and Z.-P. Liang, "Correction of field inhomogeneity effects on limited k-space MRSI data using anatomical constraints," in *Proc. IEEE Eng. Med. Biol. Soc.*, 2010, pp. 883 – 886. 29, 40, 51, 56, 57

[109] A. C. Gilbert, J. Y. Park, and M. B. Wakin, "Sketched SVD: Recovering spectral features from compressive measurements," 2012, arxiv preprint arXiv:1211.0361. 32

[110] B. J. Soher, K. Young, A. Bernstein, Z. Aygula, and A. A. Maudsley, "GAVA: Spectral simulation for in vivo MRS applications," *J. Magn. Reson.*, vol. 185, pp. 291 – 299, 2007. 38

[111] R. J. Ogg, R. B. Kingsley, and J. S. Taylor, "WET, a T1- and B1-insensitive water-suppression method for in vivo localized 1H NMR spectroscopy," *J. Magn. Reson.*, vol. 104, pp. 1 – 10, 1994. 48, 73

[112] B. Recht, M. Fazel, and P. A. Parrilo, "Guaranteed minimum-rank solutions of linear matrix equations via nuclear norm minimization," *SIAM Rev.*, vol. 52, pp. 471 – 501, 2010. 57

[113] J. P. Haldar and D. Hernando, "Rank-constrained solutions to linear matrix equations using powerfactorization," *IEEE Signal. Process. Lett.*, vol. 16, pp. 584 – 587, 2009. 57

[114] B. Zhao, J. P. Haldar, A. G. Christodoulou, and Z.-P. Liang, "Further development of image reconstruction from highly undersampled (k, t)-space data with joint partial separability and sparsity constraints," in *Proc. IEEE Int. Symp. Biomed. Imag.*, Chicago, IL, USA, 2011, pp. 1593 – 1596. 58

[115] J.-F. Cai, E. J. Candès, and Z. Shen, "A singular value thresholding algorithm for matrix completion," *SIAM J. Optimization*, vol. 20, pp. 1956 – 1982, 2010. 61

[116] M. Nikolava and M. K. NG, "Analysis of half-quadratic minimization methods for signal and image recovery," *SIAM J. Sci. Comput.*, vol. 27, pp. 937 – 966, 2005. 60

[117] J. Yang, Y. Zhang, and W. Yin, "A fast alternating direction method for TVL1-L2 signal reconstruction from partial Fourier data," *Selected Topics in Signal Processing, IEEE Journal of*, vol. 4, pp. 288 – 297, 2010. 60, 64

[118] J. Yang and Y. Zhang, "Alternating direction algorithms for ℓ_1-problems in compressive sensing," *SIAM J. Sci. Comput.*, vol. 33, pp. 250 – 278, 2011. 60

[119] S. Ramani and J. A. Fessler, "Parallel MR image reconstruction using augmented Lagrangian methods," *IEEE Trans. Med. Imag.*, vol. 30, pp. 694 – 706, 2011. 60, 62

[120] Z. Lin, R. Liu, and Z. Su, "Linearized alternating direction method with adaptive penalty for low-rank representation," in *NIPS*, 2011, pp. 612 – 620. 60

[121] S. G. Lingala, Y. Hu, E. Dibella, and M. Jacob, "Accelerated first pass cardiac perfusion MRI using improved k-t SLR," in *Biomedical Imaging: From Nano to Macro, 2011 IEEE International Symposium on*, March 2011, pp. 1280 – 1283. 62

[122] F. Lam, B. Zhao, M. Weiner, N. Schuff, and Z.-P. Liang., "Denoising image sequences: Algorithm and application to quantitative MR imaging," in *International Society for Magnetic Resonance in Medicine, Salt Lake City*, 2013, p. 3814. 62

[123] D. L. Donoho, "De-noising by soft-thresholding," *IEEE Trans. Inf. Theory*, vol. 41, pp. 613 – 627, 1995. 63

[124] M. Bydder, G. Hamilton, T. Yokoo, and C. B. Sirlin, "Optimal phased-array combination for spectroscopy," *Magn. Reson. Imag.*, vol. 26, pp. 847 – 850, 2008. 66

[125] H. Barkhuysen, R. de Beer, and D. van Ormondt, "Improved algorithm for noniterative time-domain model fitting to exponentially damped magnetic resonance signals," *J. Magn. Reson.*, vol. 73, pp. 553 – 557, 1987. 73

[126] C. R. Vogel, *Computational Methods for Inverse Problems*. Philadelphia, PA: SIAM, 2002. 74, 75

[127] J. W. Pan, T. Venkatraman, K. Vives, and D. D. Spencer, "Quantitative glutamate spectroscopic imaging of the human hippocampus," *NMR. Biomed.*, vol. 19, pp. 209 – 216, 2006. 91

[128] W. Bogner, S. Gruber, S. Trattnig, and M. Chmelik, "High-resolution mapping of human brain metabolites by free induction decay 1H mrsi at 7T," *NMR Biomed.*, vol. 25, pp. 873 – 882, 2012. 91

[129] B. P. Sutton, C. A. Conway, Y. Bae, R. Seethamraju, and D. P. Kuehn, "Faster dynamic imaging of speech with field inhomogeneity corrected spiral fast low angle shot (FLASH) at 3 T," *J. Magn. Reson. Imag.*, vol. 32, pp. 1228 – 1237, 2010. 91

[130] F. Pukelsheim, *Optimal Design of Experiments*. Philadelphia, PA: SIAM, 2006. 91

[131] R. G. Shulman, T. R. Brown, K. Ugurbil, S. Ogawa, S. M. Cohen, and J. A. den Hollander, "Cellular applications of 31P and 13C nuclear magnetic resonance," *Science*, vol. 205, pp. 160 – 166, 1979. 92

[132] X.-H. Zhu, H. Qiao, F. Du, Q. Xiong, X. Liu, X. Zhang, K. Ugurbil, and W. Chen, "Quantitative imaging of energy expenditure in human brain," *NeuroImage*, vol. 60, pp. 2107 – 2117, 2012. 92

[133] R. Gruetter, G. Adriany, I.-Y. Choi, P.-G. Henry, H. Lei, and G. Oz, "Localized in vivo ^{13}C NMR spectroscopy of the brain," *NMR Biomed.*, vol. 16, pp. 313 – 338, 2003. 92

[134] J.-H. Hwang and C. S. Choi, "Use of in vivo magnetic resonance spectroscopy for studying metabolic diseases," *Exp. Mol. Med.*, vol. 47, 2015, doi:10.1038/emm.2014.101. 92

[135] N. D. Sidiropoulos and A. Kyrillidis, "Multi-way compressed sensing for sparse low-rank tensors," *IEEE Signal. Process. Lett.*, vol. 19, pp. 757 – 760, 2012. 92